

Charles University

Faculty of Science

Study program: Organic Chemistry



Ing. Rafael Navrátil

Photodissociation studies of xanthene dyes, iron(III) azido complexes and hemithioindigo
molecular switches in the gas phase

Fotodisociační studie xanthenových barviv, železitých azido komplexů a hemithioindigových
molekulových přepínačů v plynné fázi

Doctoral thesis

Supervisor: Prof. Mgr. Jana Roithová, Ph. D.

Prague, 2019

Declaration

The work presented in this dissertation thesis was carried out under the supervision of Professor Jana Roithová, Ph. D. at the Department of Organic Chemistry at the Charles University, Prague, Czech Republic. I declare that this thesis has been composed solely by myself and that it has not been submitted, in whole or in part, in any previous application for a degree.

In Prague

Rafael Navrátil

Acknowledgements

First and foremost, I thank my supervisor Prof. Jana Roithová for the opportunity to participate on the research in her group.

I thank Prof. Dieter Gerlich is for his patience during numerous, often overwhelming and virtually endless discussions on ion spectroscopy, mass spectrometry, astrophysics, lasers, *etc.* Moreover, I won't forget about amusing moments in Dieter's car (not) going up a slope in snow-covered Krkonoše mountains. Physics is indeed impossible to cheat.

I am indebted to Juraj Jašík for his invaluable assistance and guidance during ion spectroscopy experiments. Many experimental results would not have been achievable without him, often simply because of his supernatural skills in fixing broken things.

I extent my gratitude also to the people who closely collaborated with me, namely Martin Srnec, Ondřej Baszczyński, Erik Andris, Marek Martínek and Peter Šebej. It was a real pleasure to pursue interesting research ideas together with them.

Many thanks belong to both present and past members of Roithová research group, namely Mariarosa, Anamarija, Ghazaleh, Lucka, Erik, Honza, Guilherme, Tono, Vlada, Thibault, Kyrill, Jesus,... These folks created a great working environment and always supported me, not only as colleagues but also as true friends. Furthermore, I would like to thank “Professor” Abbas Al Temimi for his support and friendship, which encouraged me during my stay at the Radboud University in Netherlands. I cherish the moments I spent with Abbas, especially Sunday fruit lunches and evening table tennis matches.

I am very grateful to Carlos V. Melo for proof-reading this Thesis and also many of my papers. Thanks to him, my scientific writing and presentation skills has significantly improved. To quote his own words: “Scientific writing. It works. Period.”

Most importantly, I would like to express my deepest gratitude to my family, girlfriend and friends for their love. Without their support, this work would not have been possible.

Finally, I would like to thank the reviews of this Thesis for their time and I look forward to any feedback and comments.

Abstract

Electronic excitation triggered by the absorption of light enables numerous chemical, physical and biological processes and transformations. Accordingly, full control over the processes involving excited molecules requires an in-depth knowledge of electronic UV/vis spectra and potential energy surfaces. Unsurprisingly, most electronic spectra are acquired in the condensed phase in which molecules are dissolved and most transformations occur. However, our knowledge of excitation, transformations and processes at the level of isolated molecules is still limited, partly because such studies require unconventional experimental approaches and equipment. This Thesis describes experimental methods for recording electronic spectra of isolated molecules in the gas phase by ion spectroscopy, which combines mass spectrometry with optical spectroscopy. Using these methods, experimental factors which affect the electronic excitation and therefore the electronic spectra of ions were determined and evaluated for various fluorescent xanthene dyes, iron-containing complexes and molecular photoswitches. Furthermore, factors which govern photochemical processes, such as photo-oxidation, photoreduction and photoisomerization, were also analyzed in detail, with surprisingly different outcomes from previous studies of those processes in the condensed phase. All results were complemented with theoretical calculations, which explain the experimental observations. Ultimately, this Thesis provides an overview of possible research avenues and applications of ion spectroscopy for studying photochemical processes.

Abstrakt

Elektronová excitace vyvolaná absorpcí světla umožňuje řadu chemických, fyzikálních a biologických procesů a přeměn. Plná kontrola nad procesy zahrnující excitované molekuly vyžaduje důkladnou znalost elektronových UV/vis spekter a hyperploch potenciální energie. Není překvapivé, že většina elektronových spekter je naměřena v kondenzované fázi, ve které jsou molekuly rozpuštěny a ve které většina přeměn a procesů probíhá. Naopak znalosti o excitaci, přeměnách a procesech na úrovni izolovaných molekul jsou stále omezené, částečně protože odpovídající studie vyžadují nekonvenční experimentální přístupy a vybavení. Tato disertační práce popisuje experimentální metody pro měření elektronových spekter izolovaných molekul v plynné fázi s pomocí iontové spektroskopie, která kombinuje metody hmotností spektrometrie a optické spektroskopie. Za použití těchto metod byly stanoveny a vyhodnoceny experimentální faktory, které ovlivňují elektronovou excitaci a tím pádem elektronová spektra nejrůznějších fluorescenčních xanthenových barviv, komplexů železa a molekulových přepínačů. Také byly studovány faktory, které ovlivňují fotochemické procesy, jakými jsou fotooxidace, fotoredukce a fotoizomerizace, s překvapivě odlišnými výsledky oproti studiím těchto procesů v kondenzované fázi. Všechny výsledky byly doplněny teoretickými výpočty, které vysvětlují experimentální pozorování. Celkově tato disertační práce poskytuje přehled potenciálních výzkumných směrů a aplikací iontové spektroskopie pro studium fotochemických procesů.

List of Abbreviations

4P ₁	first quadrupole of the ISORI instrument
4P ₂	second quadrupole of the ISORI instrument
8P	octopole of the ISORI instrument
B3LYP	Becke, 3-parameter, Lee-Yang-Parr hybrid DFT functional
Ala	alanine
CC	coupled clusters
CASSCF	complete active state self-consistent field
CASPT2	complete active space second-order perturbation theory
CID	collision-induced dissociation
D3	Grimme's dispersion correction
DFT	density functional theory
ESI	electrospray ionization
F-C	Franck-Condon
FEL	free electron laser
F1	fluorescein
FWHM	full-width at half-maximum
G3BJ	Grimme's dispersion correction with Becke-Johnson dumping
HOMO	highest occupied molecular orbital
HPLC	high-performance liquid chromatography
HTI	hemithioindigo
ICR	ion cyclotron resonance
Int	intensity
IR	infrared
IRMPD	infrared multiphoton dissociation
IRPD	infrared photodissociation
ISC	intersystem crossing
ISORI	Infrared spectroscopy of reaction intermediates (instrument)
LMCT	ligand-to-metal charge transfer
LUMO	lowest occupied molecular orbital
M06L	Minnesota pure DFT functional
Me	methyl
MLCT	metal-to-ligand charge transfer
MS	mass spectrometry

<i>m/z</i>	mass-to-charge ratio
Nd:YAG	neodymium-doped yttrium aluminum garnet
NG	noble gas
OPA	optical parametric amplifier
OPO	optical parametric oscillator
PD	photodissociation
PPS	photostationary state
QPB	quadrupole bender
Rh	rhodamine
SOMO	singly-occupied molecular orbital
TD-DFT	time-dependent density functional theory
TICT	twisted intramolecular charge transfer
Trp	tryptophan
Tyr	tyrosine
UV	ultraviolet
vis	visible
w4PT	wire-quadrupole trap of the ISORI instrument
ω B97X-D	long-range corrected hybrid DFT functional
ZPE	zero-point energy

TABLE OF CONTENTS

1	Introduction.....	1
2	Aims of the work	3
3	Ion spectroscopy	4
3.1	Ion generation and trapping	4
3.2	Ion photodissociation	8
3.3	Tagging with noble gases.....	12
3.4	Ion spectroscopy light sources	15
3.5	Interpretation of PD spectra and selected PD studies	16
4	Experimental section.....	31
4.1	Materials.....	31
4.2	Ion generation.....	31
4.2.1	Rhodamine ions	31
4.2.2	Iron(III) azide ions	32
4.2.3	Hemithioindigo ions	32
4.3	Ion spectroscopy instrumentation	32
4.4	Further experimental details.....	39
4.5	Theoretical details	44
5	Results and discussion	49
5.1	Visible photodissociation spectra of rhodamine ions and tagging and temperature effects.....	49
5.1.1	Introduction.....	50
5.1.2	Helium-tagging PD spectra of rhodamine ions.....	51
5.1.3	Tagging effect	54
5.1.4	Temperature effects on photodissociation spectra	59
5.1.5	Multiphoton character of photodissociation spectra.....	64
5.1.6	Further insight into the photodissociation of xanthene dyes	65
5.1.7	Conclusion	76

5.2	Photodissociation of iron(III) azides	78
5.2.1	Introduction.....	79
5.2.2	Photodissociation spectroscopy of iron azide 1 in the vis region	81
5.2.3	Corroboration of the spin crossover of 1 by infrared spectroscopy.....	86
5.2.4	Investigation of thermal spin crossover in other iron(III) azides.....	88
5.2.5	Conclusion	97
5.3	Photoisomerization of hemithioindigo molecular switch in the gas phase	98
5.3.1	Introduction.....	99
5.3.2	Results from the condensed phase	100
5.3.3	Results from the gas phase – infrared spectroscopy	102
5.3.4	Results from the gas phase – electronic spectroscopy	103
5.3.5	Hemithioindigo photoisomerization in the gas phase.....	106
5.3.6	Discussion.....	108
5.3.7	Hemithioindigo complexes with betaine	111
5.3.8	Conclusion	116
6	General conclusions	117
7	References and notes	118

1 INTRODUCTION

Electronic transitions enabled by ultraviolet or visible light absorption govern chemical, physical and biological processes by transforming molecules from their ground to their excited electronic states. Absorption energy and efficiency are directly related to intrinsic molecular properties, including HOMO and LUMO energies, ground and excited state geometries and symmetries, and intra- and intermolecular interactions, which are further affected by the polarity and temperature of the surrounding environment (among other properties). The combination of these effects accounts for the complex molecular information translated into electronic UV/vis spectra.

Typically, UV/vis spectra are recorded in the condensed phase with a solvent. The studied molecule is dissolved in and interacts with the solvent. Thus, depending on the polarity of the solvent and studied molecule (both in its ground and excited state), the absorption maxima of electronic transitions are affected and will shift either to longer or to shorter wavelengths. In addition, the solvent also affects the lifetime of excited states, which causes changes in absorption bandwidth. Another factor which strongly affects UV/vis spectra is temperature. Under standard experimental conditions, *i.e.*, laboratory temperature, the molecules show various populations of vibrational (and rotational) energy levels; hence, the resulting electronic spectra represent a superposition of different vibrationally excited molecules. For this reason, typical absorption bands are broad and usually lack vibrational resolution, thus providing limited information on the structure of excited states. Performing experiments with cooled or gaseous samples generally results in enhanced vibrational resolution; however, such experimental techniques are often unsuitable.

In general, UV/vis spectroscopy provides valuable information on the electronic structure of molecules. However, in the following contexts, UV/vis spectroscopy commonly fails when: 1) reactive intermediates have limited lifetimes and low concentrations, 2) intermolecular interactions (*e.g.*, with the solvent or with counter ions) and aggregation have unwanted effects on the studied molecules, 3) mixtures of compounds contain more than one absorbing species, which makes it difficult to interpret the spectra.

The limitations of scenario (1) can be overcome when performing matrix isolation and time-resolved spectroscopy experiments, which track the formation and fate of reactive species under cryo conditions and on ultrashort time scales,

respectively. Scenario (2) requires using nonpolar solvents or sample vaporization, both of which suppress intermolecular interactions. However, they are not a general solution for this problem because many molecules, especially those containing charged functional groups, cannot be easily dissolved in nonpolar media or vaporized. Lastly, scenario (3) cannot be addressed by conventional UV/vis spectroscopy methods because UV/vis spectra always result from the superposition of the spectra of all absorbing species present in the sample. Hence, different experimental approaches must be used to tackle these issues and to access the spectroscopic properties of the studied molecules.

Undoubtedly, mass spectrometry is a well-suited method for all aforementioned scenarios. In fact, mass spectrometry has proven advantageous in studies on reactive intermediates and on molecules present in complex mixtures at low concentrations thanks to its ability to analyze each component of a sample independently, with no interference from other molecules.¹⁻³ The studied molecules are separated according to their mass-to-charge (m/z) ratio and isolated under well-defined conditions (pressure, temperature), thereby eliminating undesired effects of the surrounding solvent environment and canceling all intermolecular interactions.

Despite its advantages, traditional mass spectrometry presents some drawbacks. The separation and characterization of molecules based on their m/z ratio limits the application of mass spectroscopy to charged molecules. In addition, mass spectroscopy provides limited information on the electronic and structural properties of the studied molecules, except when performing collision induced dissociation experiments,^{4,5} from which some structural insight can be gained. Fortunately, in recent decades, researchers have addressed this significant drawback by combining mass spectrometry with other spectroscopy methods, particularly UV/vis and infrared spectroscopy. As a result, a new research field has emerged: ion spectroscopy.⁶⁻⁸

Ion spectroscopy allows us to record UV/vis and infrared spectra of nearly all ions under variable experimental conditions (*e.g.*, temperatures ranging from room temperature to a few Kelvin) while benefiting from all the advantages of traditional mass spectrometry methods, most importantly mass selection. Moreover, the combination of mass and optical spectroscopy opens new research opportunities for studies of photochemical processes at the molecular level while simultaneously providing invaluable information without unwanted effects caused by the solvent or other molecules.

2 AIMS OF THE WORK

Using the ion spectroscopy techniques and the ISORI instrument:

- Evaluate the effects of experimental parameters (*e.g.*, tagging and temperature) on electronic spectra of selected fluorescent dyes in the gas phase and perform experimental calculations to support experimental observations. Furthermore, develop the experimental scheme for recording temperature-dependent photodissociation spectra.
- Investigate the underlying processes involved in the photochemical conversion of iron(III) azides into iron(V) and iron(II) complexes.
- Investigate the C=C photoisomerization process in the hemithioindigo molecular switch and compare the gas-phase data with those obtained in condensed-phase studies.

3 ION SPECTROSCOPY

The principles, methods and instrumentation of ion spectroscopy are mainly based on well-known and established mass spectrometry techniques and instruments. In addition, an ion spectroscopy setup contains a suitable light source, which provides access to electronic and infrared spectra of ions.

This chapter describes and discusses features of ion spectroscopy experiments, including the initial generation of ions, their interaction with light using common light sources and, most importantly, the underlying photodissociation (PD) process of ion spectroscopy. Furthermore, the Introduction showcases mainly the ion spectroscopy methods that are relevant to this Thesis, focusing on spectroscopy in the UV/vis range, and provides a brief overview and discussion on results previously acquired by ion spectroscopy.

3.1 ION GENERATION AND TRAPPING

Firstly, an ion spectroscopy experiment starts similarly to any other routine mass spectrometry experiment. The ions of interest are either transferred from the solution to the gas phase or directly generated in the gas phase from a viable chemical precursor. Both procedures involve the use of a suitable ionization technique. Various ionization methods are available in mass spectrometry; currently, the most popular methods are electrospray ionization (ESI), for polar organic molecules and metal complexes, and matrix-assisted laser desorption/ionization, for biomolecules. Other commonly used techniques include atmospheric pressure chemical ionization, electron impact ionization and laser desorption.⁹

Electrospray ionization is arguably the most commonly used ionization technique in ion spectroscopy, mainly because ESI readily transfers various ions from their solution to the gas phase under soft ionization conditions, with no special sample preparation or on experimental setup requirements.^{10,11} Figure 1 shows a simplified scheme of an ESI interface. The sample solution passes through a capillary to a metal needle when applying several kilovolts of voltage. This generates the Taylor cone and subsequently a jet of charged droplets in which solvated ions gradually lose surrounding solvent molecules and enter the mass spectrometer. The ESI technique is convenient for the ionization of both small and large organic (bio)molecules, particularly charged or easily ionized or protonated/deprotonated molecules.

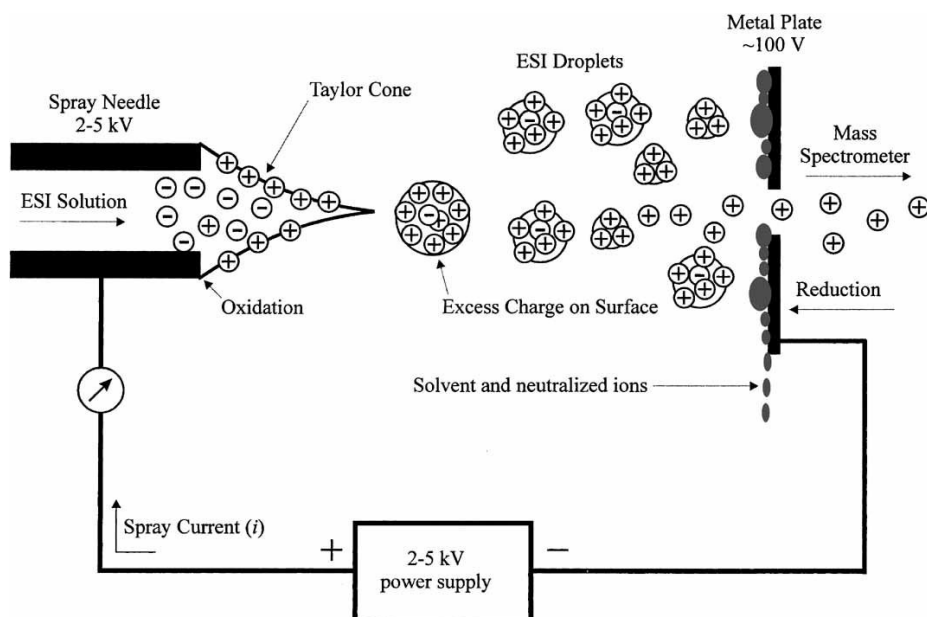


Figure 1. Scheme of the electrospray ionization interface. Reprinted from ref. 10 with permission. Copyright John Wiley & Sons, Inc (2001).

The next stage of an ion spectroscopy experiment involves mass selection in which the ions of interest are separated from the others that had entered the mass spectrometer. Commonly used mass filters include quadrupole ion guides, which differentiate ions based on their mass-to-charge ratio (m/z).¹² Mass selection is one of the most crucial advantages of both mass and ion spectroscopy over any other analytical method because it enables us to study components (ions) of a sample individually.

After mass selection, the studied ions, characterized according to their m/z ratio, are trapped and subsequently irradiated with photons, photodissociating, and then their spectrum is recorded (Chapter 3.2). Initially, most experiments used ion cyclotron resonance (ICR) cells. The ICR technique is based on the movement of ions in a magnetic field.¹³ The irradiation of ions in ICR cells was accomplished using xenon arc lamps equipped with monochromators or tunable dye lasers.

Soon after the emergence of the first photodissociation experiments, researchers mainly focused on radical cations of organic molecules, primarily because of their straightforward generation in the gas phase, reactive nature and rich electronic spectroscopy.¹⁴ Figure 2 shows one of the first electronic spectra recorded in the gas phase, the spectrum of CH_3Cl^+ ions trapped inside an ICR cell, which was reported in 1971 by Dunbar, who monitored the production of CH_3^+ ions by CH_3Cl^+ photodissociation using a xenon arc lamp and a monochromator.¹⁵

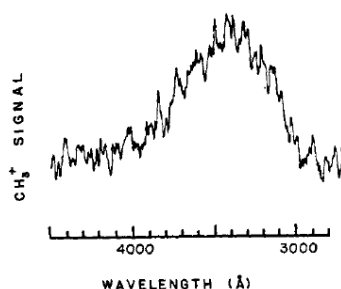


Figure 2. One of the first photodissociation spectra of a polyatomic ion, CH_3Cl^+ , recorded when monitoring production of CH_3^+ ions dissociating from CH_3Cl^+ parent ions by light. Reprinted from ref. 15 with permission. Copyright American Chemical Society (1971).

In addition to absorption properties, studies have often focused on other properties of photodissociating ions, such as dissociation mechanisms and kinetics or dissociation energies.¹⁶⁻¹⁸ Moreover, multiple studies have probed the structure of ions, especially those with several possible isomers with the same m/z ratio, which are hence undistinguishable when using traditional mass spectrometry methods. One of the first examples of such studies is the photodissociation of isomeric $\text{C}_9\text{H}_{12}^+$ ions, which clearly differentiated conjugated 1- and 3-phenylpropene and nonconjugated cyclopropylbenzene radical cations.¹⁹ Another early example is provided in Figure 3, which shows $\text{C}_3\text{H}_5\text{Cl}^+$ isomers distinguished based on their different vibrational structure.²⁰ More recently, the capacity of photodissociation spectroscopy to characterize and differentiate isomeric ions based on their PD spectra has become the main objective of numerous photodissociation studies,²¹ including those on biomolecules, such as small peptides,²² in which even isomers and conformers can be identified and distinguished according to their absorption patterns in high-resolution UV photodissociation spectra.

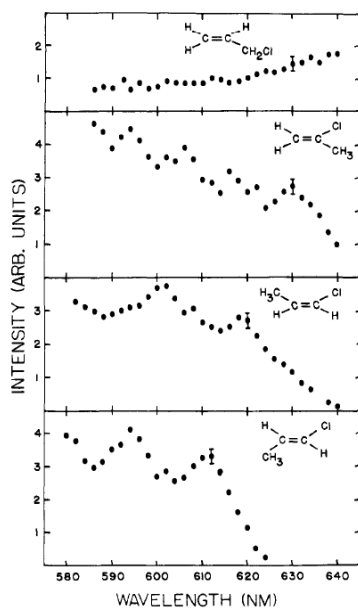


Figure 3. Photodissociation spectra of four isobaric $C_3H_5Cl^+$ ions, each of which shows a distinct vibronic structure, thus allowing straightforward structural assignments. Reprinted from ref. 20 with permission. Copyright American Chemical Society (1978).

Currently, ion spectroscopy instruments most often rely on ion storage in linear radio frequency ion traps.^{8,23,24} They are generally more advantageous than ICR cells thanks to their lower cost, better commercial availability and higher sensitivity, in addition to their overall operational simplicity. Linear ion traps (and also multipole ion guides) are constructed from an even number (commonly 4, 6, 8, 22, or 24) of linear, ideally hyperbolic but more often, cylindrical metal rods (in some cases wires) arranged symmetrically around a central axis. The number of rods is commonly known as the number of poles; thus, ion traps are referred to as quadrupole, octopole or 22-pole traps, among others. A direct current potential is applied to all multipole rods, with alternating negative and positive voltages, which creates a multipole field inside the multipole ion trap or guide.²⁵ At this point, ions are attracted to multipole rods and thus eventually collide with them. However, when applying a radio frequency voltage (instead of a static field) to one set of rods and an equal radio frequency voltage with the opposite amplitude to the other set of rods and when changing the field very fast, the cloud of ions remains along the multipole central axis.

Importantly, the shape of the multipole effective potential depends on the number of rods.²⁴ Ions in multipoles with a higher number of poles will gradually experience a smaller increase in effective potential when moving towards the poles.

This means that ions can occupy larger volumes in the center of the multipole, which has some advantages, such as the possibility to perform experiments with high ion densities or to eliminate space charges.

The last phenomenon used in ion trapping is collisional cooling (also referred to as thermalization or buffer gas cooling).²⁶ Ions generated in ion sources generally have high kinetic energy, which makes it difficult to trap them. To remove their excess energy, a neutral gas (typically helium or hydrogen) is injected through a gas inlet into the ion trap. The neutrals collide with ions many times, and the energy of ions is gradually transferred to the neutrals. Consequently, the ions lose their kinetic energy, and their internal degrees of freedom are cooled.

3.2 ION PHOTODISSOCIATION

Unlike standard direct absorption UV/vis and IR experiments in the condensed phase, experiments with isolated ions in the gas phase are unable to monitor changes in the intensity of light after it passes through a sample because samples in the gas phase are optically diluted, with only hundreds to thousands of trapped ions. Thus, the resulting changes in light intensity are undetectable. A different outcome of ion-photon interactions is therefore monitored in ion spectroscopy experiments, and only a handful of exceptions to this general feature, such as direct rovibrational absorption spectrum of isolated H_3^+ ions reported by Oka in 1980,²⁷ have been published thus far.

When ions confined in vacuum absorb energy by electronic excitation, the gained energy cannot be simply dissipated by intermolecular interactions because such interactions do not occur in the gas phase. Instead, the ions retain the absorbed energy, redistributing it within their scaffold. If the absorbed energy reaches an energy threshold for dissociation of a specific chemical bond, this bond is broken, the ion dissociates and its internal energy thus decreases. Absorption-induced ion fragmentation, termed photodissociation (PD),^{17,28-30} is then readily monitored by mass analysis and detection of photodissociation products, similarly to well-established MS experiments; for instance, collision induced dissociation (CID) or ion-molecule reactions. Photodissociation spectra are constructed by plotting the fragmentation yield as a function of photon energy. Alternatively, light-induced changes in the intensity of a parent ion signal can be monitored in photodissociation experiments.

The photodissociation process necessarily starts with UV or visible photon absorption and transition to the electronic excited state. In addition to photodissociation, the absorbed energy can trigger other, often faster, non-radiative processes, for example, radiative cooling,^{31,32} electron detachment,³³⁻³⁶ or fluorescence,³⁷⁻³⁹ which may occur simultaneously and compete with photodissociation. Ultimately, fluorescence is one of the main processes that reduces photodissociation efficiency and yield and is especially pronounced in ions with high fluorescence quantum yields.^{40,41} In turn, if the non-radiative processes, which lead to photodissociation, are rapid, or in other words, if the excited state rapidly decays, the resulting PD spectra generally exhibit broad, unresolved absorption features.^{42,43}

Collisions between excited ions and the buffer gas can be another competing non-radiative deactivation process (termed collisional deactivation). The efficiency of collisional deactivation depends on the buffer gas pressure in the ion trap, which is typically easy to control. Hence, if undesirable, collisional deactivation can be avoided by irradiating ions after the buffer gas pressure drops by vacuum pumping. Lastly, an apparent factor, which affects photodissociation, as well as other electronic spectroscopies, is the oscillator strength of electronic transition.

The mechanism of the photodissociation process can be rather complex and mainly depends on the intrinsic nature of the studied ion. If the energy gained by absorption of one photon is higher than the bond dissociation threshold, the occurring photodissociation can be a one-photon process. However, the energy of one photon (especially of infrared photons, *vide infra*) is most often insufficient to break a covalent bond; hence, in these cases, photodissociation is a two- or a multiphoton process involving sequential absorption of multiple photons.^{40,44} Experimentally, the multiphoton nature of the photodissociation process is demonstrated by the nonlinear response of the photodissociation yield to the power of the incident light and by the variation of photodissociation as a function of pressure. Despite the multiphoton nature of photodissociation, the PD spectra should always directly relate to the optical spectrum of the studied ion because the energy of the first absorbed photon equals the energy of the electronic (or vibrational) transition to the excited state.

Photodissociation involving two-photon absorption was first documented in a study on benzene radical cations;⁴⁵ soon thereafter, other studies on benzene^{18,46,47} and naphthalene derivatives^{48,49} emerged, also evidencing two-photon photodissociation

mechanisms. Figure 4 shows the suggested mechanism for a two-photon photodissociation process adapted from the work by So and Dunbar.⁴⁰ The first UV/vis photon (1) excites the ion from its ground state (\tilde{X}) to its first excited state (\tilde{B}). Because the dissociation threshold is not reached, the ion relaxes back to its ground electronic state by fluorescence (2); however, a small part of the absorbed energy is retained, thereby increasing the population of vibrationally excited ions in the ground electronic state, *i.e.*, the ions are heated.⁵⁰ This ion heating process is referred to as fluorescence pumping. Although fluorescence pumping can be repetitive, it does not account for the photodissociation alone. Eventually, the vibrationally hot ions absorb a second photon (3), and their energy surpasses the bond dissociation threshold (E_d). Therefore, dissociation occurs.

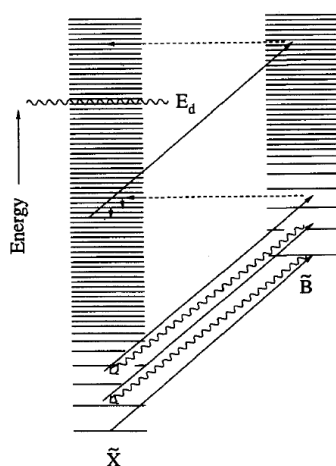


Figure 4. Suggested mechanism of a two-photon photodissociation including rapid fluorescence pumping, which results in a vibrationally excited ion in its ground electronic state (\tilde{X}). Such photodissociation mechanism has been reported to operate in the photodissociation of 1,3,5-trifluorobenzene and hexafluorobenzene molecular cations. Reprinted from ref. 40 with permission. Copyright AIP Publishing (1989).

A photodissociation mechanism involving several absorption/fluorescence cycles has also been suggested to operate in the photodissociation of rhodamine dyes,⁵¹⁻⁵³ which are highly fluorescent in solution and presumably in the gas phase also. Two mechanisms were proposed based on experimental data and kinetic modeling;⁵¹ the first is similar to the aforementioned fluorescence pumping mechanism in which the ion slowly gains vibrational energy before dissociation (Figure 5a). The second

mechanism involves a rare, non-radiative event, such as intersystem crossing (ISC), which converts the ion from its excited state S_1 into its triplet state T_1 (Figure 5b). Under gas-phase conditions (isolated ion), the triplet state is unable to relax to the ground singlet state S_0 . Consecutively, excitation of the triplet state to a higher excited state ultimately triggers photodissociation. Moreover, a similar mechanism involving dissociation from the triplet state has been shown in small protonated phenylalanine- and tyrosine-containing peptides.⁵⁴

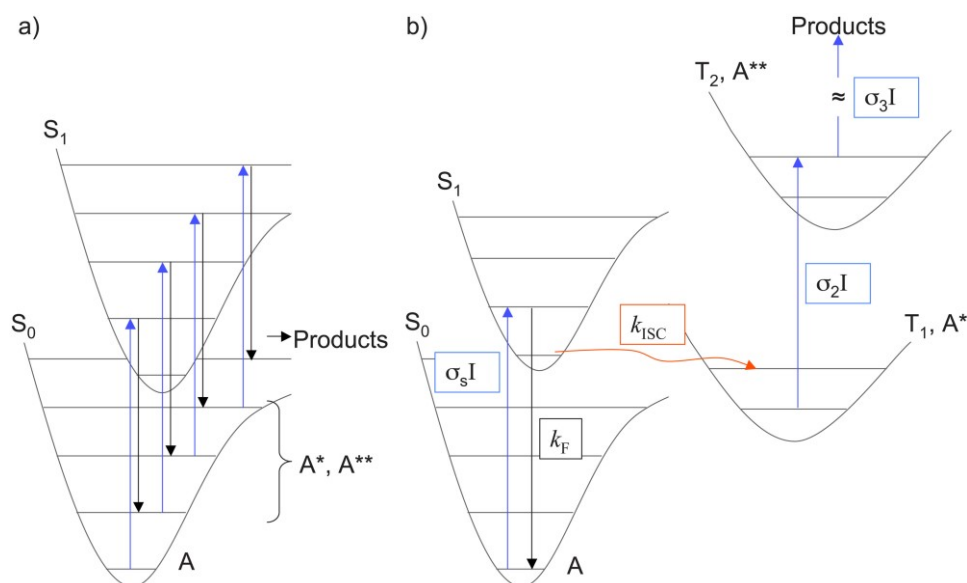


Figure 5. Proposed photodissociation mechanism of rhodamine 575 in the gas phase. (a) After three absorption/emission cycles, the fourth absorption/emission cycle promotes dissociation from an unbound vibrational state of S_0 . (b) Rare intersystem crossing (ISC) interrupts the absorption/fluorescence cycle, and dissociation occurs after consecutive photon absorption at the triplet potential energy surface. Reprinted from ref. 51 with permission. Copyright AIP Publishing (2008).

Moreover, experiments have also shown that photodissociation can be a combination of one- and two-photon processes, based on the excitation energy. For example, the photodissociation of bromobenzene cation in the UV range is a one-photon process (Figure 6).¹⁶ Conversely, the variation of pressure with photodissociation in the vis range suggests that the absorption of the first photon is followed by collisional deactivation by a buffer gas. At lower pressures, collisional deactivation becomes inefficient; thus, the excited ions retain their gained energy, and absorption of the second vis photon triggers the dissociation.

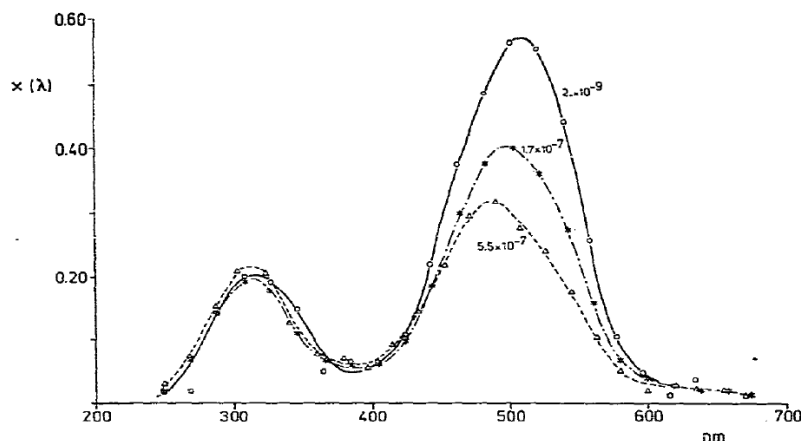


Figure 6. Photodissociation spectra of bromobenzene molecular ion as a function of pressure, which suggest that photodissociation is a two-photon process in the vis region and a one-photon process in the UV range. Reprinted from ref. 16 with permission. Copyright AIP Publishing (1981).

Importantly, in addition to UV/vis photons, infrared photons can also be used to photodissociate ions by exciting their vibrational levels. This experiment provides infrared spectra of ions. However, IR photons are much less energetic, thus the absorption of dozens to hundreds of IR photons is necessary for reaching bond dissociation thresholds. This technique is referred to as infrared multiphoton photodissociation (IRMPD)⁵⁵⁻⁵⁸ and requires using rather powerful infrared lasers (Chapter 3.4). Moreover, the multiphoton nature of IRMPD process generally results in line-broadened, red-shifted and even completely absent spectral features. Despite these significant drawbacks, many studies have reported the successful use of IRMPD for the structural elucidation of ions,⁵⁷ including reaction intermediates,^{59,60} metal clusters⁶¹⁻⁶³ and biomolecules.⁶⁴⁻⁶⁶ IRMPD technique has now been surpassed by the single-photon technique, which is described below. Nevertheless, both multiphoton electronic and multiphoton infrared photodissociation techniques require a careful data analysis; possible limitations and consequences of multiphoton absorption process should always be addressed when using these techniques.

3.3 TAGGING WITH NOBLE GASES

The photodissociation techniques discussed so far generally involve multiphoton processes. These processes can significantly affect PD spectra, which require high-intensity incident light for detectable ion fragmentation. Nevertheless, advances

in the fields of tunable bench-top laser sources and cryogenic multipole ion traps have enabled the development of widely applicable single-photon photodissociation methods involving tagging with a noble gas.⁶⁷⁻⁶⁹ These techniques operate at cryogenic temperatures, and consequently they have been sometimes described as equivalent to matrix-isolation experiments.

The tagging technique involves trapping and cooling ions to several Kelvin (typically 3–20 K) inside a cryogenically cooled ion trap. Under such conditions, most ions are relaxed and cooled, populating their ground vibrational level. Moreover, the atoms (or diatomic molecules) of an inert buffer gas (usually a noble gas (NG), such as helium,⁶⁷⁻⁷³ neon,⁷³⁻⁷⁶ argon,^{71, 73,76-80} krypton⁷³ or other inert gas, *e.g.*, hydrogen^{71,73,78,81} or nitrogen^{73,76,82}) form weakly bound van der Waals complexes with cooled ions $[M^+-NG]$ (Scheme 1). The binding energy of the tag is very low;⁸³ thus, the ion structure should only be negligibly perturbed by bonding to a tag. Subsequently, irradiation of $[M^+-NG]$ complexes with a UV/vis or IR photon, which is resonant with an electronic or vibrational transition of $[M^+-NG]$ (virtually of unperturbed M^+), increases the internal energy that dissipates by dissociation of the weakly bound tag. Subsequently, the photodissociation of $[M^+-NG]$ complexes is monitored as a function of photon energy, which provides a tagging UV/vis or IR photodissociation (IRPD) spectrum. The resulting $[M^+-NG]$ spectrum is directly related to the spectrum of the bare M^+ ion because structural changes introduced by tagging are generally negligible.^{67,68}



Scheme 1. Scheme of the photodissociation method involving ion tagging with a noble gas (NG). A UV/vis or IR photon is absorbed if its frequency is resonant with one of the electronic or vibrational transitions of $[M^+-NG]$. NG = He, Ne, Ar or an inert gas, such as H₂, N₂.

The photodissociation of the tag is almost always a one-photon process because the binding energies are even lower than the energies of far-infrared photons (<600 cm⁻¹).⁸³ Relatively low-power light sources, such as commercial bench-top tunable UV/vis and infrared laser systems (Chapter 3.4), are conveniently powerful

enough to induce detectable photodissociation. Moreover, ion spectroscopy instruments used for tagging experiments are becoming increasingly more available.

Although the tagging atom generally binds to the ion very weakly, few reports have shown that tagging may cause significant structural and even electronic changes in the studied ions. For instance, argon tag binding to $[\text{Ti}(\text{H}_2\text{O})]^+$ ions changed the spin ground state from quartet to doublet;⁸⁴ both helium and neon tags significantly perturbed the structure and the resulting IR spectrum of a very reactive $[\text{CHCl}]^{2+}$ ion;⁷⁴ in addition, the binding of a single helium to $[\text{FeO}]^+$ ion was strong enough to hinder the photodissociation of $[\text{FeO}\cdot\text{He}]^+$ ions by infrared photons.⁸⁵ Instead, $[\text{FeO}\cdot\text{He}_n]^+$ ($n = 2, 5, 6$) complexes were examined and successfully photodissociated to obtain the $\text{Fe}=\text{O}$ vibration frequency. Surprisingly, helium-tagging does not perturb the highly fluxional and reactive CH_5^+ ion.⁸⁶ More recently, researchers have reported a systematic study on tagging atom (He, Ne, Ar, Kr, H_2 , D_2 , N_2) effects on electronic spectra of the C_{60}^+ ion and showed that tagging atoms indeed caused only negligible shifts (*ca.* 2–5 cm^{-1}).⁷³

Despite all aforementioned issues described in studies on very reactive ions, helium has always been considered the most “innocent” tagging atom, only negligibly affecting the structures of ions and their photodissociation spectra.^{67,68} Accordingly, helium-tagging photodissociation spectroscopy is becoming an increasingly popular technique and the method-of-choice in many ion spectroscopy applications,⁶⁸ as shown by the first experimental assignment of two diffuse interstellar bands to the fullerene C_{60}^+ ion.⁸⁷

It should be noted that a prerequisite for successful helium-tagging is an experimental setup that reaches ion trap temperatures of a few Kelvin and high number densities of helium buffer gas.^{26,67} Higher temperatures increase the internal energy in helium complexes, which rapidly decay because the helium tag is only weakly bound (binding energies below 0.1 kcal mol^{-1} in complexes with common ions). Because reaching temperatures around 3–6 K places higher technical demands on experimental setups, some research groups have instead applied tagging using different tags with higher binding energies than helium, such as argon or nitrogen. In those cases, higher experimental temperatures (~ 20 K or even more) suffice for successful tagging and photodissociation experiments. However, photodissociation spectra should be carefully interpreted because tagging with more tightly bound tags, such as atoms heavier than

helium, can in principle perturb the structure of the studied ions (*vide supra*). Moreover, elevated temperatures may affect those spectra, causing, *e.g.*, line broadening and spectral congestion (*vide infra*).

3.4 ION SPECTROSCOPY LIGHT SOURCES

All ion spectroscopy experiments require light sources with widely tunable wavelengths in UV/vis or IR spectral regions. Multiphoton methods, in which absorption of multiple photons is necessary for photodissociation, generally demand rather powerful light sources, such as free-electron lasers (FEL). To date, a handful of FEL facilities (FELIX in Nijmegen, Netherlands,⁸⁸ CLIO in Orsay, France,⁸⁹ and FEL in Berlin, Germany,⁹⁰ among others) have been constructed and actively used for ion spectroscopy experiments. However, the high building and operational costs of FEL facilities limits their number and hence their availability for researchers.

Historically, the first photodissociation instruments used a xenon arc lamp with wavelength filters (*e.g.*, Figures 2 and 3, for other examples please refer to Chapter 3.2). Their use has been however rapidly surpassed by dye lasers, which offer a more convenient way of wavelength tuning. Yet again, in recent years, even dye lasers have been surpassed in many ways by more recently developed tunable laser sources based on non-linear optical devices.

Advances in laser technology, nonlinear optics and materials science in the last few decades have enabled the development of commercial bench-top tunable laser sources, specifically optical parametric oscillators (OPO).⁹¹ Briefly, OPO device consists of a pumping continuous-wave or pulsed pump laser, typically a Nd:YAG laser emitting at 1064 nm, an optical oscillator and a nonlinear optical crystal. The pump laser wave passing through the OPO optical elements is converted into two output waves, signal and idler, whose wavelengths can be tuned in wide tuning ranges spanning from UV through vis to IR ranges of the electromagnetic spectrum. Thus, wavelengths inaccessible by other lasers or light sources can be readily generated by OPO systems. Additionally, OPOs feature a narrow linewidth and high-power outputs, which render them valuable tools. As a result, they are becoming increasingly widespread in laser laboratories in many scientific fields, particularly in ion spectroscopy. In fact, because of their advantages, OPOs are already preferred over FELs in many ion spectroscopy research areas, thus clearly showing a trend towards

single-photon techniques. However, even OPO technology and its use remains limited in some research areas, specifically in far-infrared spectroscopy because OPO setups technically cannot reach frequencies below 600 cm^{-1} . Nevertheless, the development of new nonlinear materials will eventually overcome this restriction and further enhance OPO technology and its use. Until then, studies in the far-IR spectra region remain the domain of FEL setups, as demonstrated in the recent study on copper clusters in the $70\text{--}280\text{ cm}^{-1}$ spectral region.⁹²

3.5 INTERPRETATION OF PD SPECTRA AND SELECTED PD STUDIES

NOTE: Throughout this Thesis, *helium-tagging method/spectrum* (alternatively *argon-* or *nitrogen-tagging, etc.*) corresponds to an ion spectroscopy photodissociation experiment in which the dissociation of weakly bound tag was monitored (at cryogenic temperatures). Similarly, *photodissociation method/spectrum* corresponds to an ion spectroscopy photodissociation experiment in which the dissociation of some specified molecular fragment was monitored (at wide temperature range).

Ion transfer into the gas phase eliminates all intermolecular interactions present in the condensed phase, most importantly those between the ion and solvent molecules. This typically leads to substantial shifts (from hundreds to thousands of wavenumbers) in absorption maxima of electronic PD spectra with respect to those of solution absorption spectra. For instance, if the electronic excited state of a molecule is more polar than the electronic ground state, or if the excited state has a charge-transfer character,⁹³ the lack of polar solvent molecules in the gas phase will destabilize the excited state and increase the excitation energy; hence, the excitation energy shifts to higher wavenumbers (blue-shift). Similarly, if the more polar electronic ground state is destabilized by the absence of solvent, its energy level will increase; hence, the excitation energy shifts to lower wavenumbers (red-shift).

Both of these effects have been well documented in photodissociation studies on fluorescein dyes (Figure 7).^{34,94} The spectra of cationic fluorescein dyes showed a blue-shift of absorption maxima, explained by the destabilization of their excited states in the gas phase, and the spectra of anionic fluorescein dyes showed a red-shift of absorption maxima, attributed to the destabilization of their ground state in the gas phase. Similarly, several other gas-phase photodissociation studies have reported blue-shifts of absorption maxima with respect to data from the condensed phase for cationic

xanthene dyes, such as rhodamines 575, 590 and 6G,⁵³ rhodamine B,⁹⁵ rhodamines 590 and 640,⁹⁶ or structurally-related Nile red dye.⁹⁷ Interestingly, an absorption maximum red-shift of 170 nm has been reported for Schiff base retinal chromophore while comparing gas-phase and methanolic solution data.⁹⁸

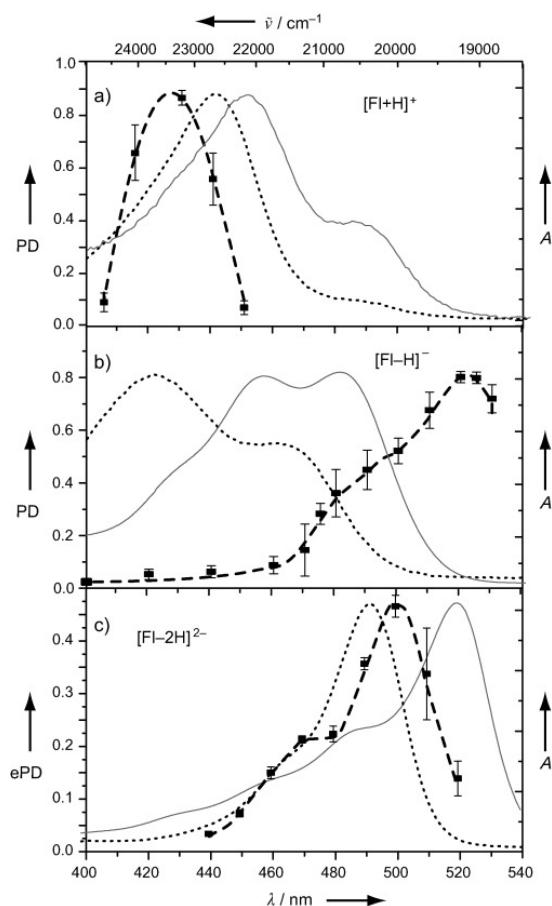


Figure 7. Photodissociation spectra (square data point) of the fluorescein cation ($[Fl+H]^+$, a), anion ($[Fl-H]^-$, b) and dianion ($[Fl-2H]^{2-}$, c). Dashed and solid lines correspond to absorption spectra measured in water and dimethylsulfoxide, respectively. Reprinted from ref. 34 with permission. Copyright Wiley-VCH (2010).

A very important photodissociation factor, which also affects other electronic spectra, is temperature. Firstly, temperature affects the population and interconversion of conformations that a non-rigid ion or a molecule adopts. Each conformation contributes to an overall absorption spectrum, which will be broadened, particularly in solution. In the gas phase and upon cooling, the ions adopt only a few conformations or often a single one, and sufficiently low temperatures preclude isomer and conformer interconversion. Hence, ion cooling has proved crucial for photodissociation studies

on large ions, for example, biomolecules.²² Additionally, isolation in the gas phase generally strengthens intramolecular interactions, for instance hydrogen bonding, which further restricts conversion between isomers and conformers.

Secondly, temperature affects the population of vibrational levels of an electronic state that an ion or a molecule adopts (Figure 8). The thermal population of higher vibrational levels results in the emergence of electronic transitions commonly known as hot bands, which originate from vibrationally excited levels. Consequently, hot bands increase the number of experimentally observed bands and reduce the vibrational resolution.

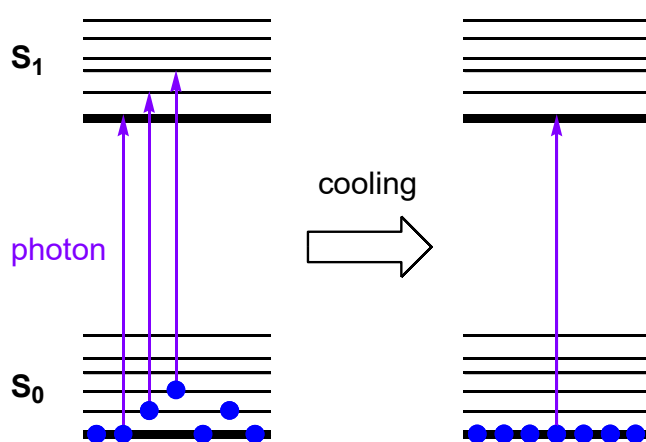


Figure 8. Cooling decreases the number of molecules (blue dots) populating vibrationally excited levels, which improves the vibrational resolution of electronic spectra.

Electronic spectra recorded in solution are strongly temperature-sensitive due to aforementioned effects. Consequently, such electronic spectra often exhibit broad absorption bands with spectral congestion in many cases. In this context, the ability to control the experimental temperature in gas-phase photodissociation studies is highly advantageous because the population of conformational and vibrational levels is reduced at low temperature. Nevertheless, even photodissociation experiments performed at a few Kelvin may still be affected by temperature (*vide infra*).

Figures 9 and 10 illustrate two examples of temperature effect on electronic photodissociation spectra of protonated amino acids.⁹⁹ In the first example, the PD spectrum of protonated tryptophan shows improved spectral resolution upon cooling,

albeit the spectrum measured at 6 K still contains rather broad absorption features (Figure 9). In the second example, reported in the same study, the PD spectrum of protonated tyrosine at ambient temperature also suffers from spectral congestion (Figure 10). In contrast, the spectrum of the same ion cooled to 6 K shows a sharp, well-resolved vibronic structure. Furthermore, differences in band broadness between the PD spectra of protonated tryptophan and tyrosine amino acids suggests that the excited S_1 state of tryptophan decays very rapidly during ultrafast non-radiative processes caused by non-covalent interactions of its indole ring.

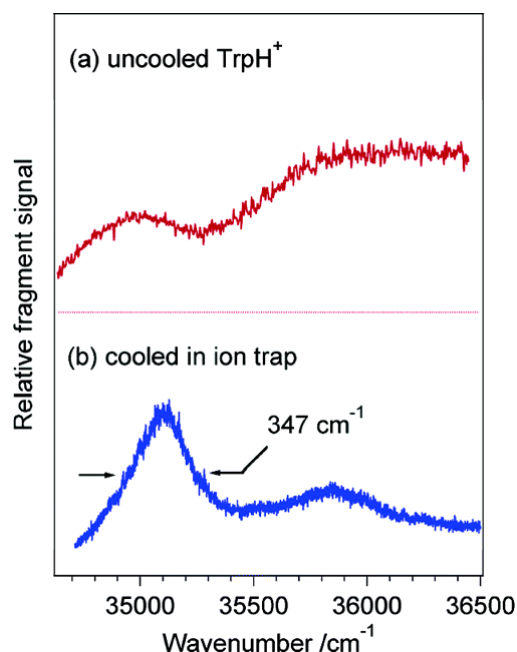


Figure 9. Electronic photofragmentation spectra of protonated tryptophan (TrpH^+) without (a) and with (b) cooling to 6 K in the 22-pole ion trap. Reprinted from ref. 99 with permission. Copyright American Chemical Society (2006).

Since the first photodissociation report,⁹⁹ protonated tyrosine (TyrH^+) has become the standard for assessing temperature effects on electronic spectra of, mostly biomolecular, ions stored in cryocooled ion traps.^{30,100-102} Recently reported temperature-dependent PD spectra of TyrH^+ highlight the importance of cooling ions to the lowest possible temperature for successfully recording vibrationally resolved spectra (Figure 11).¹⁰³ The presence of hot bands (transitions at lower energies than that of the 0–0 transition) in PD spectra of TyrH^+ at elevated temperatures (> 5 K) arises from vibrationally excited ions. Moreover, spectra acquired at increased temperatures

feature band broadening resulting from the increase in the population of higher vibrational and rotational levels, which accounts for unresolved vibronic structures and for a complete loss of spectroscopic information.

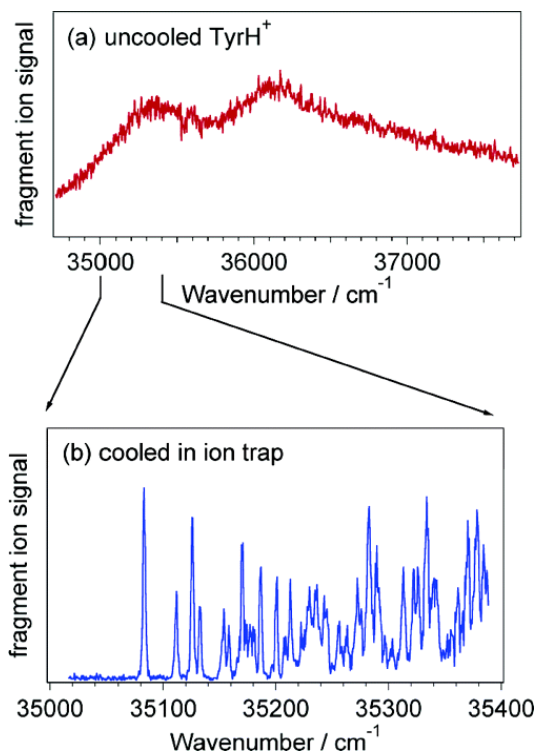


Figure 10. Electronic photofragmentation spectra of protonated tyrosine (TyrH⁺) without (a) and with (b) cooling to 6 K in the 22-pole ion trap. Reprinted from ref. 99 with permission. Copyright American Chemical Society (2006).

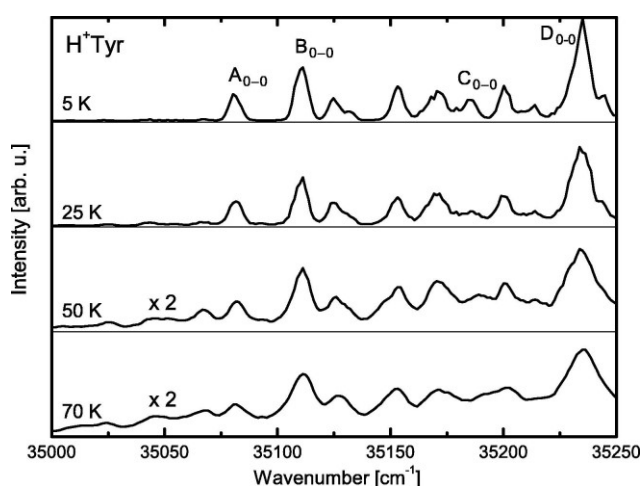


Figure 11. Electronic photofragmentation spectra of protonated tyrosine (TyrH⁺) at different temperatures of the ion trap, A-D denote 0–0 transitions of different conformers. Reprinted from ref. 103 with permission. Copyright Elsevier (2017).

Similar temperature effects have been observed in the photodissociation study of a cooled protonated tyrosine-alanine dipeptide ($[\text{TyrAla}+\text{H}]^+$, Figure 12).¹⁰⁴ As expected, elevating the experimental temperature results in hot bands and in increased band broadness. Interestingly, the photodissociation spectrum of helium-tagged $[\text{TyrAla}+\text{H}]^+$ ions recorded at 6.1 K disagrees with the respective photodissociation spectra, even when recording the latter at the same temperature (*cf.* Figure 12a, blue trace and Figure 12b). The vibrational bands in the helium spectrum are broader and blue-shifted; based on these results, the researchers proposed that binding to helium distorts the electronic structure of $[\text{TyrAla}+\text{H}]^+$ ion or that the spectra correspond to a mixture of conformers. Moreover, they suggested that structural determination of ions based on tagging UV photodissociation data may be problematic in some cases.

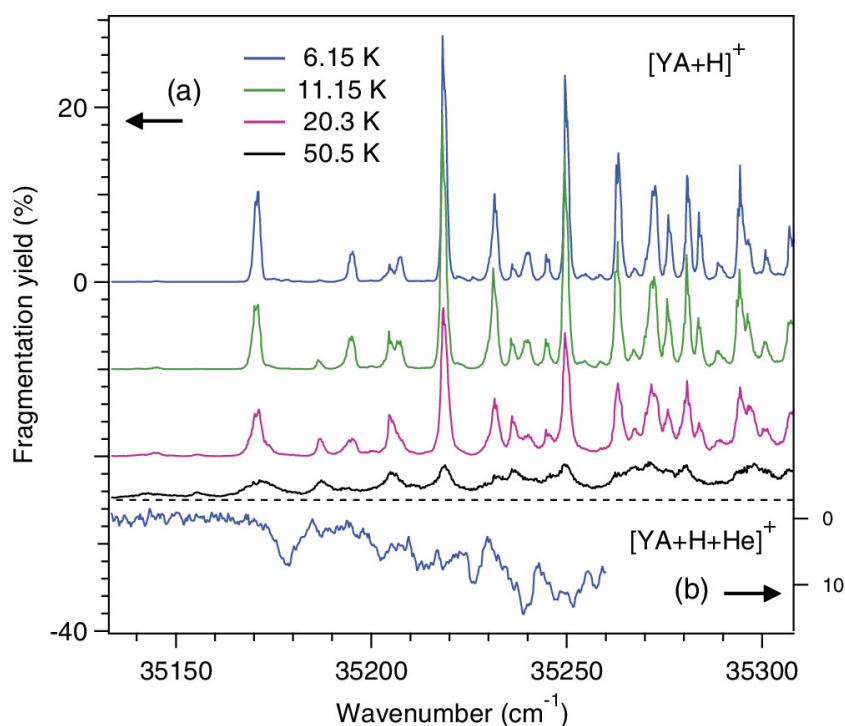


Figure 12. (a) Photodissociation spectra of the $[\text{TyrAla}+\text{H}]^+$ dipeptide recorded at different temperatures. (b) Helium-tagging photodissociation spectrum of the $[\text{TyrAla}+\text{H}]^+$ dipeptide measured at 6.1 K. Reprinted from ref. 104 with permission. Copyright AIP Publishing (2014).

In principle, the use of ESI ionization together with the isolation of ions in the gas phase makes it possible to generate solvated ions with a controlled number

of solvent molecules attached to the studied ion, which provides a smooth connection between bare ions in the gas phase and fully solvated ions in solution. This advantage has been used to further study the complex photophysics of gaseous, protonated tryptophan amino acids interacting with water molecules. Figure 13 shows electronic PD spectra of protonated tryptophan ions with 0, 1 and 2 water molecules attached.¹⁰⁵ The spectrum of protonated tryptophan is broad; however, the sequential addition of water molecules sharpens the absorption features, eventually providing a well-resolved vibronic spectrum (Figure 13). The addition of water molecules clearly prolongs the lifetime of the excited state by diminishing its ultrafast nonradiative decay.

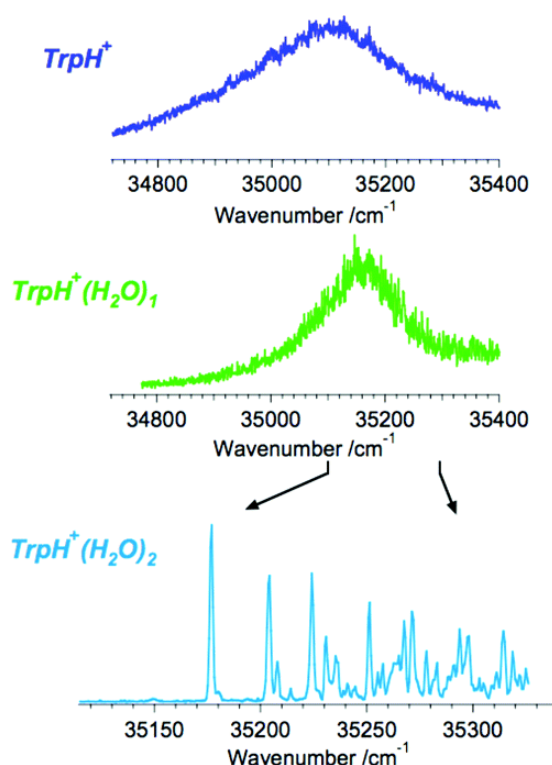


Figure 13. Electronic photodissociation spectra of protonated tryptophan (TrpH^+) with 0, 1, and 2 water molecules attached, measured at 10 K. Reprinted from ref. 105 with permission. Copyright American Chemical Society (2006).

Following the pioneering study of hydrated protonated tryptophan (Figure 13), researchers reported further studies assessing solvation, complexation and temperature effects on electronic photodissociation spectra of cooled biological relevant ions. For instance, PD studies have been reported on complexes of protonated tryptophan and methanol under different temperatures (Figure 14),¹⁰⁶ Many other hydrated ions have

been studied, for example calcium cation,¹⁰² *p*- and *o*-nitrophenolate ions,¹⁰⁷ protonated benzaldehyde,¹⁰⁸ doubly protonated gramicidin S decapeptide with 0–50 waters attached,¹⁰⁹ and penta-hydrated protonated phenol, showing a thermal interconversion between two isomers differing in hydrogen bonding and in the positions of their absorption maxima (Figure 15).¹¹⁰

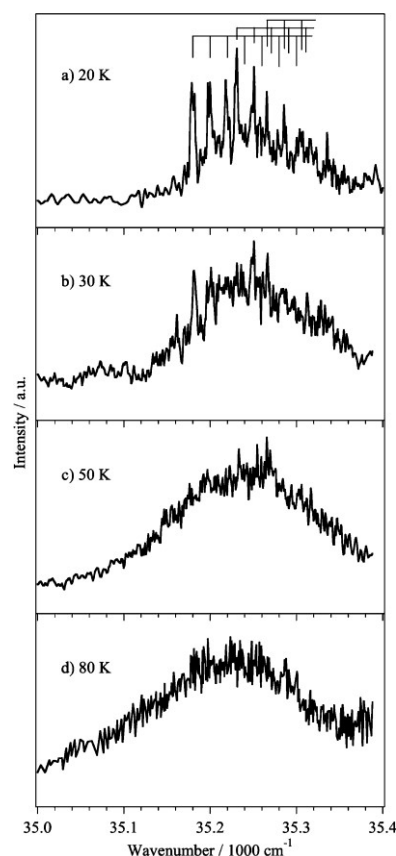


Figure 14. Electronic photodissociation spectra of protonated tryptophan with two methanol molecules attached, recorded at different temperatures. Temperature clearly affects spectral resolution; the population of vibrationally and rotationally excited ions diminishes the resolution at higher temperatures. Reprinted from ref. 106 with permission. Copyright American Chemical Society (2009).

As previously mentioned, one of the main advantages of the ESI ionization technique is its ability to generate solvated ions and clusters. Recently, ESI ionization has been used to create non-covalently bound complexes between the ion of interest and a charged molecule simply by mixing these two components together in solution before ESI ionization. Complexation (“tagging”) with a molecule (similarly to the noble gas tagging technique, albeit only under cryogenic conditions; refer to Chapter 3.3)

has proved advantageous in that only one photon is needed to trigger the photodissociation of this complex.

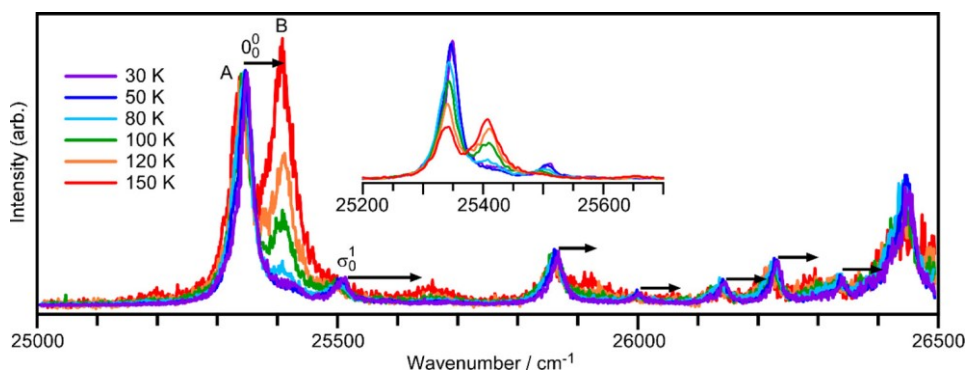


Figure 15. Electronic photodissociation spectra of protonated phenol with five water molecules attached, recorded at different temperatures. At 30 K, only one isomer is present. The increase in temperature promotes interconversion to the second isomer with a different hydrogen bonding network and different absorption characteristics, which is most evident on the position of the 0–0 transition. Reprinted from ref. 110 with permission. Copyright American Chemical Society (2017).

This approach has been used to study the optical properties of chlorophyll *a* and *b* as bare ions and of their complexes with acetylcholine and quaternary ammonium salts¹¹¹ and with formate anions.¹¹² The complexation of chlorophylls simulated the amino acid environment of a protein and these gas-phase results were compared with spectra recorded in solution and in a protein environment. Therefore, the analysis of gas-phase spectra helped to interpret and to understand results from experiments in native protein- and solvent-containing environments, which are otherwise very difficult to explain, even when using theoretical methods.

The method of acquiring PD spectra of ions by photodissociating their electrospray-generated complexes with another molecule has recently been expanded, by employing *N,N,N*-trimethylglycine zwitterion (betaine), and applied to a wide range of common chromophores (Figure 16).¹¹³ Because betaine carries a large dipole moment (calculated value: 11.9 D; for comparison, the dipole moment of water is 1.85 D), it readily forms complexes with ions. Moreover, the electronic transitions of ions, which feature a large degree of charge-transfer character, are significantly affected (shifted) upon complexation of the ion with betaine. Therefore, the comparison

between PD spectra of isolated and betaine-complexed ions enables us to directly characterize electronic transitions.

As shown in Figure 16, the largest blue-shifts in PD spectra of betaine complexes were reported for luciferin and *m*-nitrophenolate anions (last two panels). Hence, the results indicate the high charge-transfer character of electronic transitions of these two chromophores. Conversely, betaine has a rather small or negligible impact on other ions, as demonstrated by small absorption shifts, which suggest that the experimentally examined electronic transitions have little or no charge-transfer character. More recently, the same method of one-photon photodissociation of complexes with betaine has been advantageously used to study the Kongo red ion, which is otherwise difficult to photodissociate.¹¹⁴

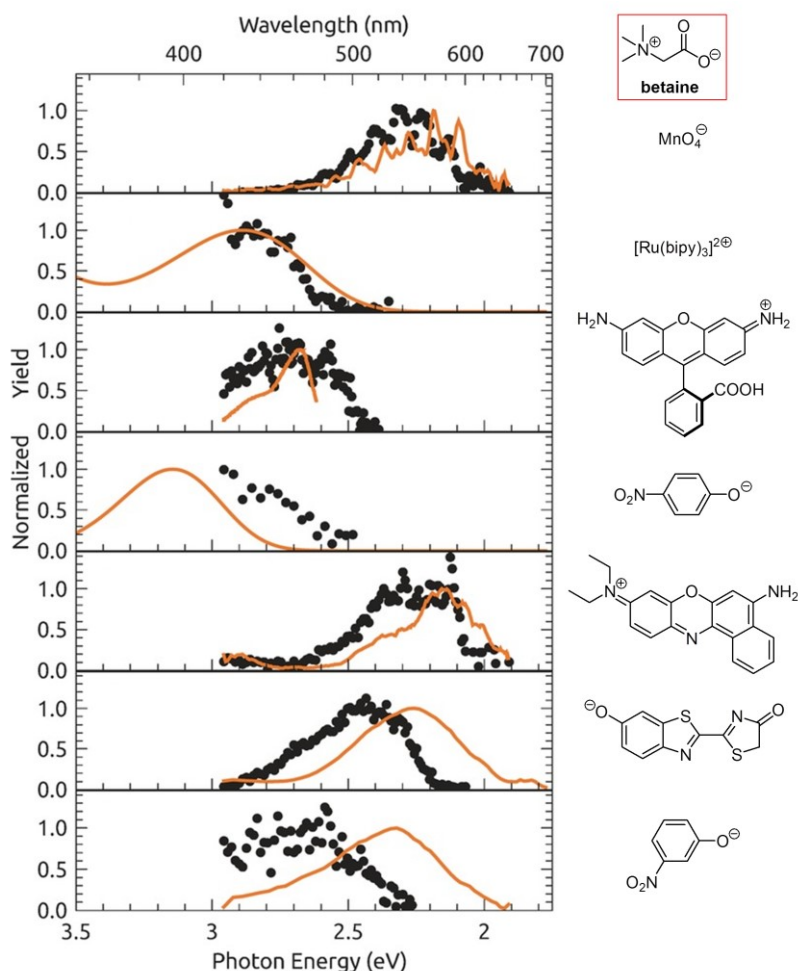


Figure 16. Photodissociation spectra (black data points) of complexes between the betaine zwitterion and various ions of common chromophores. The orange curves correspond to photodissociation spectra of isolated ions without betaine. Adapted and reprinted from ref. 113 with permission. Copyright Wiley-VCH (2017).

Electronic photodissociation spectra contain crucial information, particularly spectra with sharp vibronic structures. Vibrationally resolved PD spectra generally provide a large amount of spectroscopic data otherwise difficult to access. The interpretation of vibronic spectra is based on the well-established Franck-Condon (FC) principle¹¹⁵ and analysis of electronic and vibrational motion.

The first¹¹⁶ and often very intense absorption band is referred to as the 0–0 transition and corresponds to the excitation from the lowest vibrational state of the electronic ground state to the lowest vibrational state of the first excited electronic state (Figure 8, right). The bands at higher excitation energies are spaced from the 0–0 band by energy differences which correspond to vibrational frequencies of the molecule in its excited state (spacing). Hence, the vibrationally resolved spectrum contains the vibrational spectrum of a molecule in the first (or higher) excited state.

The intensity of bands in Franck-Condon progression, which determines the overall shape of a spectrum, is a measure of the nuclear displacement between the electronic ground and excited states and their corresponding vibrational levels (characterized by Huang-Rhys factor, S). For instance, a spectrum with an intense 0–0 transition suggests a small or negligible geometry distortion upon excitation to the excited state (small S).

Although vibrationally resolved PD spectra contain complete information on the structure of excited states, the interpretation of such spectra is only possible with the help of theoretical calculations. Based on them, the structure of ions, in both their ground and excited states, can be determined, even when the ion adopts several isomeric structures.

Figure 17 shows an example of a PD spectrum, specifically of a protonated lumichrome derivative, measured at 25 K, interpreted using theoretical calculations.¹¹⁷ The spectrum features a nice, sharp vibronic structure of the $S_1 \leftarrow S_0$ transition, and the 0–0 band is located at 19962 cm^{-1} . Based on DFT calculations, several isomers with a proton at different heteroatoms were identified; however, only one isomer and its theoretical FC simulation are in line with the experimental results. Small differences between predicted and experimental vibronic bands mainly stem from inaccuracies in harmonic DFT calculations or from experimental deviations from the Franck-Condon principle. Nevertheless, many bands can be directly assigned to specific vibrations of the excited ion.

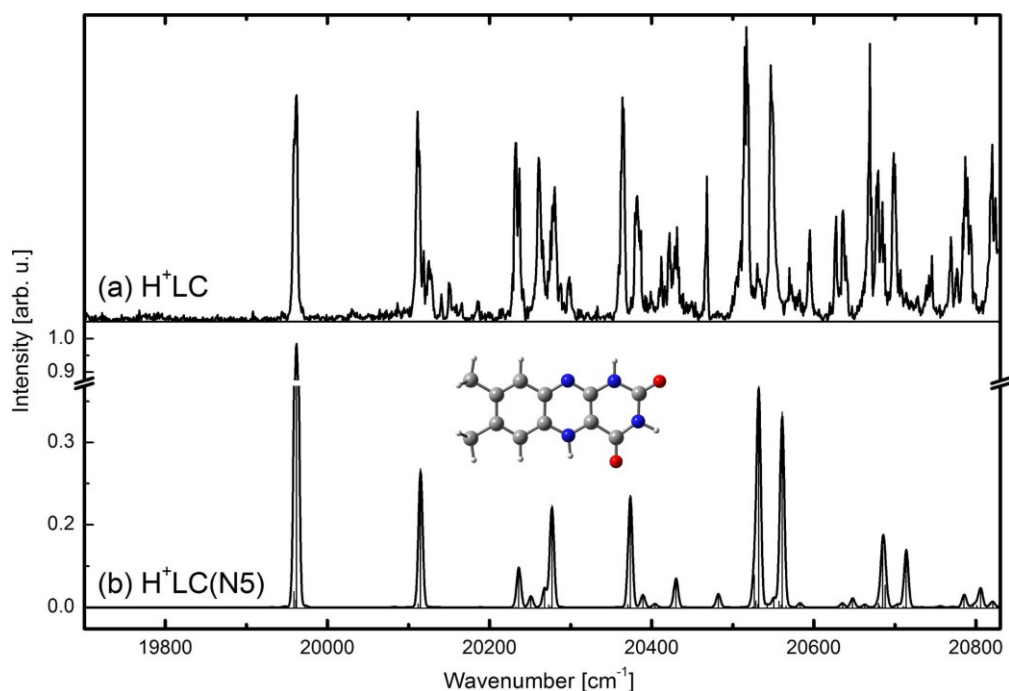


Figure 17. Experimental photodissociation spectrum of protonated lumichrome derivative (a), recorded at 25 K, featuring the 0–0 band at 19962 cm⁻¹, in comparison with the Franck-Condon simulation calculated (b, shifted by 809 cm⁻¹ to match the experimental 0–0 transition frequency). Reprinted from ref. 117 with permission. Copyright Royal Society of Chemistry (2018).

Furthermore, UV/vis photodissociation spectra complemented with theoretical calculations make it possible to assign specific electronic transitions and to uncover detailed electronic structures of studied ions, as in our recent studies on copper-oxo⁷⁵ or iron(III)-oxo complexes.¹¹⁸ Iron(III)-oxo complexes can adopt 3 possible electronic configurations: doublet, quartet and sextet, all of which show different theoretical time-dependent density functional theory (TD-DFT) spectra. Based on experimental helium-tagging photodissociation spectra and on their comparison with TD-DFT spectra, we assigned spin ground states of five iron(III)-oxo compounds (Figure 18). Moreover, our TD-DFT calculations allowed us to assign electronic transitions to excitation between molecular orbitals, specifically to the metal-to-ligand charge transfer (MLCT) from doubly occupied d_{xy} iron-based orbitals to π^* orbitals of pyridine rings.

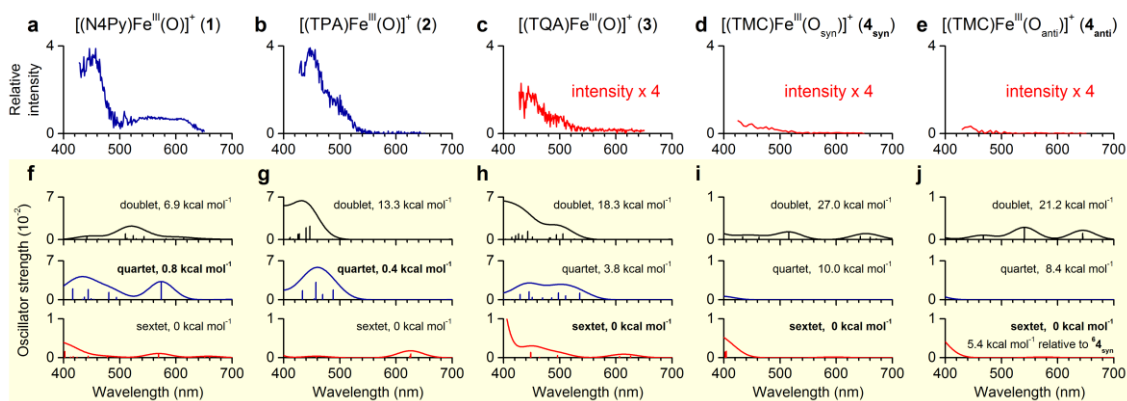


Figure 18. Electronic photodissociation spectra of iron(III)-oxo compounds measured using the helium-tagging method at 3 K (a-e). Panel f-j show theoretically predicted spectra and relative energies of investigated compounds with doublet, quartet and sextet ground spin states. The assigned spin state is highlighted in bold in each case. Reprinted from ref. 118 with permission. Copyright American Chemical Society (2018).

Undoubtedly, photodissociation studies have the potential for significantly advancing our understanding of optical and photochemical properties of molecules and for becoming a benchmark towards improving computational methods on excited state modeling. The critical advantage of gas-phase experiments is the lack of solvent interactions, which represent a substantial barrier to accurate theoretical description. Eventually, improved computational methods and their predictions will help us to design new chromophores with desired photophysical properties. Unfortunately, even TD-DFT, which is a broadly applied computational method for describing excited states, often fails to provide accurate results. For instance, the failure of TD-DFT predictions has been reported in commonly used xanthene dyes, which were described as “a pathological category of compounds for TD-DFT”¹¹⁹ mainly for their systematically overestimated transition energies (see below).¹²⁰

TD-DFT is not the only computational method available for describing excited states nonetheless. Single-reference coupled clusters (CC) or multi-reference complete active space (CAS) and complete active space perturbation theory (CASPT2) methods provide a more advanced and accurate description of electronic structures. Unfortunately, their high computational cost, which limits calculations of larger molecules, have so far restricted their broader use. Recently, a series of xanthene derivatives, including rhodamines, have been examined by photodissociation spectroscopy and their excitation energies were calculated using TD-DFT and CC

methods.¹¹⁹ Figure 19 shows that TD-DFT systematically overestimates transition energies, whereas the CC method provides a more accurate prediction of experimental transition energies.

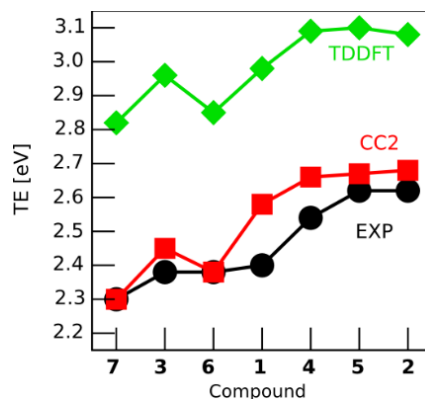


Figure 19. Trends in experimental (black) and theoretical (TD-DFT in green, CC in red) $S_1 \leftarrow S_0$ transition energies of several xanthene derivatives. Reprinted from ref. 119 with permission. Copyright Wiley-VCH (2016).

Despite all apparent advantages, photodissociation spectroscopy is not without drawbacks. The most mentioned and critiqued aspect is the relevance of gas-phase data to experiments and chemistry in solution, wherein solute molecules are surrounded by and interact with solvent and other molecules.

Undoubtedly, transfer to and isolation in the gas phase may in principle alter the molecular structure. Ion spectroscopy experiments then probe species different from those present in and transferred from solution. This is highly relevant to studies on proteins and other large biomolecules.¹²¹⁻¹²⁵ However, many efforts have been made to tackle this issue by bridging the gap between gas-phase and solution experiments, for instance, by studying solvated ions, mostly biomolecules, such as gramicidin S (*vide supra*). Such studies may provide missing links between the gas and condensed phase.

Gas-phase studies almost always depend on theoretical calculations, which enable their analysis; therefore, correctly choosing the theoretical method is crucial for successfully interpreting experimental data. Despite the lack of solvent effects, many theoretical methods fail to correctly predict both electronic absorption (*vide supra*) and vibrational gas-phase data, as shown in our screening of DFT functionals for predicting IR spectra of iron complexes.¹²⁶ Thus, theoretical methods must to be carefully chosen and ideally benchmarked.

Regardless of its limitations and drawbacks, ion spectroscopy is a powerful analytical tool that provides data potentially inaccessible either in solution or when using other methods (*e.g.*, structures of fleeting reactive intermediates), and offers a different perspective of complex chemical processes in solution. Furthermore, as shown by the assignment of diffuse interstellar bands of the C_{60}^+ ion,⁸⁷ ion spectroscopy has been and will always be an irreplaceable method for accurately interpreting astrophysical spectroscopic data.

4 EXPERIMENTAL SECTION

4.1 MATERIALS

Rhodamine 110 chloride and rhodamine 123 chloride were purchased from Sigma Aldrich and used without further purification.

Iron(III) azide complex $[(\text{MePy}_2\text{TACN})\text{Fe}(\text{N}_3)](\text{PF}_6)_2$ (MePy_2TACN = *N*-methyl-*N',N''*-bis-(2-picolyl)-1,4,7-triazacyclononane) was synthesized by Gerard Sabenya in the laboratory of Prof. Miquel Costas, University of Girona, Spain.¹²⁷ I synthesized other studied iron(III) azide complexes, namely $[(\text{cyclam})\text{Fe}(\text{N}_3)_2]^+$ (cyclam = 1,4,8,11-tetraazacyclo-tetradecane),¹²⁸ $[(\text{cyclam-ac})\text{Fe}(\text{N}_3)]^+$ (cyclam-ac = 1,4,8,11-tetraazacyclotetradecane-1-acetate),¹²⁹ and $[(\text{Me}_3\text{cyclam-ac})\text{Fe}(\text{N}_3)]^+$ ($\text{Me}_3\text{cyclam-ac}$ = 4,8,11-trimethyl-1,4,8,11-tetraazacyclotetradecane-1-acetate)¹³⁰ according to known literature procedures. 1,4,8,11-Tetraazacyclotetradecane, 2-iodoacetic acid, lithium hydroxide, formaldehyde, formic acid, sodium azide, iron(III) chloride, sodium hexafluorophosphate and betaine were purchased from Sigma Aldrich and used without further purification.

Hemithioindigo switch (2-[4-(trimethylammonium)benzylidene]-1-benzothiophen-3(2*H*)-one iodide) was synthesized by reacting 2-[4-(dimethylamino)-benzylidene]-1-benzothiophen-3(2*H*)-one with methyl iodide. The synthesis was done by Sandra Wiedbraud in the laboratory of Dr. Henry Dube, Ludwig-Maximilian University in München, Germany.

Solvents used for dissolving samples for electrospray ionization (ESI), specifically acetonitrile and methanol, were purchased from Thermo-Fisher in HPLC quality and used without further purification.

4.2 ION GENERATION

4.2.1 RHODAMINE IONS

Rhodamine ions were generated by electrospray ionization from their solutions in 10 μM methanol. Typical ESI conditions: 6 kV capillary voltage, 100 V tube lens voltage, 200 °C capillary temperature, 30 psi nitrogen sheath gas pressure, 0.2 ml h⁻¹ flow rate, 100- μm internal diameter fused-silica capillary.

4.2.2 IRON(III) AZIDE IONS

Iron(III) azide ions were transferred to the gas phase by ESI of their 50 μM solution in acetonitrile. Typical ESI conditions: 6 kV capillary voltage, 70 V tube lens voltage, 120 $^{\circ}\text{C}$ capillary temperature, 40 psi nitrogen sheath gas pressure, 0.2 ml h^{-1} flow rate, 100- μm internal diameter fused-silica capillary. The high voltage of the ESI source was directly connected to the syringe containing the sample solution through a thin stainless-steel wire. This provided a more intense and stable signal in the mass spectrum.

4.2.3 HEMITHIOINDIGO IONS

Hemithioindigo ions were obtained by ESI of their ~ 10 μM methanolic solutions. A syringe containing an HTI solution (containing both isomers) was irradiated with commercial 525-nm LED diodes for selective transfer of *Z*-HTI to the gas phase. Similarly, commercial 400-nm LED diodes were used to transfer *E*-HTI to the gas phase. Typical ESI conditions: 6 kV capillary voltage, 80 V tube lens voltage, 200 $^{\circ}\text{C}$ capillary temperature, 30 psi nitrogen sheath gas pressure, 0.2 ml h^{-1} flow rate, 100- μm internal diameter fused-silica capillary. The high voltage of the ESI source was directly connected to the syringe containing the sample solution through a thin stainless-steel wire. This provided a more intense and stable signal in the mass spectrum.

4.3 ION SPECTROSCOPY INSTRUMENTATION

All ion spectroscopy experiments described in this Thesis were performed using the Ion Spectroscopy of Reaction Intermediates (ISORI) instrument.^{85,131-133} The ISORI instrument was constructed in our laboratory in Prague by Juraj Jašík and Dieter Gerlich by combining parts from a commercial TSQ 7000 instrument¹³⁴ (Thermo Finnigan) with a custom-built low-temperature ion trap.¹³⁵ The general procedure for spectroscopy experiments using the ISORI instrument can be divided into several phases: 1) ion generation and trapping, 2) generation of vis and infrared irradiation, 3) ion irradiation, photodissociation and detection, and 4) spectra construction and data processing.

Ion generation and trapping

Ions are generated in the original ion source of the TSQ 7000 instrument, which can be equipped with electrospray ionization (ESI), atmospheric pressure chemical ionization or electron ionization sources. The functions of the ion source are controlled by the TSQ 7000 software, and all other functions and settings are controlled by a custom software. After transferring the ions to the gas phase, the ions are mass-selected by the first quadrupole ($4P_1$) and guided by the quadrupole bender (QPB) and by the octopole (8P) to the cryocooled wire quadrupole trap (w4PT) (Figure 20a).¹³⁶ The ion trap is constructed from 24 copper wires (1 mm in diameter, Figure 20b) arranged so that each 6 wires approximate one pole of a quadrupole. The trap also features entrance and exit electrodes, which control ion injection, storage and ejection. The trap is mounted onto a copper box attached to a cold head (Sumitomo) and reaches a minimum temperature of 2.3 K with no gas load inside. Helium gas injection with a custom-made Piezo valve raises the temperature by up to 2 K, most likely due to heat transport between the cold head and the thermal shield. The temperature of the trap is monitored with a silicon diode (TS, Figure 20b) mounted on a copper box, which surrounds the trap. High vacuum, which is necessary for maintaining good ion trapping conditions, is generated by six turbo molecular pumps, which differentially pump ultra-high vacuum chambers of the ISORI instrument. Operation of the ISORI instrument is controlled by custom software, whereas voltages on QPB and between neighboring parts of the instrument ($4P_1$ /QPB, QPB/8P, 8P/w4PT, w4PT/ $4P_2$) are controlled manually with knobs.

Experiments at temperatures higher than 3–4 K are performed using either ion trap heating up to ~60 K by flowing current through a resistor, which is attached to the copper box, and simultaneously by maintaining the cold head operational, or by switching off the cold head upon reaching the wanted temperature during the cool-down or heat-up phases. The trap heats up rather quickly in the 3–50 K range; further heating, eventually to room temperature (300 K), takes several hours (typically overnight).

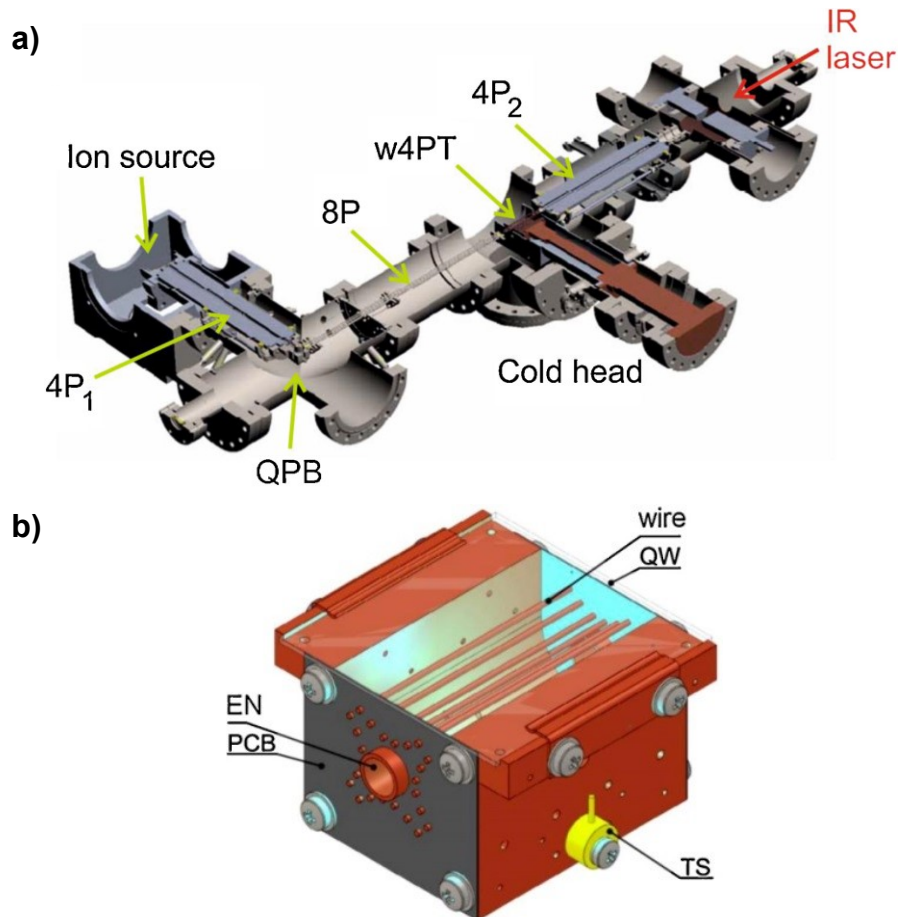


Figure 20. (a) Section of the ISORI instrument showing all main parts: 4P₁ = first mass-selecting quadrupole, QPB = quadrupole bender, 8P = octopole, w4PT = wire quadrupole trap, 4P₂ = second mass-selecting quadrupole. (b) Visualization of the wire quadrupole ion trap containing 24 copper wires. EN = entrance electrode, QW = quartz window, PCB = printed circuit board, TS = temperature sensor (silicon diode). Reprinted from ref. 131 with permission. Copyright Elsevier (2013).

All ISORI experiments, for instance, spectra measurements, consist of repeating cycles; one cycle typically lasts 1 second. Each cycle provides a single value of all monitored parameters (pressure, temperature, number of ions, and a data point in a spectrum, among other variables). Thus, the cycle is repeated to obtain a set of desired data points, *e.g.*, an electronic or infrared spectrum.

During the first part of the 1-s cycle, mass-selected ions exiting 4P₁ are pulsed by QPB (typical duration 20–200 ms), pass through 8P and enter the ion trap. Simultaneously, the helium buffer gas is injected into the ion trap through a short Teflon tube, either in several short intense pulses (0.24 ms long) or in one long pulse (typical duration 50–200 ms). The maximum helium number density reaches the order

of 10^{15} cm^{-3} . The ions that entered the trap collide with dense helium gas, and their kinetic energy and internal degrees of freedom are collisionally cooled (Chapter 3.1). Moreover, if the temperature is sufficiently low, the relaxed ions form weakly bound complexes with helium (helium-tagging, Chapter 3.3). Relaxed ions also form complexes with neutral gaseous impurities, N_2 and H_2O (both below ppm levels), which come either from the helium gas itself or from the ion source (nitrogen is used as the sheath gas in ESI). When complexes with other tagging gases are desired, such as those with argon or neon, a mixture of the desired gas and helium in $\sim 1:10$ ratio is used as the buffer gas.

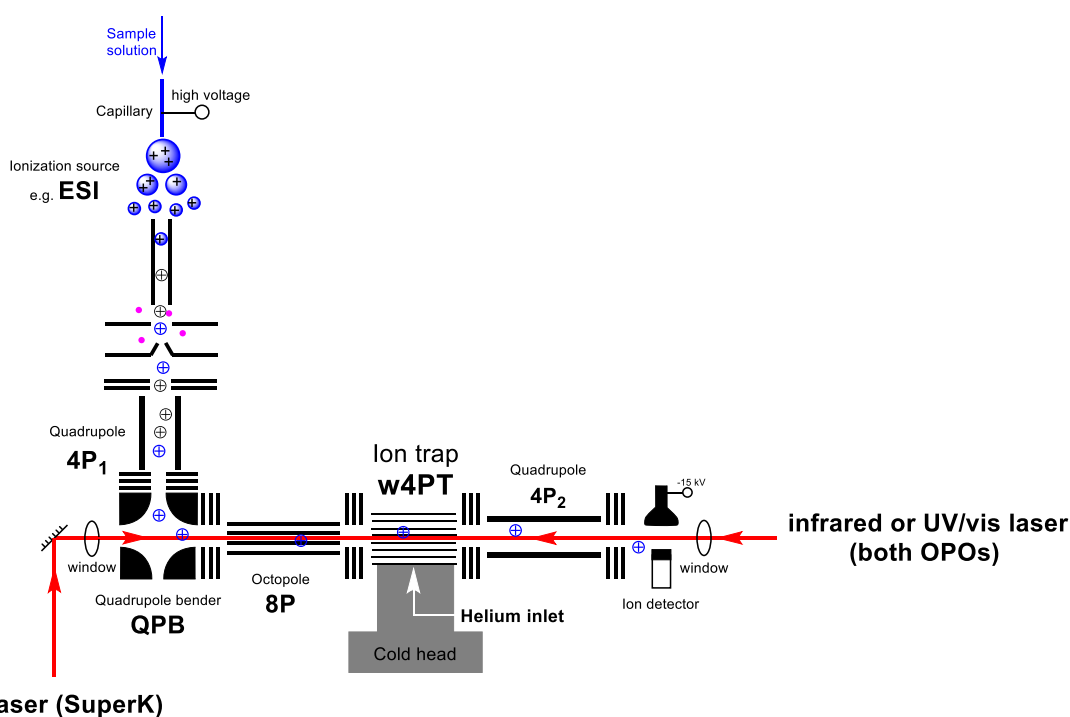


Figure 21. Scheme of the ISORI instrument.

After trapping the ions, eventually complexed with a tagging atom/molecule, the ion cloud interacts with the laser irradiation that is generated as follows:

Generation of vis irradiation

Tunable visible radiation is generated by a supercontinuum laser NKT Photonics SuperK Extreme (78 MHz seed laser repetition rate) equipped with an acousto-optic tunable filter (AOTF) SuperK Select (400–650 nm range, full-width at half-maximum (FWHM) continuously increases from 1.8 nm at 400 nm to 8.5 nm at 650 nm).

The accuracy is ± 0.2 nm of the nominal value over the whole wavelength range, according to the manufacturer. Visible irradiation is focused on the ion trap by lenses and enters the instrument from the QPB side (Figure 21). The diameter of the focal spot is approximately 0.5 mm. The power of the visible laser is routinely measured right before the entrance window of the ISORI instrument (after focusing lenses) using a power meter Thorlabs PM100A with a detector Thorlabs S120C. Typical power output is shown in Figure 22. In iron(III) azide photodissociation spectra (Chapter 5.2), the power output was regulated to approximately 0.8 mW (Figure 22, black trace).

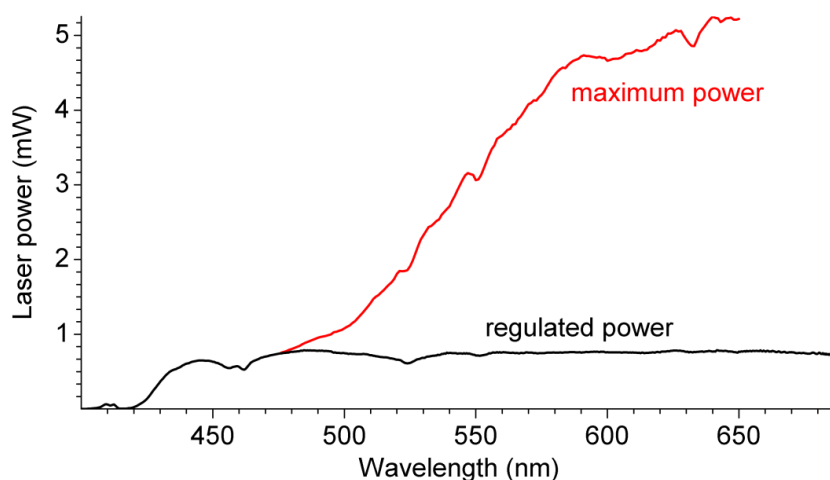


Figure 22. Power output of the visible laser. The red line corresponds to the full power output, which was used in all experiments unless stated otherwise.

High-resolution measurements in the vis range are performed using a Sunlite EX OPO tunable laser system (Continuum), which is pumped with a seeded PL 9010 laser (line width <0.1 cm^{-1} , 10 ns pulse length). The wavelength of the Sunlite EX OPO is calibrated using a WS6-600 wavelength meter (HighFinesse GmbH).

Generation of infrared irradiation

The tunable infrared radiation used for infrared photodissociation spectroscopy is generated by a pulsed OPO/OPA system (LaserVision, tuning range $600\text{--}4700$ cm^{-1} , FWHM ~ 1.5 cm^{-1} , 10 ns pulse length), which is pumped with a seeded Nd:YAG laser Surelite EX (Continuum, 10 Hz repetition rate). The photon beam is guided and focused into the ion trap by lenses and enters the ISORI instrument through a window on the detector side (Figure 21). The energy of the photon beam is controlled by attenuation of the pump energy delivered to the OPA stage and measured by a laser energy meter

Coherent Fieldmax II with J-25MB-LE sensor. Precise frequency calibration of the Nd:YAG pump and OPA stage is performed using a WS6-600 wavelength meter (HighFinesse GmbH).

Ion irradiation, photodissociation and detection

The ions/He complexes in the ion trap are irradiated for a specific period, typically hundreds of milliseconds. If resonant absorption occurs, excited ions/He complexes dissociate a molecular fragment, in the case of ions, and helium (or other tag), in the case of He complexes. Next, the number of ions/He complexes that dissociated is recorded by extracting the ion trap contents (exit electrode potential is lowered) and by their subsequent mass analysis in the second quadrupole ($4P_2$), followed by detection by a Daly-type detector (specifically, the ions are counted). This way, the number of ions/He complexes that dissociated at specific photon energy is obtained (N_i). Furthermore, the same cycle is repeated with the laser beam blocked by a mechanical shutter outside of the instrument; this provides the number of ions/He complexes that were not subjected to laser irradiation (N_{i0} , essentially serving as a reference).

Figure 23 depicts the complete timing of a typical photodissociation experiment. One cycle lasts for 1 s; from 0 to 50 ms, the ions are injected into the ion trap (QPB is pulsed) and, simultaneously, the helium buffer gas is injected (two short pulses at 0 and 35 ms) and collides with ions, thereby enabling their collisional cooling. From 100 to 980 ms, in the N_i cycle, laser irradiation (vis or IR) enters the instrument and irradiates the contents of the ion trap. Finally, at 980 ms, the exit electrode voltage is lowered, which results in the ejection of ions from the trap and in their detection (counting). In the following cycle (N_{i0}), all steps are repeated, except for the laser irradiation, which is blocked by a mechanical shutter in all N_{i0} cycles. Thus, the spectra measurement features many (from hundreds to thousands) alternating N_i and N_{i0} cycles, whereas the laser frequency is continuously being scanned.

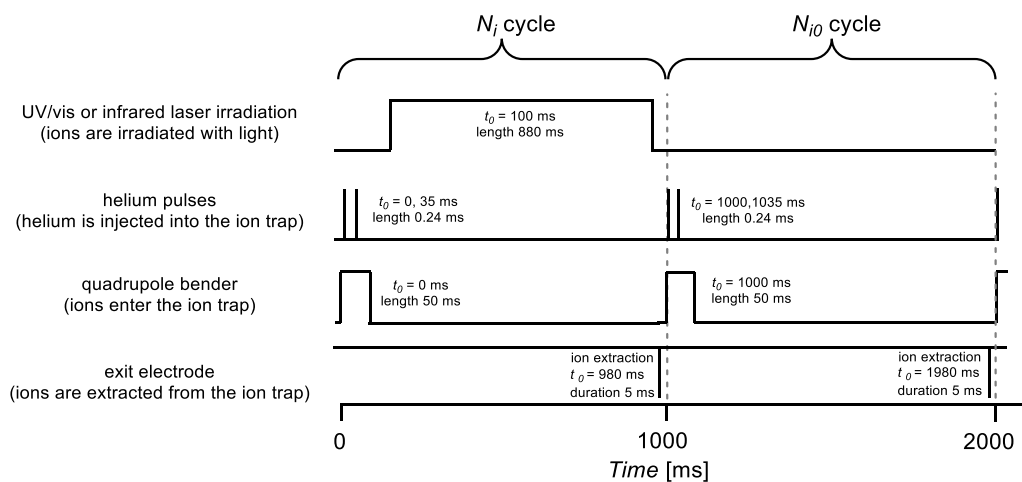


Figure 23. Typical timing of photodissociation experiments

The waiting period between admission of the helium buffer gas and light irradiation typically lasts 50 ms or more and serves for pumping off the helium background pressure, which could, if sufficiently high, cause collisional cooling of ions during the irradiation (please refer to Chapter 3.2 for a discussion on pressure effects on PD spectra and to Figure 6, for instance).

The irradiation period represents the most time-consuming part of all spectroscopy experiments; depending on the strength of the electronic or vibronic transition, irradiation lasting for several hundred milliseconds is required to induce observable photodissociation. When the electronic or vibrational transitions are weak, even longer irradiation times are necessary (e.g., 10 s). Moreover, a cycle at each wavelength is repeated while blocking laser irradiation to obtain a single attenuation value ($1 - N_i/N_{i0}$) in the spectrum. The need for measuring the spectrum point by point represents a significant drawback of this experimental technique because the measurement of a single spectrum, which is composed of multiple scans, takes dozens of minutes to several hours to complete. Furthermore, the stability and intensity of the signal of ions, which is generated in the ionization source, is essential for recording spectra with good signal-to-noise ratios.

Spectra construction and data processing

Tagging electronic and infrared photodissociation spectra are constructed by plotting the attenuation of the signal, expressed as $1 - N_i/N_{i0}$ (N_i and N_{i0} are counts of tagged ions), as a function of photon energy. Such spectra are easily processed by averaging multiple scans and by subsequent reducing noise using the Savitzky-Golay

smoothing¹³⁷ (typically 7 points of window, polynomial order 3) as implemented in the OriginPro 2015 software.

In vis photodissociation of bare ions, N_i and N_{i0} usually denote the number of fragments formed upon dissociation; hence, the N_{i0} value is zero because no fragments are produced without irradiation. The photodissociation spectrum is then constructed by plotting the number of formed fragments (N_i) as a function of photon energy, normalizing intensity to 1. Alternatively, the number of fragments (N_i) can be normalized to the intensity of the parent ion to account for signal fluctuations over time. In some cases (e.g., multiple dissociation channels with distinct absorption profiles, Chapter 5.2), the intensities of several fragments and of the parent ion can be simultaneously and conveniently monitored in the same photodissociation experiment. Furthermore, it should be mentioned that this experiment is only possible when using a supercontinuum SuperK laser, which allows us to measure multiple cycles (multiple fragments, N_i) without the need for changing the wavelength.

Experiments with a high-resolution Sunlite EX OPO laser preclude multiple fragment and parent ion monitoring (multiple N_i values) because wavelength is scanned continuously throughout the experiment; hence, multiple N_i values cannot be simultaneously measured at the exact same wavelength. Instead, only parent ion attenuation is monitored in high-resolution experiments; thus, N_i and N_{i0} correspond to the number of parent ions, which are acquired with and without ion irradiation. The spectra are then typically normalized to the laser power and to the irradiation time, thereby constructing the spectrum by plotting $(1 - N_i/N_{i0})/(E_{laser} \times T_{irr})$ as a function of wavelength.

To avoid ambiguities in spectral processing, y -axis is fully described in all figures with further details in figure captions. Moreover, in the following section, I describe additional experimental details for each Chapter of this Thesis.

4.4 FURTHER EXPERIMENTAL DETAILS

Rhodamine ions (Chapters 5.1.2, 5.1.3 and 5.1.4)

Helium-, argon- and nitrogen-tagging photodissociation spectra are expressed as tagged ion attenuation, $1 - N_i/N_{i0}$, and are not normalized to the laser power. Photodissociation spectra were measured by monitoring the major fragment ion, (m/z 285); PD spectra, in which other fragments were monitored, were measured

analogously. The intensity of PD spectra is normalized to 1. The spectra of rhodamine 123 in Figure 36 are normalized to overall fragmentation efficiency at 460 nm.

Fluorescein and pyronin Y ions (Chapter 5.1.5)

High-resolution helium-tagging photodissociation spectra (Figure 38 and 44) are normalized by dividing tagged ion attenuation by laser power (E_{laser}) and by irradiation time (T_{irr} , typically 800 ms), *i.e.*, $(1 - N_i/N_{i0})/(E_{laser} \times T_{irr})$. In contrast, the low-resolution helium-tagging photodissociation spectrum of pyronin Y (Figure 41) correspond to non-normalized tagged ion attenuation, $1 - N_i/N_{i0}$. Parent ion attenuation was monitored and normalized in temperature-dependent high-resolution photodissociation spectra (Figure 38, blue trace and Figures 40 and 43) and, thus, expressed as $(1 - N_{i,parent}/N_{i,parent})/(E_{laser} \times T_{irr})$.

Iron azides (Chapter 5.2)

In temperature-dependent photodissociation spectra (Figures 48a, 51a, 53a and 55a), wavelength-dependent fragment formation ($N_3\cdot$ (m/z 190.5) and N_2 (m/z 197.5) losses) and parent ions (with (N_i , m/z 211.5) and without (N_{i0} , m/z 211.5) irradiation) were simultaneously monitored in complex **1** (Scheme 2). Analogous fragments and parent ions were monitored in photodissociation experiments with complexes **4**, **5**, and **6** (Scheme 7). Figure 24 shows a typical timing sequence used for measuring temperature-dependent photodissociation spectra with specific ion masses in experiments with complex **1**. The exact conditions at each temperature setting were slightly modified because trapping efficiency strongly depends on temperature, eventually increasing the number of trapped parent ions at low temperatures and saturating the detector. For this reason, the number of trapped parent ions was kept below 4000 by adjusting the number and length of helium pulses and by shortening the length of the QPB pulse.

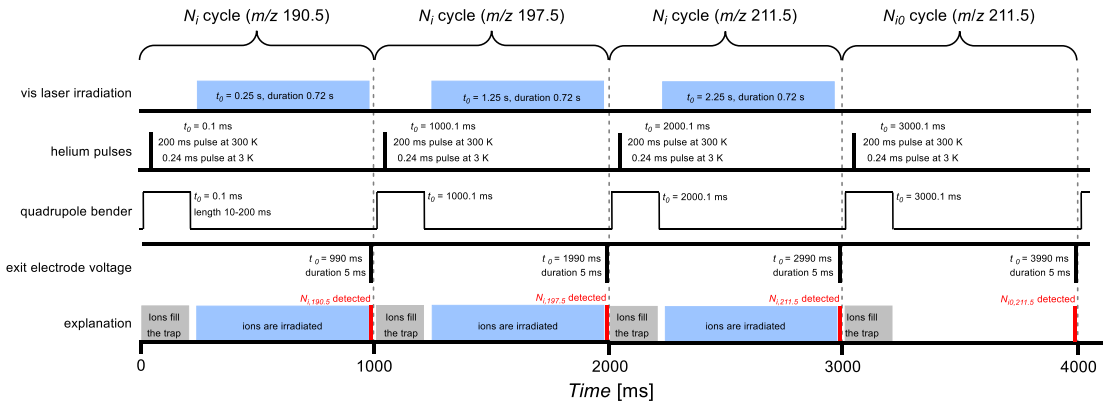


Figure 24. Timing scheme of temperature-dependent photodissociation experiments; the example above shows masses of fragment (m/z 190.5 and 197.5) and parent (m/z 211.5) ions in the photodissociation of complex **1**.

In all experiments, the number of parent ions without irradiation (N_{i0}) was used as a reference value. The ratio between each fragmentation channel (e.g., N_3 vs. N_2 loss) was calculated assuming equal detection efficiency for all fragments. The individual photodissociation yields in PD spectra were determined using a Python script, according to the following equation, in which $N_{i,fragment}$ is the detected number of specific fragment ions, and $N_{i,parent}$ and $N_{i0,parent}$ are the detected numbers of parent ions with and without irradiation, respectively. The equation also includes normalization to the laser power, as shown in Figure 22.

$$Photodissociation\ yield = \frac{N_{i,fragment}}{\sum N_{i,fragment}} \times \frac{-\ln \frac{N_{i,parent}}{N_{i0,parent}}}{E_{laser}}}{\max \left(\frac{-\ln \frac{N_{i,parent}}{N_{i0,parent}}}{E_{laser}} \right)}$$

In temperature-dependent photodissociation experiments measured in the full 3–300 K range (Figures 49, 52, 54 and 56), only the numbers of fragment and parent ions were monitored at few specified wavelengths (*i.e.*, no PD spectra were actually measured); photodissociation yields and PD ratios were determined according to the photodissociation yield equation above. Considering the aforementioned horizontal movements of the ion trap upon cooling/heating and the need for continuous

data collection, the focus of the laser, which cannot be adjusted manually in this experiment, was adjusted automatically using a servomotor that moves the focusing optical element based on a previous calibration (Figure 25). This calibration was performed by manually finding the correct focus (photofragmentation maximum) at each of the 17 temperature values. Lastly, the resulting calibration curve was programmed into the Python script that was used for data acquisition.

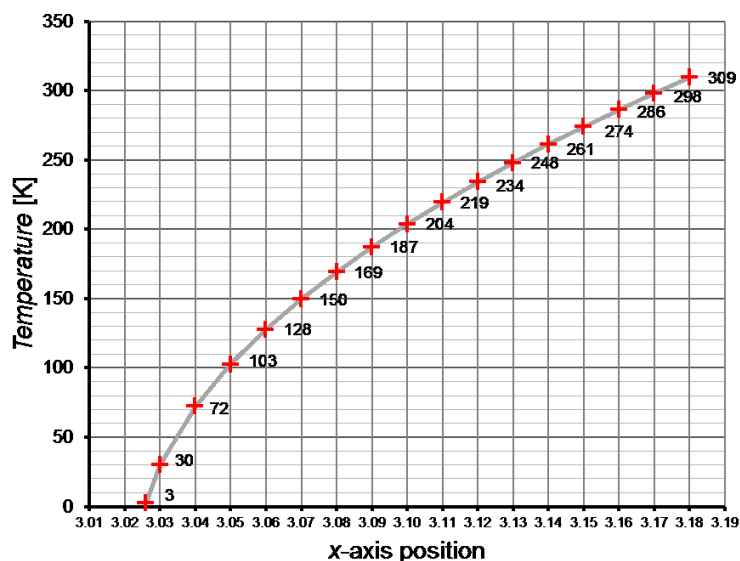


Figure 25. Calibration of the optimal position of the servomotor-driven optical element, which adjusted the horizontal position of the laser beam as a function of the experimental temperature.

The helium-tagging photodissociation spectrum (Figure 48b) corresponds to tagged ion attenuation, $1 - N_i/N_{i0}$, and was normalized to the laser power.

The helium-tagging IRPD spectrum (Figure 50a) displays the tagged ion attenuation, $1 - N_i/N_{i0}$. The infrared multiphoton photodissociation (IRMPD) spectrum (Figure 50b) was measured by monitoring the dissociation of N_2 from the parent iron azide complex **1** at 300 K (N_i and N_{i0} are number of fragments, m/z 197.5, with and without irradiation, respectively) and was constructed by plotting $N_i/N_{i0} - 1$ as a function of wavenumber. In this case, the number of primary ions was not used as a reference due to differences in detection efficiency between the parent and fragment ions.

Hemithioindigo (Chapter 5.3)

Helium-tagging IRPD and helium-tagging photodissociation spectra of *Z*-HTI, *E*-HTI and their betaine complexes (Figures 58, 59, 65 and 66) were measured using the standard tagging experimental scheme and timing (Figure 23) and constructed by plotting the attenuation of helium complexes ($1 - N_i/N_{i0}$) as a function of wave-number/wavelength. Photodissociation spectra were acquired by monitoring the number of formed fragments (m/z 285, loss of 15 mass units from the parent HTI ions, m/z 296) and constructed by plotting the number of fragments normalized to 1 as a function of wavelength.

Figure 26 shows the timing scheme used in photoisomerization experiments (Figure 60 and 61). Firstly, HTI ions were first trapped and cooled to 3 K in the ion trap. Subsequently, the ions were irradiated with a 436-nm laser for 570 ms in $Z \rightarrow E$ photoisomerization. All available wavelengths, including longer irradiation times and a 1.1-W 462-nm laser diode (Thorlabs), were tested in $E \rightarrow Z$ photoisomerization experiments. Afterwards, product ions were cooled again with a helium pulse at 800 ms and formed helium complexes, which were probed by infrared laser providing IRPD spectra. It should be noted that these ions were irradiated only with 2 infrared laser pulses, which sufficed to generate an IRPD signal with attenuation comparable to that of the previous IRPD spectra because these 2 pulses were more powerful than the pulses used in the previous IRPD experiments.

In the attempted $E \rightarrow Z$ photoisomerization of *E*-HTI betaine complexes, a similar experimental scheme to the one shown above was used (Figure 27), albeit with a 2-s cycle. Trapped and cooled [*E*-HTI:betaine]⁺ ions were irradiated by 490-nm light for 900 ms, followed by two helium pulses, which led to the formation of helium complexes. Subsequently, the helium complexes were subjected to 9 infrared laser pulses, recording and comparing IRPD spectra with those of [*Z*-HTI:betaine]⁺ ions (Figure 66).

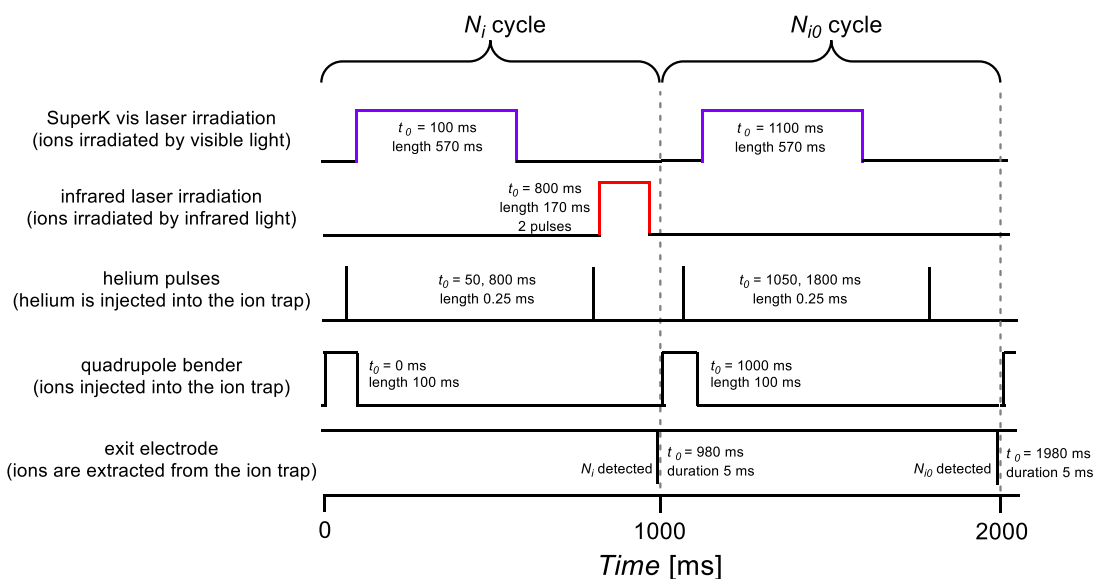


Figure 26. Timing sequence used in $Z \rightarrow E$ and $E \rightarrow Z$ hemithioindigo photoisomerization experiments (Figure 60 and 61).

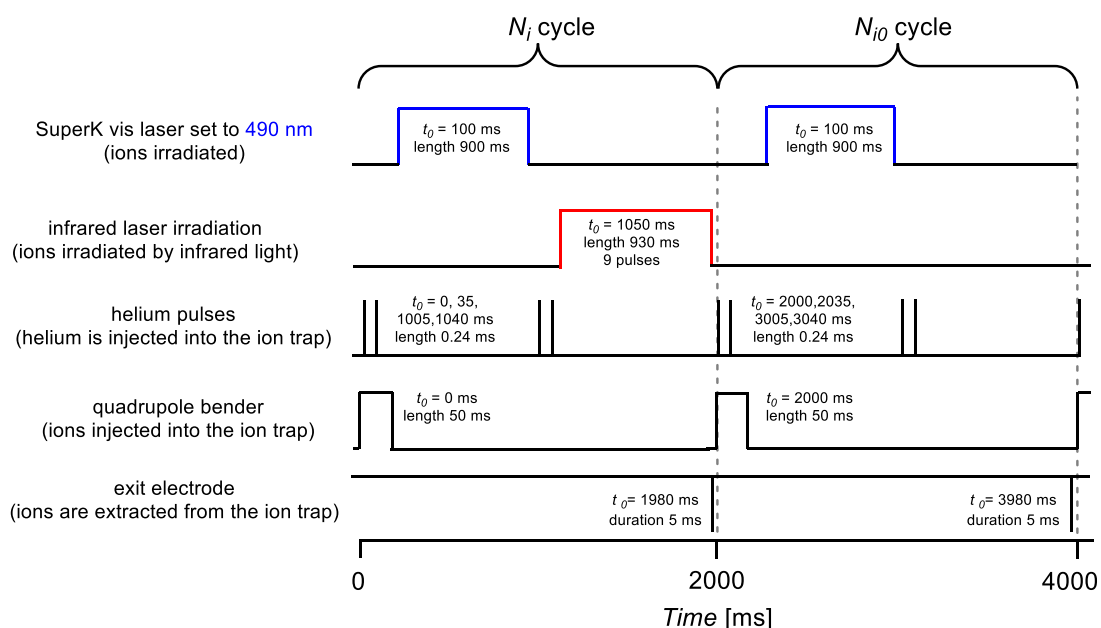


Figure 27. Timing sequence used in $E \rightarrow Z$ photoisomerization experiments of $[E\text{-HTI.betaine}]^+$ ions at 3 K (Figure 66).

4.5 THEORETICAL DETAILS

General remarks

All calculations were performed using the Gaussian 09 software package,¹³⁸ results were visualized in the ChemCraft software,¹³⁹ and experimental and compu-

tational data were processed in the OriginPro 2015 software. Finally, theoretical infrared spectra were scaled by a factor of 0.99, and Gaussian broadening (full width at half maximum 5 cm^{-1}) was applied to theoretical IR spectra using a custom Python script for a better comparison with experimental spectra.

Rhodamines, fluorescein and pyronin Y (Chapter 5.1)

Geometry optimization and frequency calculations of rhodamine 110 and 123 were performed using the density functional theory (DFT) by combining the B3LYP¹⁴⁰⁻¹⁴³ method with the 6-311++G** basis set, Grimme's D3 dispersion correction¹⁴⁴ and Becke-Johnson damping¹⁴⁵ (GD3BJ), as implemented in the Gaussian G09 software package.¹³⁸ The geometry optimization of pyronin Y ions was performed using the M06L¹⁴⁶ method combined with the def2TZVP¹⁴⁷ basis set and Grimme's D3 dispersion correction.¹⁴⁴ The procedure for determining S₁ state geometries is described in detail below. The identities of all optimized structures were examined by Hessian matrix calculations at the same level of theory to ensure that energy minima were reached. Franck-Condon simulations were performed using the same DFT methods as those used for geometry and frequency calculations.

Iron azides (Chapter 5.2)

The geometry optimization and frequency calculations of ions **1**, **4**, **5** and **6** were performed by Erik Andris at the B3LYP-D3/6-311++G** level of theory¹⁴⁰⁻¹⁴⁴ using the Gaussian G09¹³⁸ software. Electronic spectra were predicted at the same level of theory using the time-dependent DFT theory. Complete active space self-consistent field (CASSCF) and complete active space second-order perturbation theory (CASPT2) calculations were performed by Martin Srncic in MOLCAS 8.0 service pack 1 software.¹⁴⁸ The ANO-RCC basis set was used, contracted to [6s5p3d2f1g] for Fe, [4s3p2d] for N, [3s2p] for C and [2s] for H atoms. Second-order Douglas-Kroll-Hess one-electron spinless Hamiltonian was used in all calculations to allow spin-free relativistic effects.^{149,150} For additional details on CASSCF/CASPT2 calculations, please refer to ref. 151.

Hemithioindigo (Chapter 5.3)

Geometry optimizations of S_0 , T_1 and S_1 states and calculations of theoretical infrared spectra were performed using the DFT by combining the M06L¹⁴⁶ method with the def2TZVP¹⁴⁷ basis set and Grimme's D3 dispersion correction¹⁴⁴, as implemented in the Gaussian G09 software.¹³⁸ Calculations of the Hessian matrix were performed for all optimized structures at the same level of theory to ensure that structures correspond to energy minima or transition states. Franck-Condon simulations were performed using the Franck-Condon-Herzberg-Teller method¹⁵² at the same M06L-D3/def2TZVP level theory, as implemented in the Gaussian G09 program.

The following procedure was used to determine S_1 state geometries to perform Franck-Condon calculations: Firstly, S_0 and T_1 states were optimized, inspecting the HOMO and LUMO orbitals of S_0 and the both SOMO orbitals of T_1 states (Figure 28). In the studied HTI compounds, the $S_1 \leftarrow S_0$ electronic transition occurs between orbitals number 78 (HOMO) and 79 (LUMO).

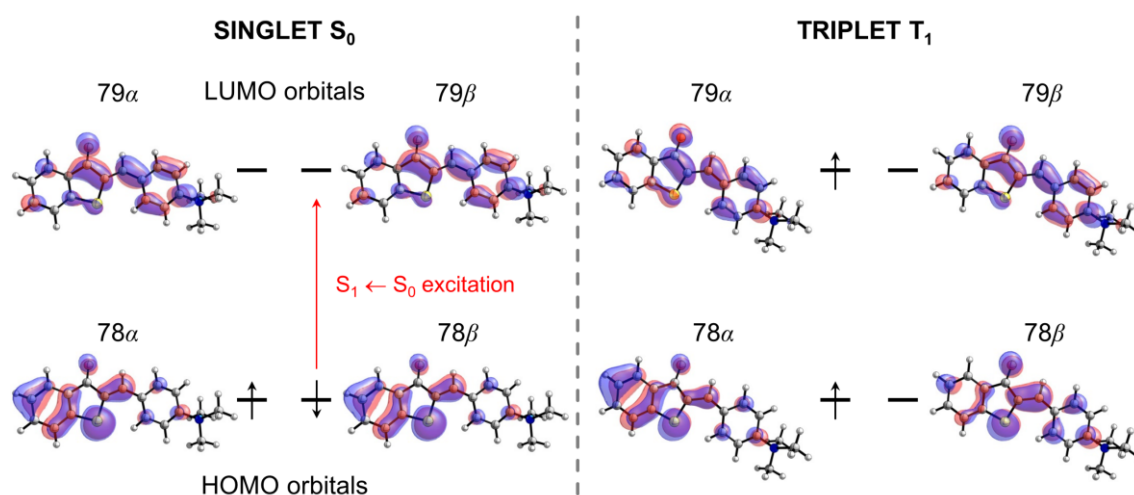


Figure 28. Molecular orbital scheme of S_0 and T_1 states of Z -HTI cation. Orbitals are divided according to their spin into α and β orbitals based on the unrestricted formalism. The red arrow highlights the $S_1 \leftarrow S_0$ excitation involving an electronic transition from 78β to 79β , which was used in Franck-Condon simulations.

The orbital scheme also shows that the desired S_1 state has orbital occupancies similar to the T_1 state; moving the electron in 79α orbital to 79β orbital (spin flips) provides the correct orbital occupancies of the S_1 state. In fact, this is exploited in S_1 state optimization because the T_1 wavefunction is used as an initial guess in S_1 state

optimization. In the calculation, orbitals are swapped (rotated); in this case, 78β and 79β orbitals are exchanged. An example of such Gaussian input is presented below:

```
%oldchk=T1_state_checkpoint.chk           T1 state wavefunction as the initial guess
%chk=name.chk
%nproc=12
%mem=24GB
# method/basis_set geom=check scf=(qc,VShift=500) guess=(read,alter)
opt=calcall freq=SaveNM                   keywords

name

1 1                                         charge and multiplicity

78 79                                       79 $\beta$  and 78 $\beta$  orbitals are swapped
```

The keywords *oldchk*, *guess=read* and *geom=check* specify that the checkpoint file of the T_1 state optimization is used as the initial wavefunction guess. The keyword *guess=alter* swaps (rotates) together with the specification of orbitals at the bottom of the input swaps (rotates) the orbitals, in this case, 78β and 79β . Please note that the correct number line spacing is needed for successfully submitting the calculation. Keywords *scf=(qc,VShift=500)* and *opt=calcall* are recommended and most often also necessary for successful convergence to the desired S_1 state. Finally, the keyword *freq=SaveNM* is necessary for the final Franck-Condon calculation job and must also be included in the input file of the S_0 state calculation.

Finally, the Franck-Condon simulation is a straightforward procedure, which combines the output of ground and excited state calculations. The typical Gaussian 09 input is shown below:

```
%oldchk=S0_checkpoint.chk                 checkpoint file of the initial state (S0)
%nproc=12
%mem=25GB
#P method/basis_set NoSymm freq=(ReadFC,FC,ReadFCHT) temperature=3
geom=allcheck                             keywords

InpDEner=
Spechwhm=
PrtInt=
MaxStatesI=
DoTemp
MaxBands=
MAXC1=
DeltaSP=                                 simulation parameters

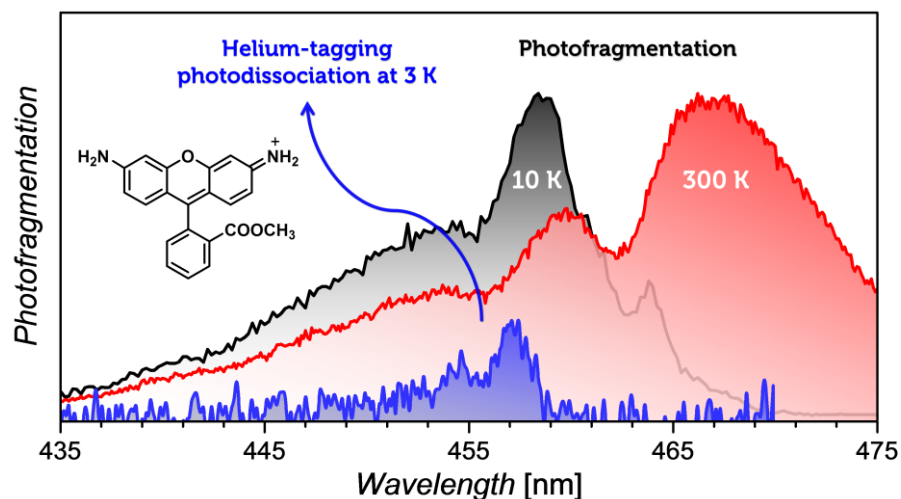
S1_checkpoint.chk                         checkpoint file of the final state (S1)
```

The checkpoint file of S_0 and S_1 calculations must be included with the Franck-Condon simulation input file; the *temperature* keyword specifies the temperature of the simulation. Furthermore, several other parameters of the simulation can be and are typically specified, such as the experimental 0–0 transition energy or spectra linewidth, among others. For further details, including the theory behind the Franck-Condon simulations, parameter default setting, recommendations and trouble-shooting, please refer to a manual for calculating vibrationally-resolved electronic spectra in Gaussian 09.¹⁵³

Finally, I note that I had also tried designated programs for simulating Franck-Condon envelopes, specifically PGOPHER¹⁵⁴ and ezSpectrum,¹⁵⁵ however, I was unable to reach reliable results. Moreover, with the availability of analytical frequency calculations in the TD-DFT method in Gaussian 16 software, the need for performing geometry optimizations of excited state using the scheme described above is highly unlikely. The results should be always carefully evaluated nevertheless, especially regarding the nature of the excited state, which can be biased by the chosen DFT method.

5 RESULTS AND DISCUSSION

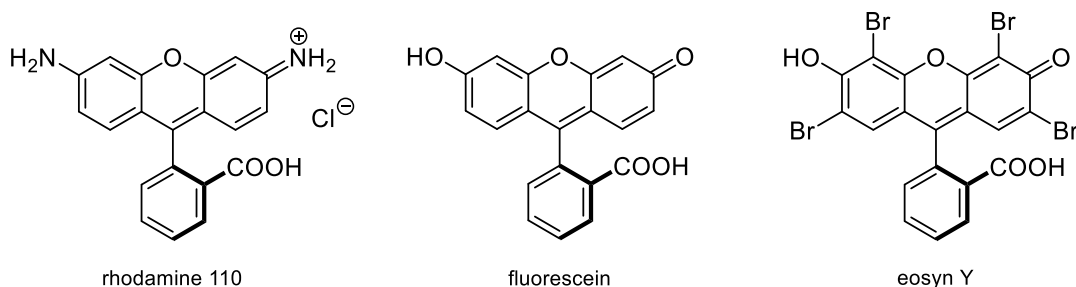
5.1 VISIBLE PHOTODISSOCIATION SPECTRA OF RHODAMINE IONS AND TAGGING AND TEMPERATURE EFFECTS



This chapter is based on results reported in “Jašík, J.; Navrátil, R.; Němec, I.; Roithová, J. *Infrared and Visible Photodissociation Spectra of Rhodamine Ions at 3 K in the Gas Phase. J. Phys. Chem. A* **2015**, *119*, 12648–12655” and in “Navrátil, R.; Jašík, J.; Roithová, J. *Visible photodissociation spectra of gaseous rhodamine ions: Effects of temperature and tagging. J. Mol. Spectrosc.* **2017**, *332*, 52–58” and “Navrátil, R.; Roithová, J. *unpublished results*”.

5.1.1 INTRODUCTION

Rhodamines are fluorescent dyes based on a rigid three-ring xanthene core, similarly to other xanthene-type dyes like fluorescein or eosin derivatives (Scheme 2).¹⁵⁶ The synthesis of xanthene dyes dates back to 1871, when von Bayer first synthesized fluorescein.¹⁵⁷ Thereafter, many other xanthene dyes, especially rhodamine derivatives, have been synthesized with varying substituents mainly on the phenyl ring in position 9 of the xanthene core and on the rhodamine nitrogen atoms. Substitution directly affects the absorption, solubility and stability properties of xanthene dyes.



Scheme 2. Examples of xanthene-type dyes.

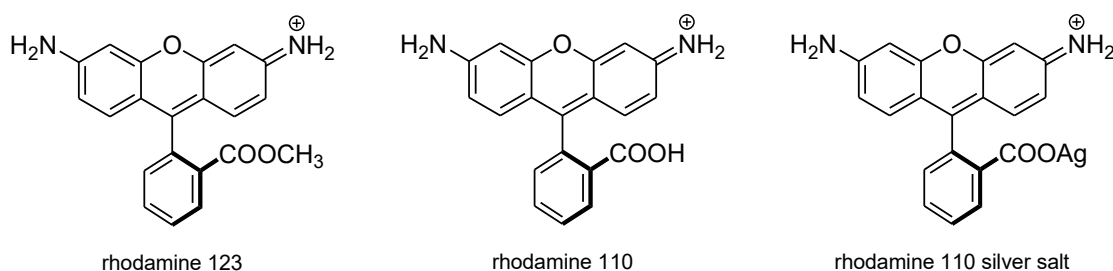
Rhodamine chromophores feature interesting photophysical properties, such as excitation and emission covering the visible range and even extending to the near-infrared range, high molar extinction coefficients (10^4 – 10^5), high fluorescence quantum yields (typically 90% or higher, depending on the dye derivative and on the solvent), low triplet quantum yields and sufficient photostability.^{158,159} Thanks to these properties, rhodamines have been widely applied in physics, chemistry and biology¹⁶⁰ as dyes, dye laser gain media,¹⁶¹ fluorescent tracers in water,¹⁶² fluorescent probes,¹⁶³⁻¹⁶⁶ fluorescent thermometers,¹⁶⁷ cell and tissues stains^{168,169} or molecular probes.¹⁷⁰

In addition to numerous studies in the condensed phase, properties of rhodamine chromophores have also been studied in the gas phase. Some of these studies have already been discussed in Chapter 3.5. Notably, in 2015, the group of Jockusch directly compared experimental photodissociation and fluorescence excitation spectra of rhodamine 110 (Rh 110) using a modified commercial quadrupole ion trap mass spectrometer.¹⁷¹ In solution, absorption and fluorescence excitation spectra of Rh 110 are virtually indistinguishable. In contrast, the gas-phase PD spectrum of Rh 110 is red-shifted by ~ 120 cm^{-1} and features a narrower profile than its gas-phase fluorescence excitation spectrum. Moreover, the authors of the study showed that the photo-

dissociation is on average a three-photon process, whereas fluorescence excitation requires only a single photon.

Gas-phase studies on highly fluorescent ions, such as rhodamines, can be rather challenging experimentally because competing fluorescence deexcitation typically limits the efficiency of multiphoton photodissociation processes (Chapter 3.2). Therefore, single-photon photodissociation methods are more desirable, not only for accessing spectroscopic properties of isolated molecules but also for allowing direct interpretation and benchmarking of computational data. In our initial studies, we aimed to establish helium-tagging photodissociation spectroscopy as an ideal method for recording electronic spectra of highly fluorescent ions. Similarly to the previously established helium-tagging infrared photodissociation (IRPD) method, we assumed that the helium tag would dissociate after single-photon absorption. Moreover, we assumed that helium-tagging photodissociation spectra would be only negligibly affected and biased by the helium-tagging method itself.

We selected three cationic and highly fluorescent rhodamine dyes, specifically rhodamine 123 (Rh 123), rhodamine 110 (Rh 110) and rhodamine 110 silver carboxylate (Rh 110-Ag; Scheme 3), to assess whether the helium-tagging method could be applied for recording their electronic photodissociation spectra in the visible range.



Scheme 3. Investigated cationic rhodamine dyes.

5.1.2 HELIUM-TAGGING PD SPECTRA OF RHODAMINE IONS

Figure 29 shows helium-tagging visible photodissociation spectra of investigated rhodamine ions recorded at 4 Kelvin. All spectra feature prominent 0–0 transitions, which are located at 457.1 ± 1.0 nm in rhodamine 123, 459.2 ± 1.0 nm in rhodamine 110 and 450.6 ± 1.0 nm in rhodamine 110 silver salt. The spectra of all three compounds are vibrationally resolved, thereby containing structural information on ex-

cited states. However, the spectral resolution, which is limited by the linewidth of our laser, in this case, precludes a more detailed analysis. Nonetheless, simulations of the Franck-Condon envelope (Figure 29, blue traces) allowed us to assign the detected electronic transitions between S_0 and S_1 states. Moreover, the high intensities of the 0–0 bands suggest that the $S_1 \leftarrow S_0$ excitation is accompanied only by negligible nuclear distortion.

The 0–0 transition energies increase from acid (rhodamine 110) through methyl ester (rhodamine 123) to carboxylate (rhodamine 110 silver salt). The same trend has already been observed in a previous photodissociation study of rhodamine 575 (acid) and rhodamine 590 (methyl ester).⁵³ The less electron-withdrawing substituents at the perpendicular phenyl ring stabilize the decreased electron density in position 9 of the xanthene ring upon excitation to the S_1 state. The resulting stabilization effect on the S_1 state lowers the $S_1 \leftarrow S_0$ excitation energy, which may explain the trend highlighted above.

Interestingly, the 0–0 transition of rhodamine 110 located at 459.2 nm is blue-shifted by 5.8 nm (276 cm^{-1}) and by 3.3 nm (160 cm^{-1}) in comparison with the PD and fluorescence excitation spectra reported by Jockusch,¹⁷¹ corresponding to energy differences of 3.3 and 1.9 kJ mol^{-1} , respectively. These small, but apparent energy differences can stem from the limited resolution of the previous experiments reported by Jockusch and/or from the fact that the spectra reported by Jockusch were acquired at room temperature, which suggest that studied ions had increased internal energy. Conversely, our spectra were recorded at 3 Kelvin using the helium-tagging technique, which ensures vibrational relaxation. Nevertheless, our data, including excitation energies, could still be biased by the helium-tagging method itself.

Figure 30 summarizes two possible outcomes of helium-tagging on excitation energies between ground and excited singlet states, S_0 and S_1 . If the helium tag were bound in the S_0 and not in the S_1 state (Figure 30b), the corresponding excitation energy would be higher than that of the bare ion (Figure 30a). This would stem from the decrease in the energy of the S_0 state caused by binding to a helium tag. Moreover, the fact that the S_1 state would be dissociative for helium would suggest that helium specifically binds to some functional groups. Furthermore, the excitation energy would directly depend on the tag used, reflecting its binding energy. In the third scenario (Figure 30c), helium would be bound in both S_0 and S_1 states.

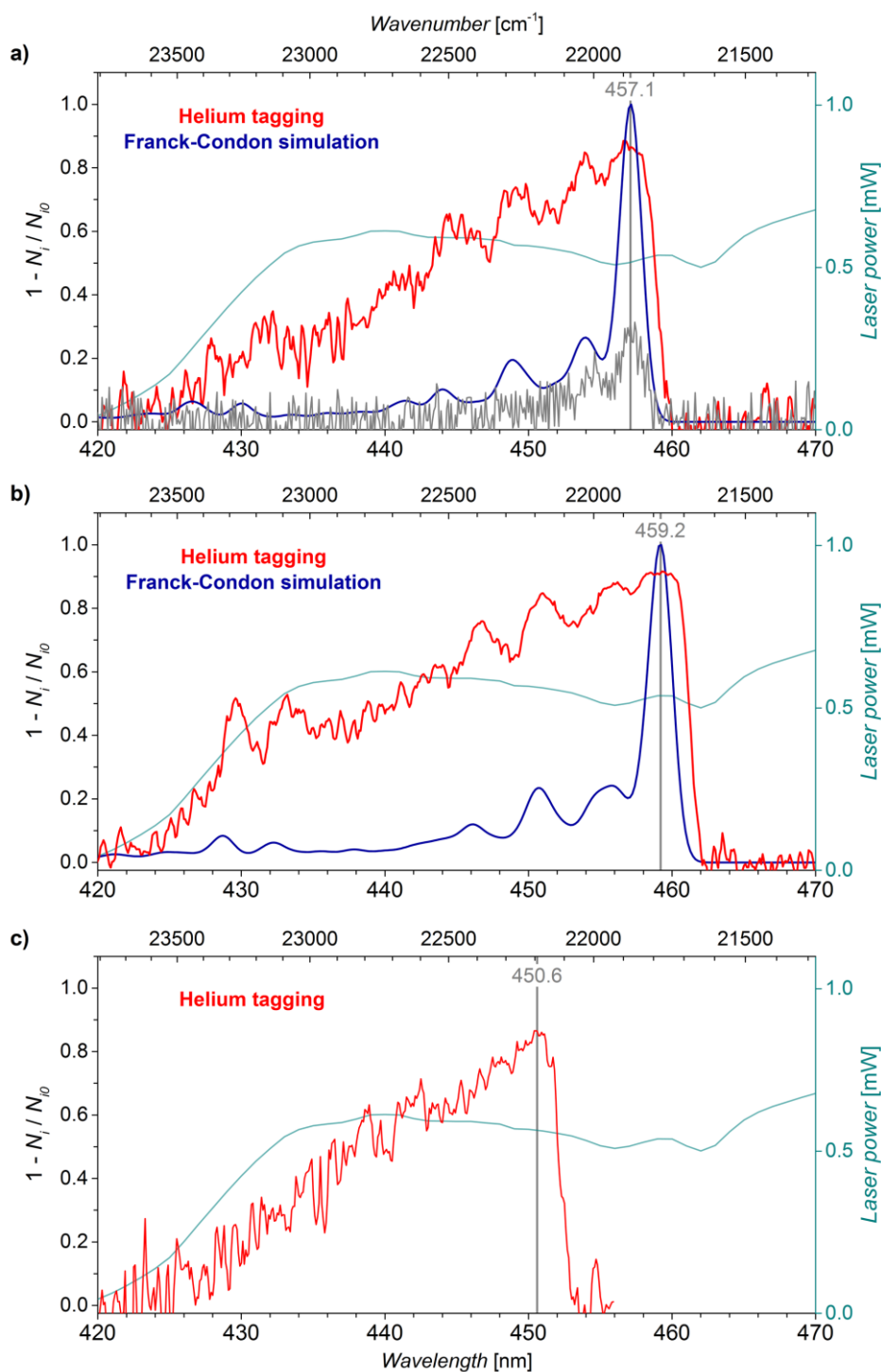


Figure 29. Helium-tagging photodissociation spectra of rhodamine 123 (a), rhodamine 110 (b), and rhodamine 110 silver salt (c). The gray trace in (a) represents the spectrum, which was recorded using a reduced laser power to avoid signal saturation.

If the binding energies were identical in both states, helium-tagging would have no effect on the excitation energy. Similarly, different tags would have the same effects on the excitation energy, despite their different binding energies. Hence, excitation

energies should be independent of the tagging atom used because the binding energies at S_0 and S_1 states are the same.

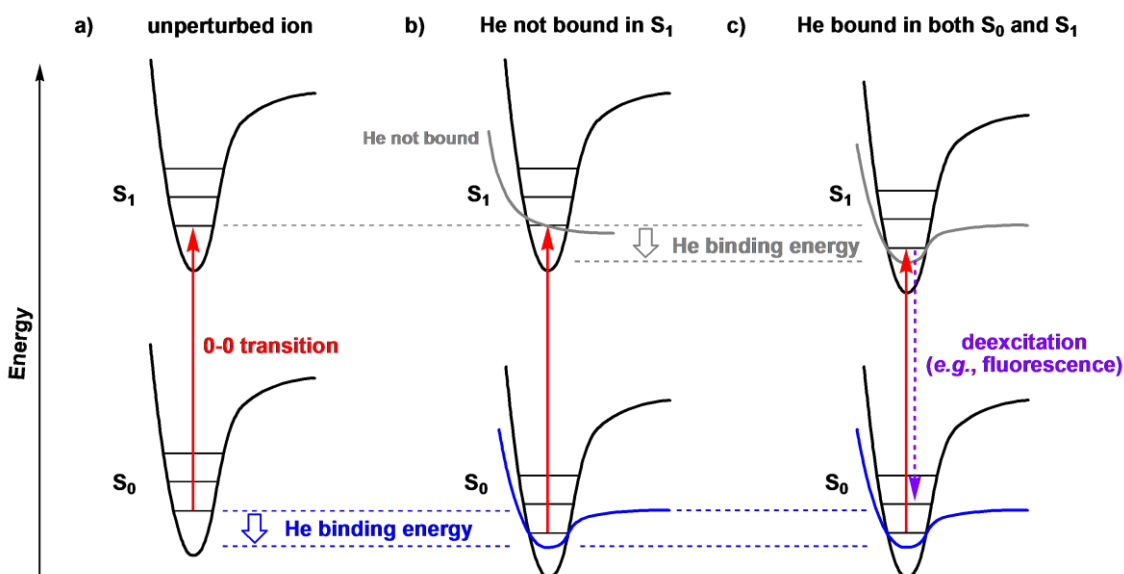


Figure 30. Possible effects of helium-tagging on S_0 and S_1 energies and $S_1 \leftarrow S_0$ excitation energy of an ion. (a) Unperturbed ion. (b) Tagging with helium decreases the S_0 energy level and thus increases the $S_1 \leftarrow S_0$ excitation energy. Helium dissociates right after the excitation because it is not bound in the S_1 state. (c) Tagging with helium decreases the S_0 and S_1 energy levels and thus may not affect the $S_1 \leftarrow S_0$ excitation energy. Helium dissociates after deexcitation (e.g., fluorescence) into the vibrationally hot state of the S_0 state.¹⁷²

5.1.3 TAGGING EFFECT

To study the effects of tagging on electronic PD spectra, I measured tagging photodissociation spectra using two more alternative tags, argon and nitrogen. Both tags bind more strongly than helium, which I also confirmed by DFT calculations at the B3LYP-GD3BJ/6-311++G** level. Table 1 outlines the calculated binding energies of various isomeric helium- and argon-tagged complexes of rhodamine 123 ion. As expected, helium is indeed bound very weakly, with binding energies well within the generally accepted DFT calculation error, which is 1 kcal mol^{-1} . This corroborates my experimental observations in which a small temperature increase (tenths of Kelvin) leads to the immediate decay of helium complexes. Argon, a heavier noble gas, is more strongly bound than helium (by one order of magnitude), which also

explains why argon-tagging does not require temperatures as low as those required for helium-tagging. I was nevertheless unable to localize energy minima of the corresponding nitrogen complexes and thus to determine nitrogen binding energies. However, those energies are expected to be even higher than that of argon.

Table 1. Energies of the bond between rhodamine 123 and the helium/argon-tagging atom calculated at the B3LYP-GD3BJ/6-311++G** level of theory. Optimized geometries of complexes are shown in Figure 31.

	$E_{el.}+E_{ZPE}$ [Hartree]	Binding energy [kJ mol ⁻¹]
Rhodamine 123	-1145.547811	-
Helium	-2.913544	-
Argon	-527.553884	-
Rhodamine 123 . He complex 1	-1148.461427	0.2
Rhodamine 123 . He complex 2	-1148.461412	0.1
Rhodamine 123 . He complex 3	-1148.461422	0.2
Rhodamine 123 . He complex 4	-1148.461416	0.2
Rhodamine 123 . Ar complex 1	-1673.105072	8.9
Rhodamine 123 . Ar complex 2	-1673.104727	8.0
Rhodamine 123 . Ar complex 3	-1673.104675	7.8

Optimized geometries of all helium and argon complexes are shown in Figure 31. The character of helium and argon binding is non-specific in both cases (no particular isomer is energetically preferred). The non-specificity of helium binding to ions has been previously reported, *e.g.*, in the proton-bound complex $[\text{NH}_3\text{-H-OH}_2]^+$ ¹⁷³ or in the fullerene C_{60}^+ ion.⁸⁷

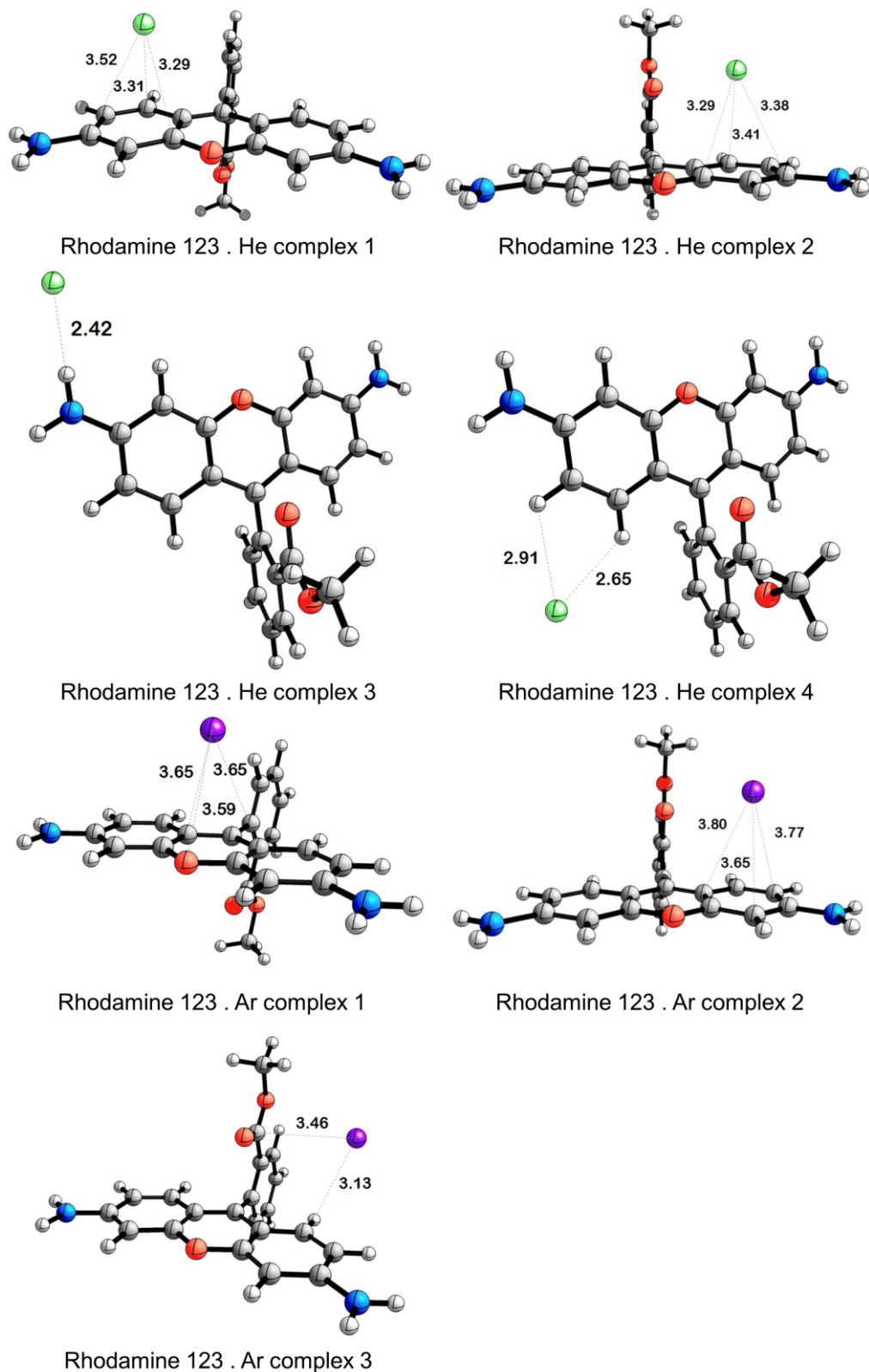


Figure 31. Optimized geometries of complexes between rhodamine 123 and helium or argon calculated at the B3LYP-GD3BJ/6-311++G** level. Distances are reported in Ångströms. Color code: helium – green, argon – violet, oxygen – red, nitrogen – blue, carbon – grey, hydrogen – light grey.

Figure 32 shows the comparison between helium, argon and nitrogen-tagging spectra acquired at 3 K. The 0–0 transitions remain located at unchanged wavelengths in all three cases, specifically at 457.1 nm for He-tagging and at 457.3 nm for Ar- and N₂-tagging. The relative shift of 0.2 nm corresponds to an energy difference of 0.1 kJ mol⁻¹. Such small shifts have been previously reported in a study of C₆₀⁺ (Chapter 3.3).⁷³ However, the differences in theoretical binding energies between helium and argon (and most likely also nitrogen) are significantly larger, *ca.* 8 kJ mol⁻¹ (*cf.* Table 1). The tagging atom has only a minor effect on the excitation energies of rhodamine ions; hence, the tagging atom has to be bound in the S₁ state (situation in Figure 30b). Accordingly, the tagging atom is bound both in S₀ and S₁ states and, upon excitation, the photodissociation occurs from a vibrationally hot ground state reached after fluorescence deexcitation from the S₁ state (depicted in Figure 30c).

A closer inspection of the spectra shown in Figure 32 shows some minor discrepancies between band positions, for example, the position of the 10¹ transition (assigned based on theoretical predictions) is shifted to shorter wavelengths when applying N₂ tagging. In addition, the N₂ tagging spectrum is less resolved, which suggests that heavier tagging atoms, such as nitrogen and argon, slightly distort the molecular structure of Rhodamine ion to some extent. At this point, I could not exclude the possibility that helium binding has a similar effect as well.

Additionally, I measured the argon-tagging spectrum of rhodamine 123 ion at a higher temperature (10 K, Figure 33). The spectrum at 10 K displays only minor changes in vibronic structure in comparison with the spectrum acquired at 4 K. The position of the 0–0 band remains unchanged. Interestingly, when I used a full laser power in the experiment at 4 K, I obtained a spectrum with over-saturated bands with increased linewidth and with absorption bands with lower energy than that of the 0–0 transition, possibly hot bands. I concluded that these bands with maxima around 461 and 465 nm originate from excitations from vibrationally excited states of the S₀ ground electronic state. I observed no such bands in the helium-tagging spectrum, even when I used the full laser power (*cf.* Figure 29a). This further demonstrates that helium more efficiently generates tagged complexes with the lowest possible internal energy than the other tags, especially because argon and nitrogen, due to their higher binding energies, also form tagged complexes with ions, which are not fully vibrationally relaxed.

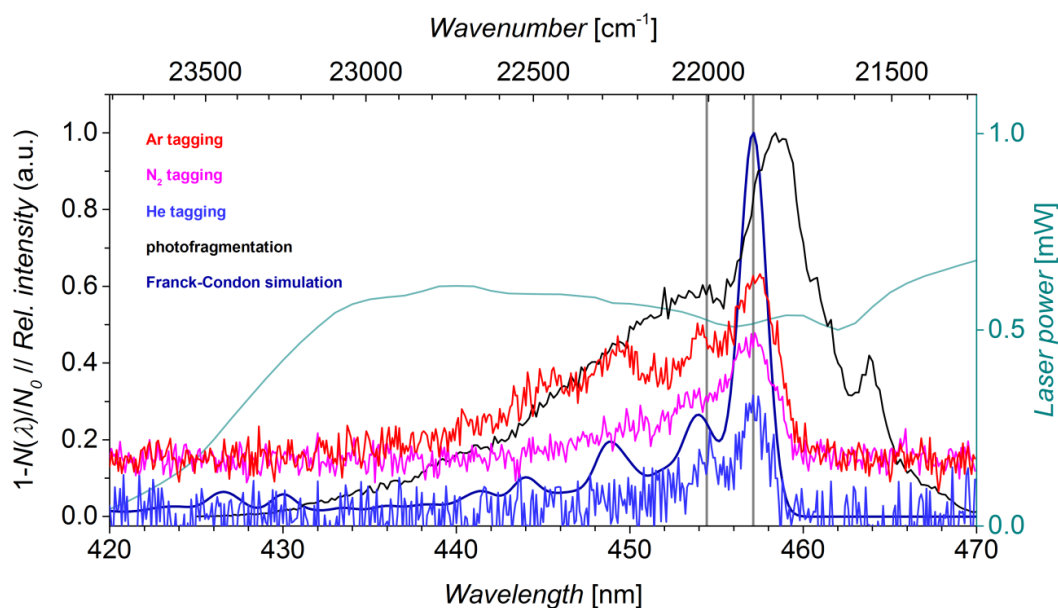


Figure 32. Comparison of helium-, argon- and nitrogen-tagging photodissociation spectra of rhodamine 123 ion measured at 4 K. The laser power was reduced to avoid signal saturation. The black spectrum corresponds to the photodissociation spectrum measured at 10 K (fragment with m/z 285 was monitored). The vertical lines denote the wavelengths of 0–0 and 10^1 transitions, respectively, the latter was assigned by theoretical calculations. The navy trace corresponds to the Franck-Condon simulation by DFT at the B3LYP-GD3BJ/6-311++G** level of theory.

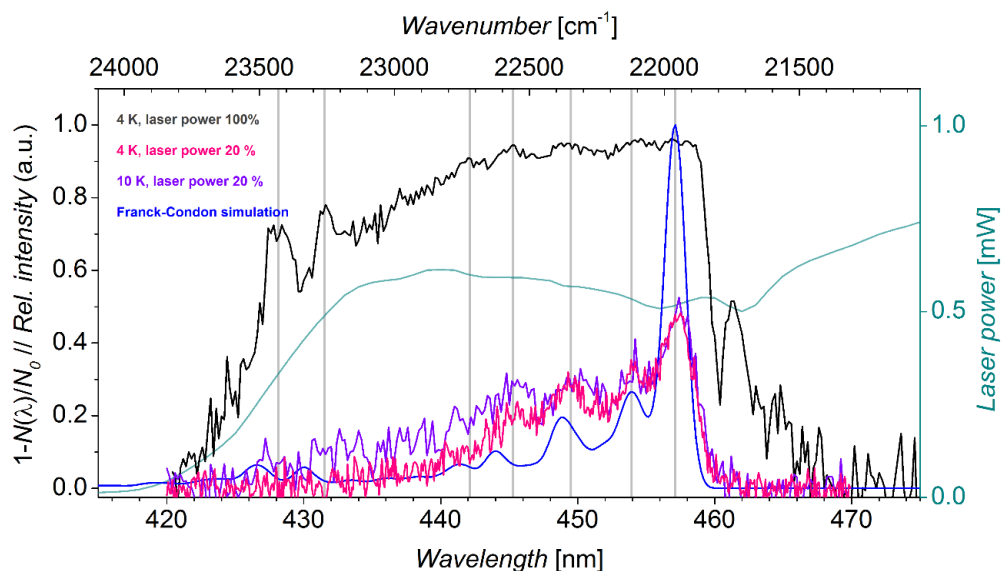


Figure 33. Comparison of argon-tagging photodissociation spectra of rhodamine 123 ion measured with full (black trace) and 20% (pink trace) laser power at 4 K and with 20% laser power at 10 K (violet trace). The blue trace corresponds to the calculated Franck-Condon envelope.

5.1.4 TEMPERATURE EFFECTS ON PHOTODISSOCIATION SPECTRA

In addition to tagging experiments, our experimental setup enables us to measure standard photodissociation spectra of bare ions. In rhodamine 123, several fragments were formed during its photodissociation upon 467 nm excitation (parent m/z 345, Figure 34), specifically at m/z 328 ($\Delta M_r = -17$), m/z 313 ($\Delta M_r = -32$), m/z 298 ($\Delta M_r = -47$), m/z 285 ($\Delta M_r = -60$) and m/z 270 ($\Delta M_r = -75$). The dominant fragmentation, which corresponds to the loss of 60 mass units and which I used in my PD experiments, most likely represents the elimination of the methyl ester group and a hydrogen atom (*i.e.*, methylformate). The loss of 17 mass units is likely caused by the elimination of ammonia. The remaining fragmentation channels likely account for the combined losses of ammonia and parts of the methyl ester group.

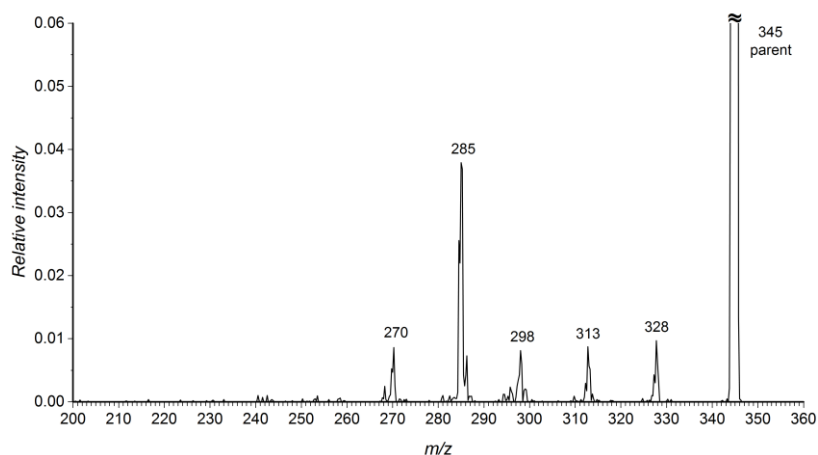


Figure 34. Photodissociation mass spectrum of rhodamine 123 after irradiating the parent ions (m/z 345) with 467-nm light (full laser power) at 300 K.

I measured the photodissociation spectrum of rhodamine 123 ions at 10 K by monitoring the prevalent fragmentation channel (loss of 60 mass units, Figure 35a), subsequently comparing it with the helium-tagging spectrum (Figure 29). Initially, I attempted to acquire the PD spectrum at 4 K for a more consistent comparison with the helium-tagging spectrum; unfortunately, the photodissociation yield strongly decreased below 10 K, thereby preventing me from acquiring any PD spectrum.

Interestingly, the comparison of both photodissociation methods showed that the absorption maximum in the PD spectrum is red-shifted by ~ 2 nm with respect to the helium-tagging spectrum (*cf.* Figure 35a and Figure 29). Interestingly, the same

effect has been described in photodissociation experiments of $[\text{TyrAla+H}]^+$; again, absorption maxima (including the 0–0 transition) in the helium-tagging spectrum were blue-shifted with respect to the photodissociation spectrum (Figure 12).¹⁰⁴

Another notable difference in the photodissociation spectrum of rhodamine 123 is the presence of hot bands in the PD spectrum located at ~ 464 and ~ 468 nm. As I already mentioned and demonstrated above, only fully vibrationally relaxed ions form complexes with helium. Conversely, bare rhodamine ions probed in photodissociation experiments are not fully vibrationally relaxed, despite using collisional cooling and experimental temperatures of 10 K. To work with more relaxed ions, I modified the trapping conditions in the ion trap to enhance their collisional cooling by prolonging the trapping time and by lengthening and intensifying the helium buffer gas pulses. Notwithstanding my efforts, I always observed hot bands in the photodissociation spectra, regardless of experimental settings, for unknown reasons, which might be associated with the ISORI experimental setup in general.

The PD spectra, which I recorded by monitoring two other fragmentation pathways (losses of 17 and 47 mass units), feature maxima at the same wavelength ($\lambda = 459.1$ nm, Figure 35a) as that of the spectrum in which I monitored the most dominant fragmentation channel (loss of 60 mass units). Thus, I showed that photodissociation of rhodamine 123 ions is fragment-independent, in contrast to many other ions.

After measuring the photodissociation spectrum at 10 K, I assessed whether (and how much) higher temperatures would affect the photodissociation spectra of rhodamine ions. As previously mentioned in Chapter 4.3, the ISORI instrument can operate the ion trap at any temperature in the 3–310 Kelvin range by switching-off the cold head when the ion trap reaches the desired temperature (100–300 K) or by simultaneously operating the coldhead cooling and resistor heating when working with temperatures ranging from 3 to ~ 60 K. Furthermore, acquiring data at temperatures of 100 K and higher can be somewhat serendipitous because recording spectra generally takes dozens of minutes, and in the meantime the ion trap slowly increases its temperature, causing several experimental limitations. Firstly, the ion trap changes its position horizontally within *ca.* 5 millimeters between 3 and 300 K, which is caused by thermal expansion of the materials used; therefore, the laser beam must be constantly re-focused. Secondly, trapping efficiency also depends on temperature (increasing with

the decrease in temperature); hence, the timing (*e.g.*, QPB pulse) and trapping conditions (number and duration of helium pulses) must be constantly re-adjusted to avoid saturating the detector, which is counting the ions. Eventually, saturation generates irreproducible photodissociation data, *i.e.*, the number of formed fragments does not equal the number of dissociated parent ions. Hence, the time at which ions enter the trap (regulated by QPB timing), the helium number density (regulated by the number and strength of helium pulses) and the voltage applied to the electrodes before and after the ion trap must be carefully altered at each experimental temperature.

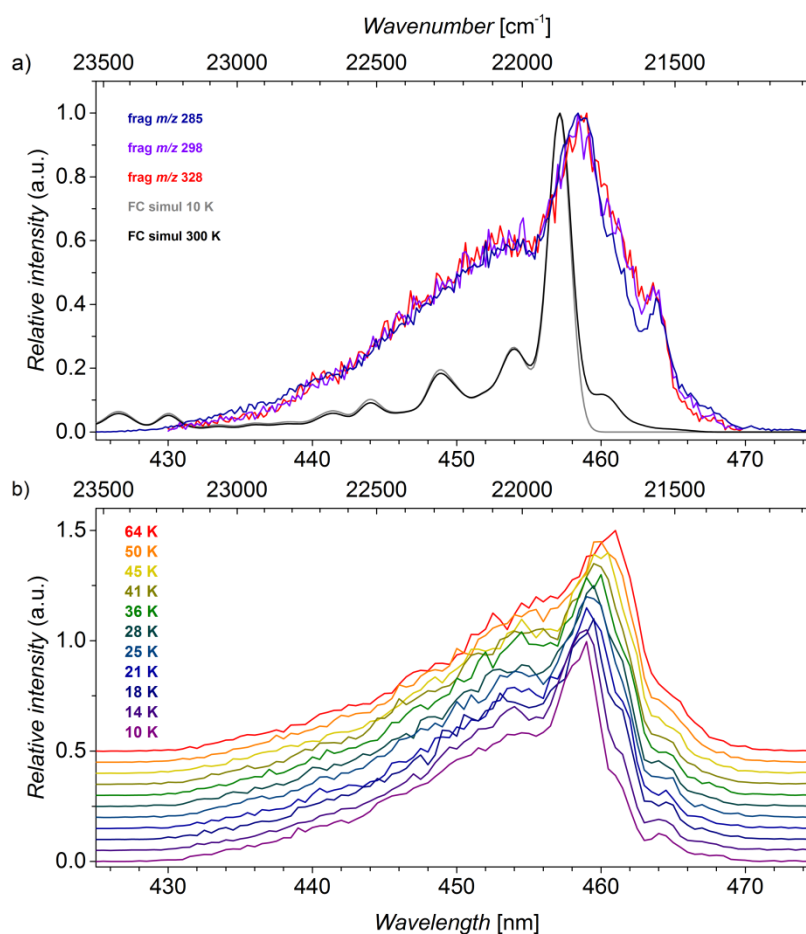


Figure 35. (a) Comparison of photodissociation spectra of rhodamine 123 measured at 10 K (full laser power) while monitoring different fragments (m/z 285, 298 and 328). The gray line shows the Franck-Condon envelope simulation at 10 K and the black line represents the simulation at 300 K. (b) Photodissociation spectra of rhodamine 123 ion measured at 10–64 K (fragment with m/z 285 was monitored; the total yield of photo-fragmentation was $\sim 5\%$).

Notwithstanding all experimental requirements described above, I was able to measure the photodissociation spectra of rhodamine 123 between 10 and 64 K in small temperature steps (Figure 35b) and subsequently in 50 K increments (100, 150, 200 and 300 K, Figure 36). At all temperatures, no PD spectra featured resolved Franck-Condon envelope, in contrast to the tagging spectra. In the 10–64 K temperature range, I observed a small shift (~ 1.5 nm) in the absorption maximum, which corresponds to the 0–0 transition, and an increase in the intensity of the hot band at ~ 464 nm. Around 45 K (yellow trace) and above, the 0–0 transition and the first hot band become indistinguishable. However, I cannot exclude the possibility that the observed temperature-induced shifts in the 10–64 K range result from a small horizontal movement of the ion trap. Accordingly, the cloud of stored ions would also be displaced, thereby deteriorating the correct alignment and overlap with the laser beam, which interacts with the ion cloud. Furthermore, because of the supercontinuum laser beam characteristics, the set wavelength slightly deviates within spatial areas of the beam. Hence, wavelength shifts in PD spectra could have been introduced by wavelength deviations of the laser beam (my tests have shown that PD spectra can be shifted by up to 4 nm due to this effect, in the worst-case scenario); unfortunately, there was no way to avoid these wavelength deviations in the 10–64 K experiment (Figure 35b). In all other experiments, specifically those at 10, 50, 100, 150, 200, 250 and 300 K, I was able to avoid these deviations, always correctly aligning the laser beam with the overlapping the ion cloud.

At higher temperatures (above 50 K), the absorption bands of vibrationally excited ions become continuously more pronounced (Figure 36a). At 150 K, the photodissociation of vibrationally excited ions becomes more significant. At 200 K, the 0–0 band at 459 nm and the hot band at ~ 467 nm exhibit similar intensities, and the latter eventually becomes the most intense absorption band at 300 K. Hence, photodissociation at room temperature is mostly dominated by dissociation of vibrationally excited ions, similarly to photodissociation studies, which also probed ions at elevated temperatures (Chapter 3.5, *e.g.*, Figures 11 and 14).

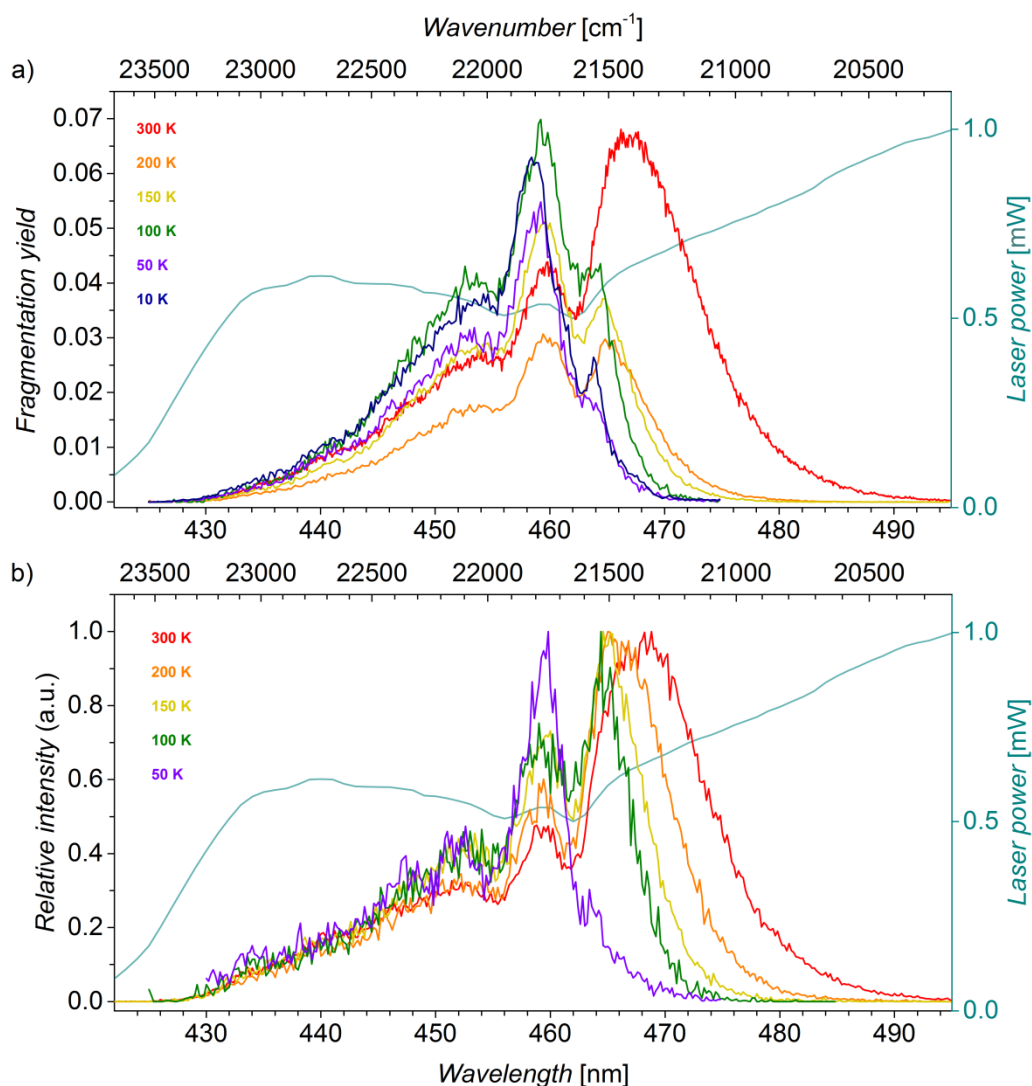


Figure 36. Temperature-dependent photodissociation spectra of rhodamine 123 (a) and rhodamine 110 (b) ions (fragments with m/z 285 were monitored in both cases). The PD yield of Rh 123 was 3.0–6.5% at 460 nm, and the spectra were normalized to the given fragmentation yield at this wavelength. The fragmentation yield error was approximately 20%, which most likely accounts for the decreased intensity of the spectrum measured at 200 K (orange trace). In (b), All spectra rhodamine 110 in (b) were normalized to the maximum intensity of 1.

To compare my data with a photodissociation study by Jockusch,¹⁷¹ I also measured temperature-dependent photodissociation spectra of rhodamine 110 (Figure 36b), which showed an identical temperature effect to that of rhodamine 123. The absorption maximum of rhodamine 110 at 300 K is located at 468 nm, whereas Jockusch reported an absorption maximum at 465 nm. This discrepancy can be

explained by 1) differences in populations of vibrationally excited ions, even though the experiments were performed at the same temperature (300 K), 2) differences in the experimental setups (wire quadrupole vs. linear quadrupole trap), and 3) the lower laser resolution of the PD spectrum reported by Jockusch, which was constructed from only 13 data points.

5.1.5 MULTIPHOTON CHARACTER OF PHOTODISSOCIATION SPECTRA

Based on previous photodissociation studies (Chapter 3.1),^{51-53,171} I predicted that the photodissociation of rhodamine ions would also be a multiphoton process. To confirm this assumption, I measured the fragmentation yield as a function of the laser power, which provides the number of photons absorbed to trigger photodissociation (Figure 37). Then, I fitted the resulting curves for rhodamine 123 using an exponential function in which the exponent equals the number of photons involved in photodissociation.

At 300 K, at irradiation wavelengths of 440, 453 and 460 nm, 3–4 photons are responsible for photodissociation (Figure 37). In contrast, photodissociation at 467 and 475 nm (hot band absorption, please refer to Figure 36) requires, on average, 3 photons. The same number of photons was estimated to trigger the photodissociation of closely related rhodamine 110 ions.¹⁷¹ Agreement between my and previously reported values shows that vibrationally excited ions fragment more readily than relaxed ions, which absorb at shorter wavelengths. Moreover, multiphoton photodissociation of rhodamine ions may involve fluorescence pumping, similarly to other ions featuring strong fluorescence deexcitation (Chapter 3.2, Figures 4 and 5). At 50 K, the ions have a lower vibrational energy; hence, the number of photons necessary for photodissociation increases to 4–5. Similarly, exponential fitting suggests that photodissociation at 10 K also requires 4–5 photons.

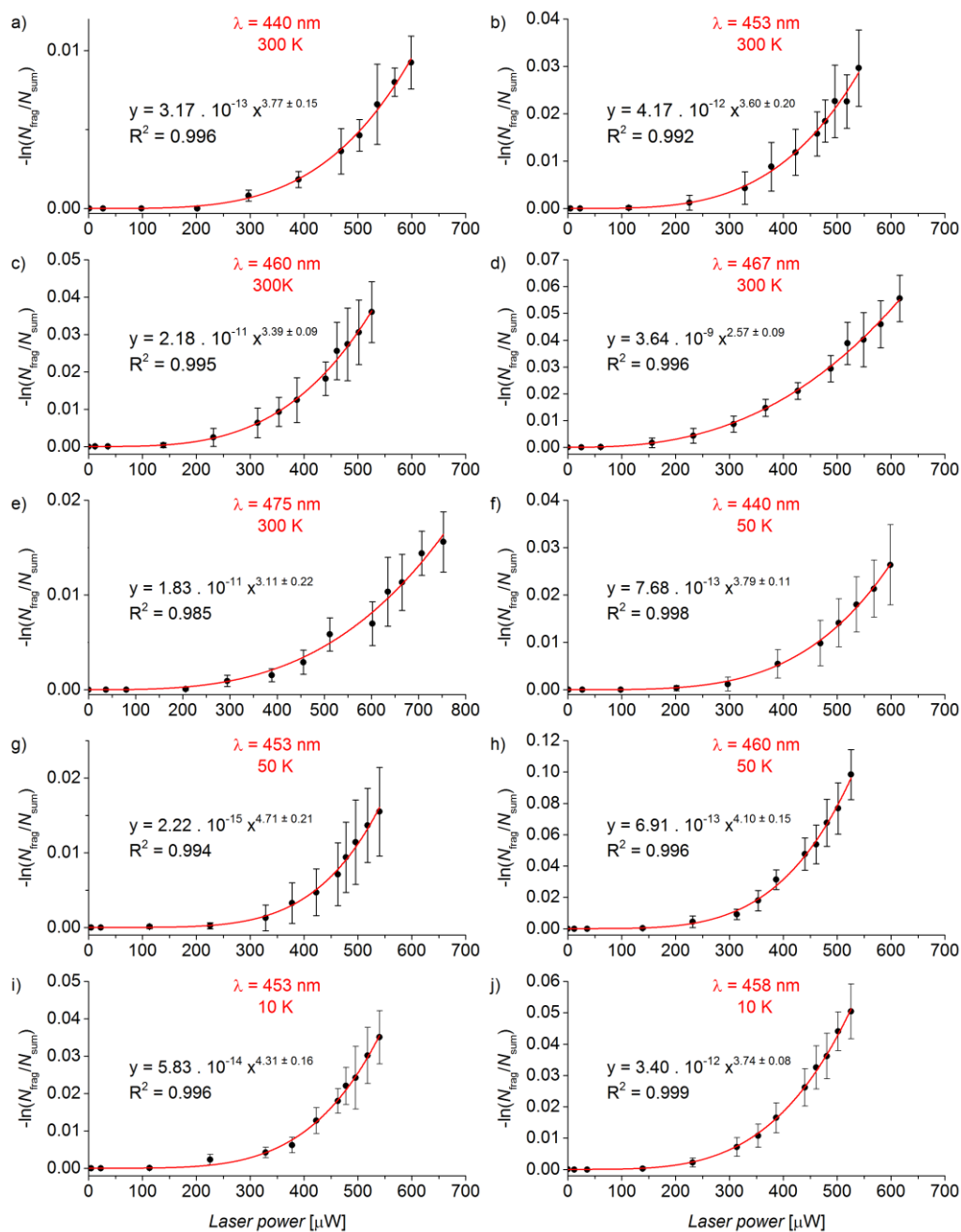
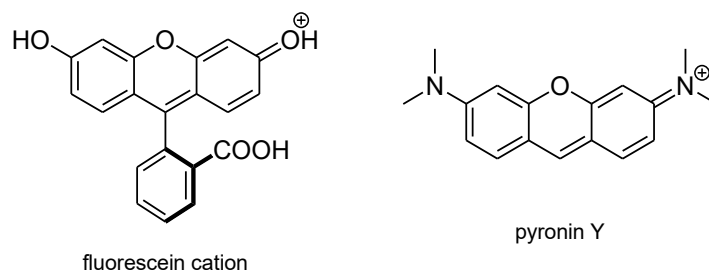


Figure 37. Photofragmentation efficiency as a function of laser power at specific excitation wavelengths at 300 K (a-e), 50 K (f-h) and 10 K (i-j). The red curves are exponentially fitted to black data points, which also include error bars showing their standard deviation. Exponents in equations provide an approximate number of photons, which are needed for dissociation at a given wavelength and temperature.

5.1.6 FURTHER INSIGHT INTO THE PHOTODISSOCIATION OF XANTHENE DYES

Thus far, I have focused on structurally related rhodamine ions in my photodissociation studies. However, I also wondered whether the absorption of other

cationic xanthene dyes also strongly depends on the experimental temperature. I selected and examined two additional and widely known xanthene derivatives, fluorescein cation and pyronin Y (Scheme 4). I chose fluorescein for its different substitution pattern at the xanthene core (OH instead of NH₂ groups) and pyronin Y as one of the simplest xanthene derivatives. Moreover, I assumed that the lack of a perpendicular benzene ring in pyronin Y, in comparison with other examined dyes, for instance, rhodamines, might affect temperature-dependent photodissociation spectra. Lastly, both selected compounds have already been studied by photodissociation spectroscopy; the absorption maximum of the fluorescein cation was reported at 420–430 nm (Figure 7a),³⁴ which was later refined to 425 nm,¹⁷⁴ and the absorption maximum of pyronin Y was reported at 517 nm.¹¹⁹



Scheme 4. Additional studied xanthene dyes.

First, I measured the helium-tagging spectrum of fluorescein at 3 K (Figure 38, red trace); in this case, I could not use the supercontinuum SuperK laser because its power output at wavelengths around and below 420 nm, where I expected fluorescein ions to absorb, is insufficient to trigger photodissociation. For this reason, I used a high-resolution UV/vis laser Sunlite EX OPO (please refer to Chapter 4.3).

The helium-tagging spectrum of fluorescein cation features the 0–0 transition at 420.8 nm with a relatively low intensity (Figure 38), especially in comparison with previously studied rhodamines ions. This suggests that fluorescein undergoes a more sizable nuclear distortion upon excitation than rhodamine derivatives. I attempted to confirm this inference by DFT calculations. First, I optimized the geometries of S₀ and S₁ states. For the latter, I typically used the broken symmetry approach; in simple terms, one electron from the HOMO is placed in the LUMO while retaining the overall singlet multiplicity, and then molecular coordinates are optimized, thus providing the geometry of the S₁ state (please refer to Chapter 4.5 for further computational

details). However, the broken symmetry approach failed in the optimization of excited fluorescein cation. In all my attempted calculations, the wave function converged back into the ground electronic state S_0 . I eventually succeeded in calculating the optimized S_1 geometry using the TD-DFT method at the ω B97X-D/6-31+G* level (analytical TD-DFT geometry optimization has been available since the release of Gaussian 16 version of this software). Interestingly, the angle between benzene and xanthene planes in S_1 state, which is 111° , markedly differs from the angle in the S_0 state, which is 90° . Unfavorable overlap between S_0 and S_1 geometries may thus account for the reduced intensity of the 0–0 and for several other vibronic transitions, which I detected in the helium-tagging experiment. Indeed, the Franck-Condon prediction of the $S_1 \leftarrow S_0$ transition confirms this hypothesis by providing a spectrum with very low spectral progression (low intensity) and, hence, questionable reliability.

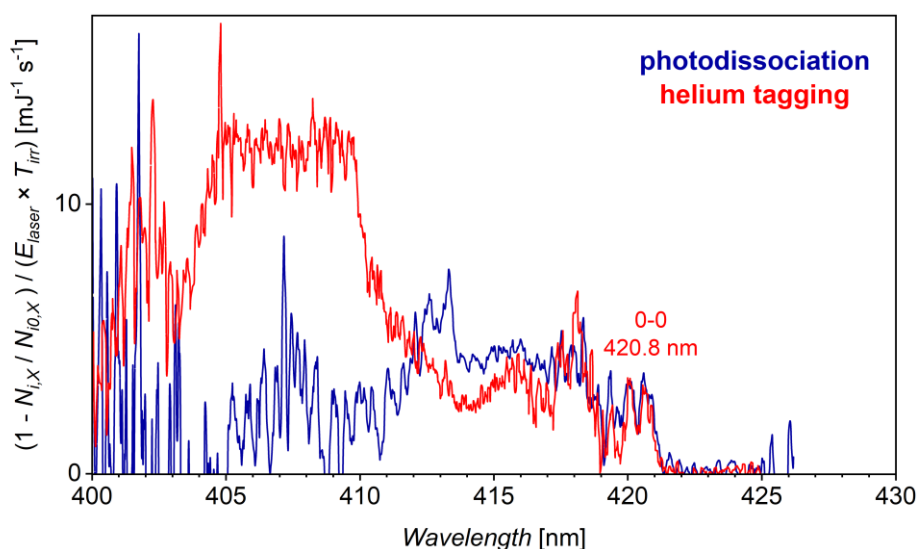


Figure 38. Comparison of photodissociation and helium-tagging spectra of fluorescein cation measured at 3 K. The intensity of the spectra was normalized to the energy of the laser (E_{laser}) and to the irradiation time (T_{irr}). The signal of the helium-tagging spectrum is saturated between 405 and 410 nm due to the increase in the power output of the laser. Below ~ 405 nm and above 425 nm, the PD signal is biased due to the decrease in photodissociation yield and in laser power.

The second notable feature of the helium-tagging spectrum is the line broadness (in this case not limited by the laser linewidth), which can also result from an unfavorable overlap of S_0 and S_1 geometries resulting in a broad Franck-Condon

envelope and/or from a short lifetime of the excited state (Chapter 3.2).^{42,43} The nature of the excited state is most likely rather complicated. Previous study showed that fluorescein emits no detectable fluorescence in the gas phase, even though fluorescein and its derivatives are highly fluorescent in solution. Hence, the dominant deexcitation pathway in the gas phase is most likely a different process with an unclear nature; proton transfer has been suggested to occur in the excited state.³⁴ This is particularly puzzling considering the relevance of deexcitation for the helium-tagging process and for its mechanism in particular.

I also recorded photodissociation spectra of the fluorescein cation at variable temperatures. Fluorescein exhibits numerous fragmentation channels, such as the loss of 46 mass units (m/z 287, Figure 39), which corresponds to dissociation of formic acid from the carboxylate moiety and which is the major fragmentation channel. The large number of fragmentation channels with similar intensities apparently stems from several, similarly strong chemical bonds, which dissociate in the excited fluorescein cation. However, the efficiency of individual fragmentation channels, which is rather low, could impede photodissociation experiments. Hence, instead of monitoring several dissociation channels simultaneously, I monitored the depletion of the parent fluorescein signal (m/z 333).

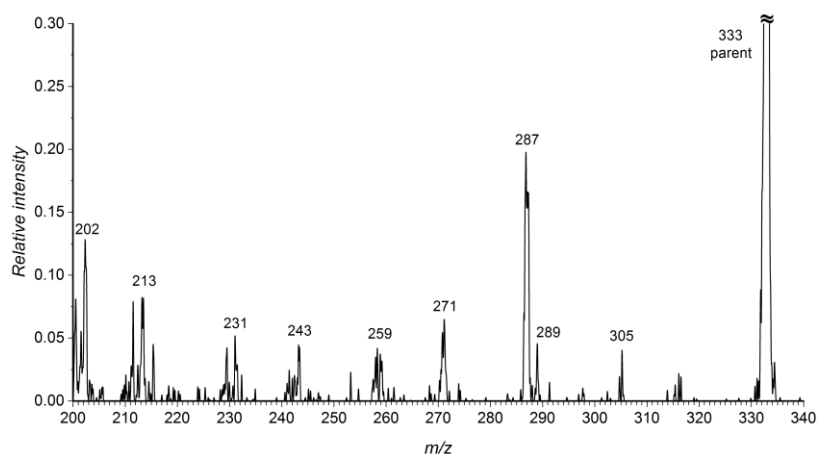


Figure 39. Photodissociation mass spectrum of fluorescein cation (m/z 333) recorded after irradiation with a 414-nm laser light (250 μ J) at 295 K. Please note that the laser power used for the actual spectra measurements was decreased by more than 10-fold to avoid PD signal saturation.

The PD spectrum measured at 3 K is shown in Figure 38 together with the helium-tagging spectrum for comparison purposes. The positions of the 0–0 transition (420.8 nm) and several subsequent absorption bands are virtually identical in both spectra. Yet both spectra start deviate below *ca.* 413 nm; the PD spectrum retains vibrational resolution, whereas the signal of the helium-tagging spectrum is saturated due to increase in laser power and thus lacks any vibronic structure. The reason for such difference remains unknown and requires further experiments for clarification.

Figure 40 shows PD spectra of fluorescein measured at 3, 45 and 300 K. The three spectra substantially differ in intensity, band position and vibronic structure. The most intense is the spectrum measured at 45 K, meaning that the photodissociation

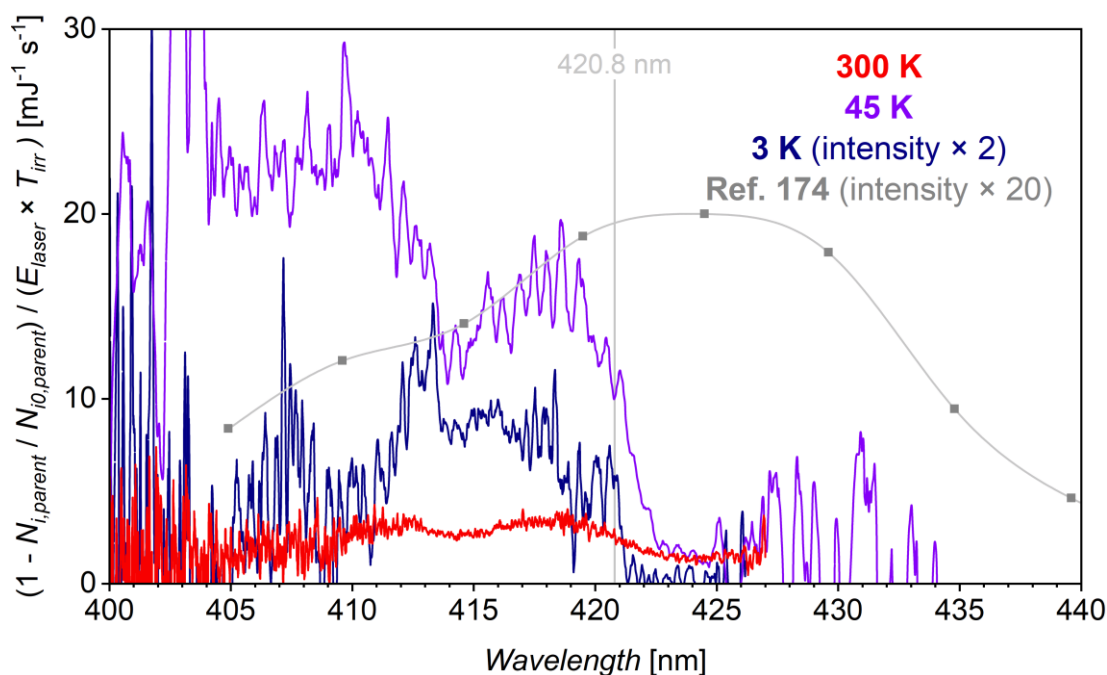


Figure 40. Temperature-dependent photodissociation spectra of the fluorescein cation obtained by monitoring the attenuation of the parent ion signal (m/z 333). The intensity of the spectra was normalized to the energy of the laser (E_{laser}) and to the irradiation time (T_{irr}). The reduced signal-to-noise ratio, below ~ 405 nm and above ~ 427 nm, results from the significantly decreased photodissociation yield and from instabilities of the laser power output. A previously reported PD spectrum of fluorescein measured at ambient temperature is also included (gray points and trace; note that the intensity in that spectrum, corresponding to the PD yield, was multiplied by 20 to allow a direct comparison with my data; please refer to Figure 7a for the original PD spectrum).¹⁷⁴

at 45 K was the most efficient, whereas the efficiencies at 3 and 300 K were lower. The spectra at 3 and 45 K featured resolved vibronic bands, in contrast to the spectrum at 300 K. The linewidth of the 0–0 (located at 420.8 nm) and other vibronic bands increased with the temperature, as shown when comparing the spectra measured at 3 and 45 K. The 0–0 transition in the 300 K spectrum cannot be assigned because the spectrum lacks vibronic structure and thus provides limited information on the excited state nature and structure.

In Figure 40, I also included the previously reported PD spectrum of fluorescein recorded at ambient temperature for comparison purposes (gray trace and data points).¹⁷⁴ Interestingly, the position of the previously reported absorption maximum, at 425 nm, differs not only from the spectra I measured at low temperatures (3 and 45 K, 420.8 nm) but also from the spectrum measured at 300 K. Different instruments and experimental setups, particularly different ion trap arrangements, affect the collisional cooling of ions, which causes differences in the internal energy distribution of ions. The internal energy of ions changes the efficiency of ion photodissociation at a specific wavelength. Most likely, the main complication is the multiphoton nature of the photodissociation process in general, which exacerbates effects associated with the vibrational energy levels of ions. Thus, PD spectra recorded using two different instruments, even when using the same experimental temperature, do not necessarily match. Accordingly, single-photon photodissociation, such as helium-tagging, provides more reliable results, albeit precluding experiments in a wide temperature range.

Lastly, I investigated the photodissociation of pyronin Y, the smallest xanthene chromophore included in this Thesis, using both available tunable vis lasers, Supercontinuum SuperK laser with low (1.8 to 8.5 nm depending on the wavelength) and Sunlite EX OPO laser with high resolution (linewidth $< 0.1 \text{ cm}^{-1}$). Photodissociation spectra of pyronin Y resemble those of previously discussed rhodamine ions (Chapter 5.1.4). Figure 41a shows the comparison between PD spectra measured at 300, 150 and 50 K together with the helium-tagging spectrum acquired at 3 K. Similarly to rhodamines, PD spectra feature a broad and intense hot band at $\sim 531 \text{ nm}$, which decreases in intensity with the decrease in temperature until 50 K at which temperature the hot band is no longer detected. The second absorption feature at 522 nm prevails in the entire temperature range and eventually becomes the most

intense absorption band at 50 K. Overall, the PD spectra contain no other vibronic features, except for the 522 nm band.

Based on the helium-tagging spectrum (Figure 41a, navy trace), I assigned the 522 nm band to the 0–0 transition. The helium-tagging spectrum features several other vibronic bands at 515, 506, 499 and 490 nm. I simulated the Franck-Condon envelope by DFT calculations, which clearly agreed with the experimental helium-tagging spectrum (Figure 41b, navy trace). Based on the results, I concluded that the spectra of pyronin Y correspond to the $S_1 \leftarrow S_0$ transition.

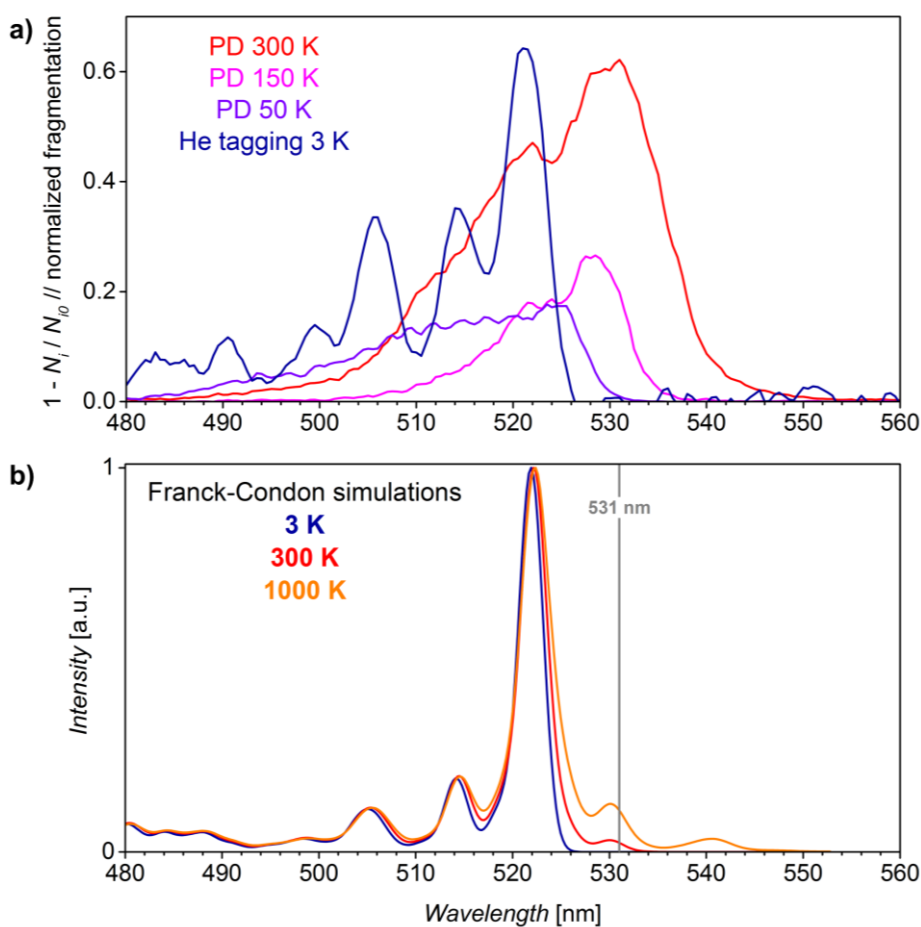


Figure 41. (a) Helium-tagging and photodissociation spectra of pyronin Y measured at different temperatures. PD spectra were acquired by monitoring the formation of a fragment with m/z 251 (loss of 16 mass units from the parent, Figure 42) and normalized to the intensity of the parent signal (m/z 267). (b) Franck-Condon envelope simulations at 3, 300 and 1000 K. The 0–0 transition energies in simulated spectra were shifted to match the position of the experimental 0–0 transition (522.216 nm recorded in high-resolution experiments, *vide infra*).

Additionally, I addressed the band at 531 nm, most likely a hot band, in the 300 and 150 K spectra, by modifying the temperature parameter in Franck-Condon simulations (Figure 41b). The Franck-Condon simulation at 3 K contains no transition originating from the vibrationally-excited state. However, the simulation at 300 K contains a small shoulder located at 530 nm. To highlight the temperature effect, I also performed a simulation at 1000 K. Although this temperature is far from the experimental conditions used in this study, the simulation at 1000 K clearly shows an increase in the intensity of this specific vibronic band with the temperature. Nevertheless, all simulations failed to reproduce the experimental intensity of this very intense hot band, unsurprisingly, because theoretical predictions overlook the multiphoton nature of the photodissociation process itself, which in principle introduces bias into the relative intensities of absorption bands. Moreover, the photodissociation at the hot band (531 nm) could require fewer photons than that in the rest of the PD spectrum, as observed in PD spectra and in the curves representing the variation of photodissociation as a function of laser power of rhodamine 123 ions (Chapter 5.1.5, Figure 37). Accordingly, the absorption intensity at 531 nm would be stronger than in the rest of the experimental spectrum. Lastly, the limited accuracy of DFT methods should also be considered.

Notwithstanding the aforementioned difficulties, I sought to more accurately determine the energy of the hot band transition, which would enable me to assign this hot

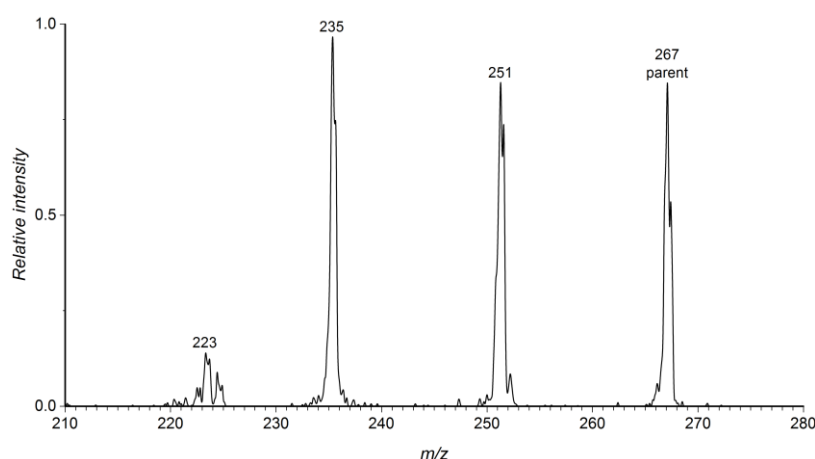


Figure 42. Photodissociation mass spectrum of pyronin Y ions (m/z 267) recorded after irradiation with 522.4 nm light (400 μ J) at 295 K. Please note that the laser power used in actual spectra measurements was decreased by more than 10-fold to avoid PD signal saturation.

band to a specific normal vibrational mode of pyronin Y ion. Therefore, I measured PD spectra using a high-resolution laser. Firstly, as shown in Figure 42, which depicts the photodissociation mass spectrum of pyronin Y at 295 K, photodissociation was quite efficient with two major and most likely consecutive dissociation channels: loss of 16 and 32 mass units, which correspond to the loss of one and two CH₄ fragments, respectively. Additionally, I observed a less intense loss of 44 mass units, resulting from the dissociation of a dimethylamino group.

Figure 43 shows the PD spectra of pyronin Y ions recorded at 3, 20, 45, 100 and 300 K. For the same reasons described in the fluorescein study (*vide supra*), I monitored only the attenuation of the parent pyronin Y signal (m/z 267) in PD experiments. The spectra feature a sharp vibronic structure, clearly shows the 0–0 band at 522.423 nm at 3 K, in addition to those acquired at 100 and 300 K spectra, which display considerably increased spectral congestion. Upon closer inspection, the vibronic bands show broadening already at 45 K. Similar broadening effects caused by temperature have already been observed in different studies, as discussed in Chapter 1.1.5. The main reasons for the temperature broadening effect are the population of the higher vibrational and rotational levels, which are very close in energy, and/or the shortened excited state lifetime (Chapter 3.2).^{42,43} Please note that the broad

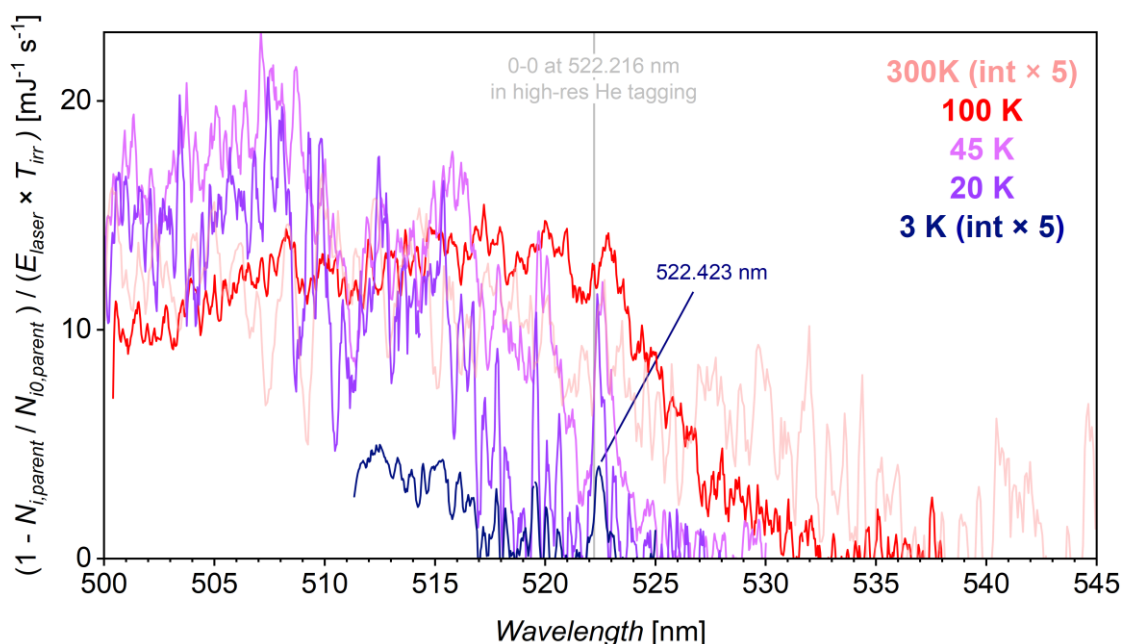


Figure 43. Temperature-dependent photodissociation spectra of pyronin Y recorded by monitoring the attenuation of the parent ion signal (m/z 267). The spectra were normalized to the energy of the laser (E_{laser}) and to the irradiation time (T_{irr}).

spectrum measured at 300 K contains no artefacts caused by the fluctuations of laser power or by inaccurate laser beam alignment.

The increase in spectral congestion, unfortunately, prevented me from ascertaining which specific vibration (*i.e.*, a normal vibrational mode) accounts for absorption at longer wavelengths. The results nevertheless show that several low frequency vibrations very efficiently couple to the $S_1 \leftarrow S_0$ electronic transition with the increase in temperature and thus broaden the electronic absorption bands.

I also measured the helium-tagging spectrum of pyronin Y at 3.2 K (Figure 44), and I referenced the plotted spectrum with respect to the 0–0 transition located at 522.216 nm (19149.2 cm^{-1}). Similarly to fluorescein photodissociation spectra, the 0–0 transition of pyronin Y is not the most intense band. However, unlike fluorescein, the spectrum of pyronin Y features a highly resolved vibronic structure, and vibronic bands can be assigned to specific vibrations of the excited molecule. Based on my DFT calculations, I assigned vibronic bands at $400\text{--}700 \text{ cm}^{-1}$ to deformation vibrations of the xanthene moiety, those at $800\text{--}1000 \text{ cm}^{-1}$ to wagging vibrations of aromatic C–H bonds and those at $1100\text{--}1260 \text{ cm}^{-1}$, the most intense bands in the spectrum, to wagging and twisting vibrations of methyl groups. Moreover, I measured the region of the first 200 cm^{-1} using an increased laser resolution (Figure 44, right panel). Numerous bands are present in this region, even though DFT calculations predicted

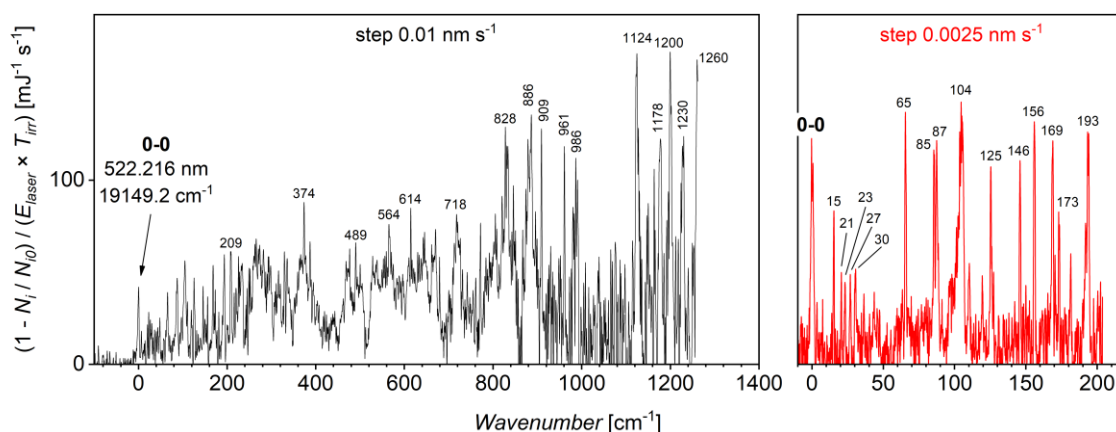


Figure 44. Helium-tagging spectra of pyronin Y ion measured at 3.2 K. The red spectrum was acquired by decreasing the scan rate of the laser and hence by increasing the resolution (step size 0.0025 nm s^{-1} , duration of cycle 1 s). Both spectra were referenced with respect to the origin, the 0–0 transition, located at 522.216 nm (19149.2 cm^{-1}).

only 6 infrared-active vibrations in this frequency region. The detected low-frequency vibronic bands, although partly assignable to deformations of the whole pyronin molecule, most likely correspond to a rotational structure and/or to artifacts of the helium-tagging method (*vide infra*). Furthermore, the 200–900 cm^{-1} region exhibits broader bands than the remaining parts of the spectrum.

Lastly, I compared the helium-tagging spectrum with the photodissociation spectrum of pyronin Y measured at 3 K. In the former, the 0–0 band is located at 522.216 nm (19149.2 cm^{-1}); in contrast, in the latter, the 0–0 band emerges at 522.423 nm (19141.6 cm^{-1}); hence, the difference in 0–0 positions is $\sim 0.2 \text{ nm}$ ($\sim 8 \text{ cm}^{-1}$), which could actually be an artifact of the helium-tagging method, corresponding to an energy difference in helium-binding energies between the S_0 and S_1 states of approximately 8 cm^{-1} ($\sim 0.1 \text{ kJ mol}^{-1}$). Surprisingly, this value is similar to the helium-binding energies calculated for helium-tagged rhodamine 123 ions (Chapter 5.1.3, Table 1), which are presumably equal to those of helium-tagged pyronin Y. Moreover, a few wavenumbers shifts in maxima of absorption bands when comparing helium-tagging with photodissociation spectra have previously been reported in (Figure 12).¹⁰⁴ Additionally, similarly sizable shifts in absorption maxima have also been reported among differently tagged C_{60}^+ ions.⁷³ Although, in both studies, the authors failed to explain the shifts in absorption maxima, differences in helium-binding energies between the S_0 and S_1 states may also account for those shifts.

In addition to the shifts in absorption maxima, helium-tagging could also have other effects on the electronic spectra. For this reasons, I compared the region of low-frequency vibronic bands of helium-tagging and photodissociation spectra of pyronin Y (0–200 cm^{-1} , Figure 45). Several vibronic bands were absent from the photodissociation spectrum, specifically those with frequencies of 21, 30 and 44 cm^{-1} , among others; thus, these vibronic bands are most likely another artifact of the helium-tagging. Furthermore, this comparison unveiled minor frequency shifts of some vibronic bands, *e.g.*, the band at 104 cm^{-1} . Therefore, helium-tagging has no significant effects on pyronin Y spectra although some minor frequency shifts and additional absorption bands can be detected when using high-resolution experimental setups.

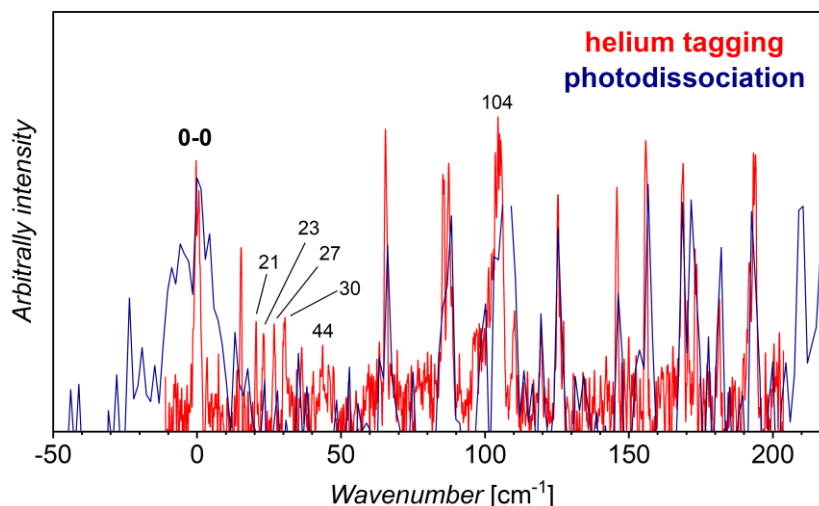


Figure 45. Comparison between helium-tagging (red trace) and photodissociation (blue trace) spectra of pyronin Y. Both spectra were referenced in respect to the energy of the 0–0 transition. The intensity was set for direct comparison purposes.

5.1.7 CONCLUSION

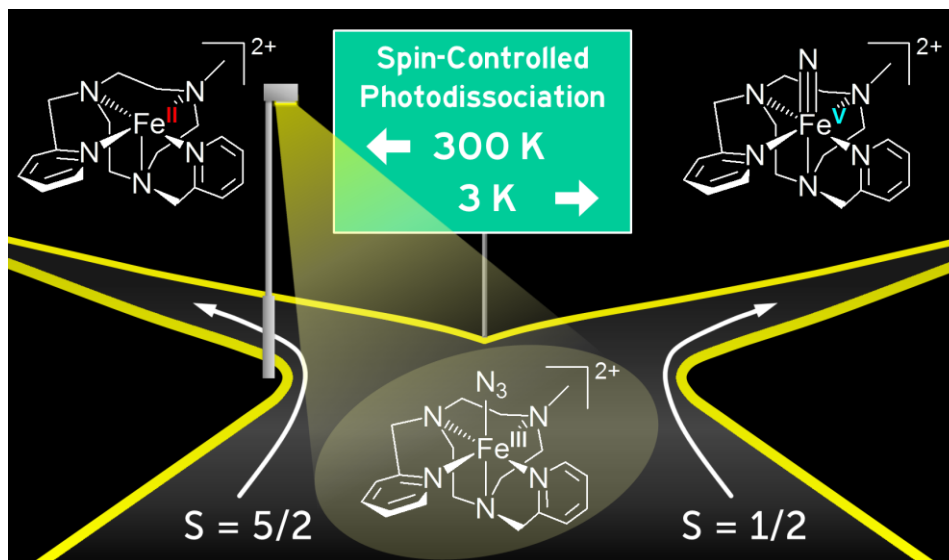
I measured helium-tagging and photodissociation spectra of cationic rhodamine, fluorescein and pyronin ions in the visible range, and I demonstrated that the tagging method can compete with other deexcitation processes (*e.g.*, fluorescence, radiative cooling); thus, the helium-tagging method can be used to measure electronic spectra of highly fluorescent ions. Vibrational resolution of spectra and Franck-Condon simulations allowed me to assign experimental spectra to $S_1 \leftarrow S_0$ transitions and to determine 0–0 transition energies. Furthermore, I assessed the tagging effect on electronic spectra. The spectra of helium-, argon- and nitrogen-tagged rhodamine ions displayed only small shifts in their absorption maxima, but the binding energies in S_0 and S_1 states were virtually equal even though the calculated binding energies of helium, argon and nitrogen differed in the ground S_0 state. In the case of pyronin Y ion, I estimated that the difference in binding energies between its S_0 and S_1 states was approximately 8 cm^{-1} ($\sim 0.1 \text{ kJ mol}^{-1}$), which is undetectable in low-resolution spectra. Furthermore, the tagging method, even when using weakly bound helium, can introduce some artifacts.

Subsequently, I developed an experimental method for assessing temperature effects on photodissociation spectra of ions, which enabled me to study the photodissociation of rhodamine, fluorescein and pyronin ions in the 3–300 K range. Interestingly, the results showed that photodissociation spectra of rhodamine

and pyronin ions are indeed temperature-sensitive, as shown by the efficient photodissociation of vibrationally excited ions, which become increasingly more populated with the increase in experimental temperature. The spectra of the fluorescein cation were even more complicated and thus warrant further studies beyond the scope of this Thesis. Moreover, I established that the photodissociation of rhodamine ions requires 3–5 photons, depending on the excitation wavelength and temperature, in line with a previous photodissociation report on rhodamine 110.¹⁷¹

Overall, my results show that tagging photodissociation spectroscopy is a viable tool for studying absorption characteristics of isolated ions and can provide invaluable data for benchmarking and improving computational methods for molecules, such as xanthene derivatives, which are otherwise difficult to describe.

5.2 PHOTODISSOCIATION OF IRON(III) AZIDES



This chapter is based on results reported in “Andris, E.; Navrátil, R.; Jašík, J.; Sabenya, G.; Costas, M.; Srnec, M.; Roithová, J. *Spin-State-Controlled Photodissociation of Iron(III) Azide to an Iron(V) Nitride Complex*. *Angew. Chem. Int. Ed.* **2017**, *56*, 14057–14060”.

5.2.1 INTRODUCTION

High-valent iron-containing enzymes and complexes are effective catalysts in natural and synthetic oxidation reactions involving strong and unactivated C–H bond cleavage in hydrocarbons.^{175,176} Although numerous reports have focused on understanding the chemical and spectroscopic properties of iron-oxo compounds involved in such oxidations,¹⁷⁷ much less is known about closely related iron-nitrido compounds.

High-valent iron nitrides, featuring a terminal nitrido ligand bound to an iron center in a high oxidation state (*e.g.*, Fe(V)≡N), are the proposed intermediates of challenging reactions such as nitrogen atom transfer,¹⁷⁸ nitrogen fixation¹⁷⁹ and industrial Haber-Bosch ammonia synthesis.¹⁸⁰ Despite their relevance to these important processes, few iron nitrides have been successfully generated and characterized. This mostly stems from their highly reactive and thermally unstable nature, resulting from their high oxidation state and unfavorable orbital interactions in pseudo-octahedral iron nitrides,¹⁸¹ which weaken the iron-nitrogen bond. Accordingly, all iron nitrides studied thus far are limited to simplified synthetic models of complex enzymatic and catalytic systems. Therefore, further studies are required to broaden our knowledge on challenging chemical transformations catalyzed by these reactive species.¹⁸²

The primary route for the generation of iron nitrides is the photolysis of labile azido ligand in iron(III) azide precursors, as first reported in the porphyrin-iron(III) azide complex.¹⁸³ The process of iron nitride generation, formally photooxidation, involves a heterolytic N–N bond cleavage and yields an iron(V) nitride concomitantly with the formation of N₂ (illustrated in Figure 46 and Scheme 5). However, an alternative process, formally photoreduction, competes with photooxidation and produces an undesired iron(II) complex and azido radical. Lastly, a redox-neutral process involving heterolytic Fe–N bond cleavage and thus providing an iron(III) complex and an azide anion has been identified using time-resolved infrared spectroscopy.¹⁸⁴

The ratio between desired photooxidation and unwanted photoreduction depends on the experimental temperature and on the irradiation wavelength.¹⁸⁵ Due to their thermal instability, the generation and characterization of high-valent iron nitrides have so far been restricted to experiments under cryogenic conditions, such as a frozen acetonitrile matrix cooled to 4 K¹⁸³ or 77 K.^{129,186} More recently, the formation of iron

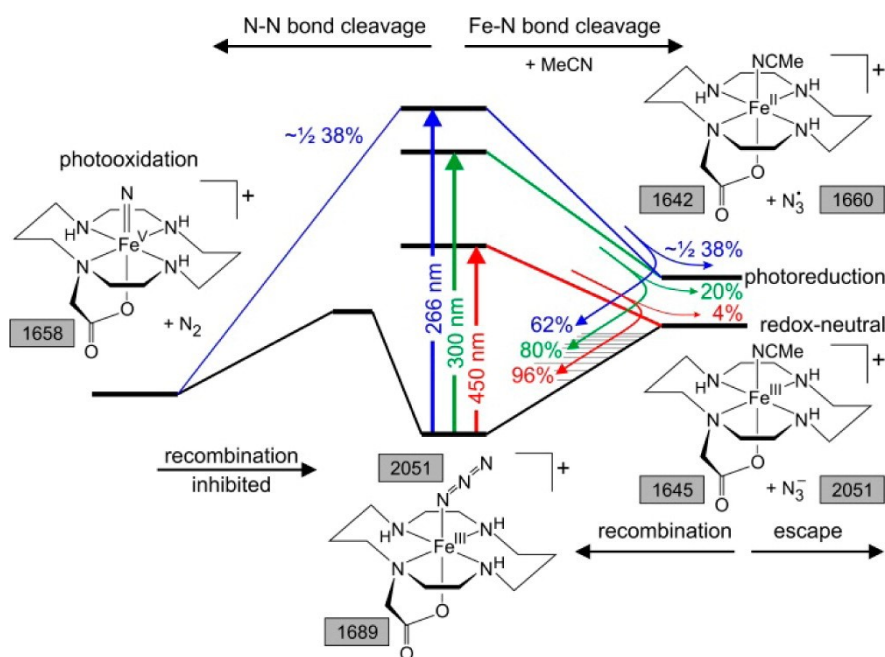


Figure 46. Overview of photochemical processes occurring after electronic excitation of the iron(III) azide complex $[(\text{cyclam-ac})\text{Fe}^{\text{III}}(\text{N}_3)]^+$ in acetonitrile solution under ambient conditions. The values in gray boxes indicate vibrational frequencies (in cm^{-1}) of detected carbonyl and azide vibrations. Reprinted from ref. 184. with permission. Copyright American Chemical Society (2014).

nitrides has also been shown at ambient temperature by ultrafast transient spectroscopy.^{184,187-189} Despite these reports, our overview of the photochemistry of pseudooctahedral iron(III) azides is still limited, and the underlying principles that determine and explain the outcome of iron azide photolysis remain mostly unknown.

Based on our previous experience with temperature-dependent photodissociation experiments (Chapter 5.1), we applied this method to investigate the photochemistry of iron(III) azides isolated in the gas phase. We presumed that gas-phase techniques would allow us to study photooxidation and photoreduction processes independently, at the molecular level, with no interference from solvent or other surrounding molecules, which are permanently present in the condensed phase. Moreover, our experimental setup would provide us with full control of experimental conditions, such as temperature and irradiation wavelength.

Our collaborators from the group of Professor Miquel Costas (University of Girona, Spain) had previously synthesized and studied an iron(III) azide complex $[(\text{MePy}_2\text{TACN})\text{Fe}(\text{N}_3)]^{2+}$ (**1**, $\text{MePy}_2\text{TACN} = N\text{-methyl-}N',N''\text{-bis-(2-picolyl)-1,4,7-$

photooxidation of **1** to **2** (m/z 198.5, red trace) and the loss of $N_3\cdot$ that corresponds to photoreduction of **1** to **3** (m/z 190.5, navy trace). Surprisingly, the spectra constructed from these two individual photodissociation channels display distinct absorption profiles with absorption maxima at 530 and 600 nm for the N_2 dissociation and at 455 nm for the $N_3\cdot$ dissociation (highlighted by gray vertical traces in Figure 48). Moreover, we observed that PD spectra, specifically the ratio between photooxidation and photoreduction, depend on temperature. $N_3\cdot$ loss is the major dissociation channel

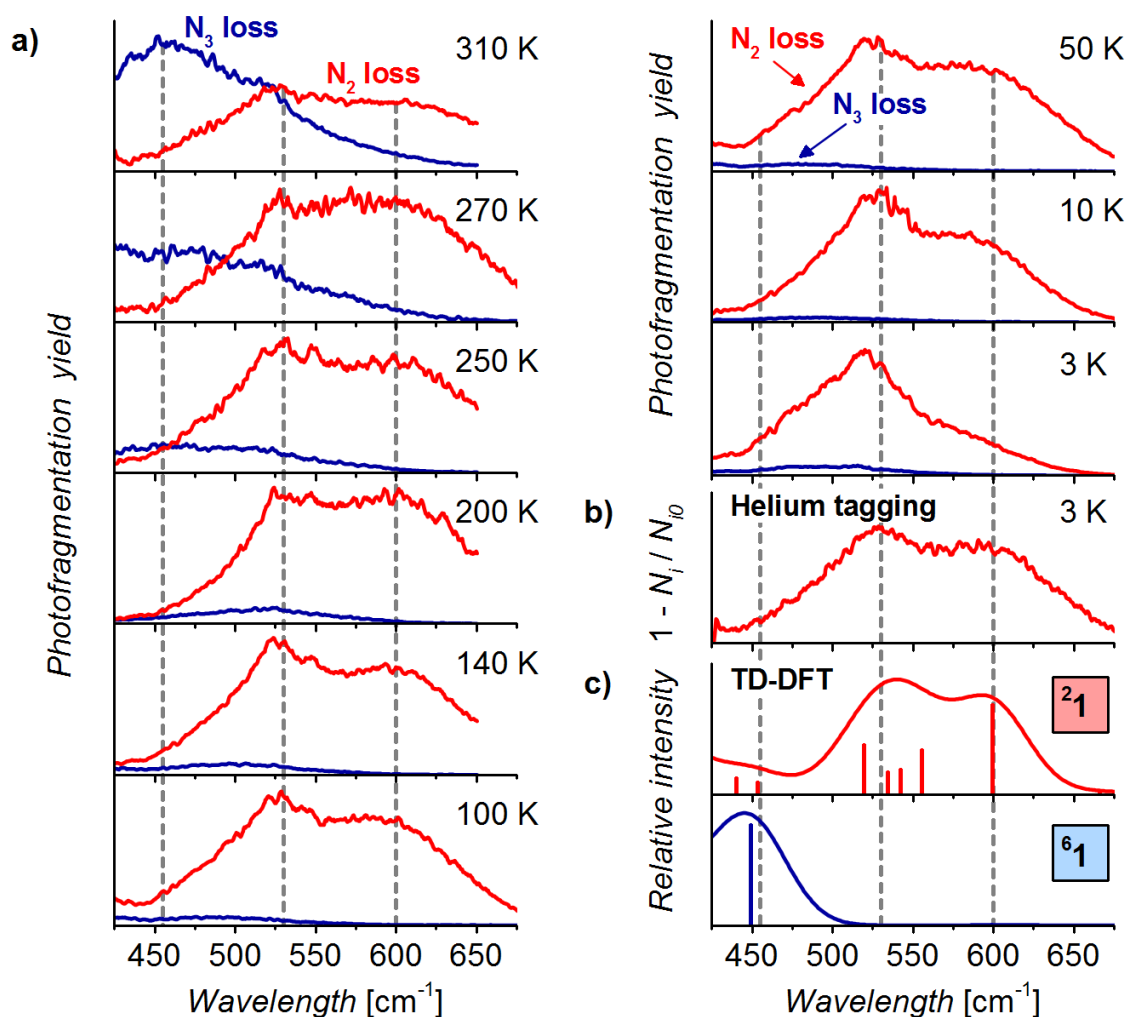


Figure 48. (a) Temperature-dependent photodissociation spectra of iron(III) azide **1** in which we monitored the formation of iron(II) complex **2** (loss of $N_3\cdot$, navy traces) and iron(V) nitride **3** (loss of N_2 , red traces). (b) Helium-tagging spectrum of **1** measured at 3 K. (c) Theoretical TD-DFT spectra of doublet (21 , red trace) and sextet (61 , blue trace) ground state iron(III) azide **1** calculated at B3LYP-D3/6-311++G** level of theory. The TD-DFT spectra were red-shifted by 25 nm to better fit the experimental data.

at 310 K, and its intensity diminishes with the decrease in temperature. Conversely, N₂ loss becomes more pronounced with the decrease in temperature and eventually becomes the major dissociation channel at 3 K.

The temperature of the ion trap, in which the ions are trapped and probed, directly affects the internal energy of the ions subjected to photodissociation. N₃[•] dissociation became inefficient below 200 K; in contrast, below 50 K, the photodissociation yield at longer wavelengths decreased, and the N₂ dissociation absorption maximum at 600 nm diminished. The observed temperature effect may result from interconversion between two isomeric forms of **1** with distinct absorption and fragmentation profiles from other relaxation processes enabled at low temperatures.

To better understand the photochemistry of **1**, we measured its helium-tagging spectrum at 3 K (Figure 48b). The comparison between the helium-tagging spectrum and PD spectra showed that the former displayed an absorption profile similar to those of the PD spectra in which we monitored the loss of N₂ and detected two absorption maxima located at 530 and 600 nm. The absorption maximum at 455 nm detected in the N₃[•] dissociation was absent from the helium-tagging spectrum. The species with the same absorption profiles in N₂ dissociation and helium-tagging spectra differs from the species that absorbs at 455 nm and dissociates N₃[•]. Thus, we concluded that iron(III) azide **1** exists in two isomeric forms, which display different absorption spectra, yield distinct photodissociation products and interconvert as a function of temperature.

Our results are similar to the findings of a previous study on hydrated protonated phenol, which also identified two isomeric species interconverting with temperature (Figure 15).¹¹⁰ However, in our experiments, the dissociation of **1** isomers provided two independent photodissociation channels; thus, isomer interconversion could be visualized by plotting the ratios of N₂ and N₃[•] photodissociation yields as a function of temperature at a chosen wavelength (Figure 49). At 455 nm, the yield of N₃[•] loss steeply decreased with the temperature along with a reduction in overall PD yield. Below 200 K, the PD yield at 455 nm increased to some extent, as a result of the increase in the N₂ dissociation yield of the higher energy part of the 530 nm band. We observed similar trends in PD yields measured at 530 and 600 nm; the N₃[•] photodissociation yield was negligible below ~200 K, but it increased above this temperature, with a maximum contribution to the total PD yield at 530 nm.

At all wavelengths, N_2 loss is the dominant dissociation process, and its efficiency increases with the decrease in temperature. Total PD efficiency follows the same trend, except for the 3–20 K temperature range in which some other non-dissociative relaxation processes (*e.g.*, radiative cooling or fluorescence, please refer to Chapter 3.2) became more efficient and accounted for the decrease in overall PD yield. The mutual dependence of N_2 and $N_3\cdot$ photodissociation yields suggests that both channels originate from a single or two interconverting precursors.

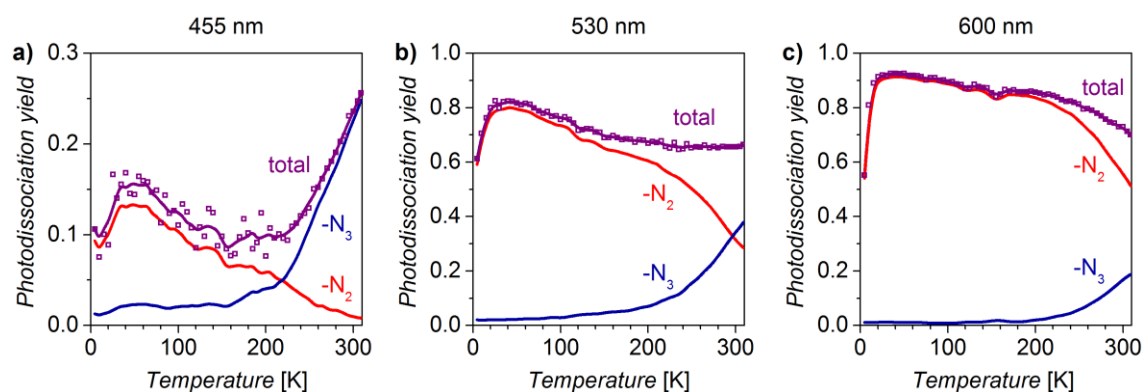
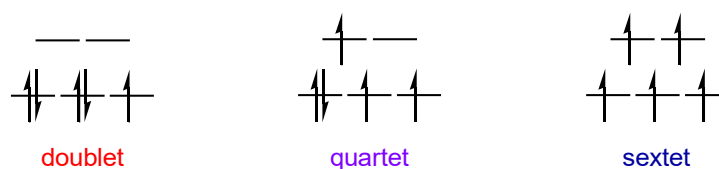


Figure 49. Photodissociation yields of N_2 (red traces) and $N_3\cdot$ (navy traces) dissociations from **1** as a function of temperature at 455, 530 and 600 nm. Total photodissociation yields are shown with purple traces.

We anticipated that the scaffold of iron(III) azide complex **1** is rigid enough to avoid any conformational isomerization caused by temperature changes. Hence, we considered that **1** could possibly undergo a thermal spin-crossover between two closely-lying spin isomers, each of which featured different absorption spectra, thus leading to different photodissociation outcomes. Iron(III) azide **1** is a d^5 electron complex with three possible electronic configurations of d orbitals: doublet (low spin), quartet (intermediate spin) and sextet (high spin, Scheme 6).



Scheme 6. Possible electronic configurations of d^5 complexes in an octahedral ligand field.

We performed multireference *ab initio* calculations using the CASPT2 method (complete active space perturbation theory) to determine the relative spin state energies. We found that doublet and sextet states are almost equal in energy (Table 2). Depending on whether the zero-point vibrational energy is included or not, the ground state of **1** is predicted to be either doublet or sextet; in each case, the energy difference is approximately 1 kcal mol⁻¹, which is in line with the generally accepted accuracy of theoretical methods. The remaining quartet spin state is more than 25 kcal mol⁻¹ higher in relative energy and was therefore discarded for any further considerations.

Table 2. Relative electronic energies ($E_{\text{rel}}^{\text{tot}}$) and relative energies at 0 K including zero-point vibrational energies ($E_{\text{rel}}^{0\text{K}}$) of spin isomers of **1** calculated using the CASPT2(11,15) method and geometries optimized at the B3LYP-D3/6-311++G** level.^(d)

spin state	$E_{\text{rel}}^{\text{tot}}$ [kcal mol ⁻¹]	$E_{\text{rel}}^{0\text{K}}$ [kcal mol ⁻¹]
double	0.0 ^(a)	1.0 ^(a)
quartet	26.3 ^(b)	25.8 ^(b)
sextet	1.4 ^(c)	0.0 ^(c)

(a) Contribution of the dominant electronic configuration is 85%.

(b) Contribution of the dominant electronic configuration is 69%.

(c) Contribution of the dominant electronic configuration is 92%.

(d) CASPT2 calculations were performed by Martin Srnec, DFT calculations were performed by Erik Andris.

Furthermore, we performed TD-DFT calculations for the doublet and sextet spin isomers of **1**, which provided the corresponding theoretical vis spectra (Figure 48c). Based on TD-DFT results, the electronic excitations, both in doublet and sextet states, are mainly of ligand-to-metal charge transfer character between the azide ligand and the iron center. Notably, the doublet state theoretical spectrum reproduced the photodissociation spectra of **1** in which N₂ dissociated (*cf.* Figure 48a and 48c, red traces), whereas the sextet state theoretical spectrum reproduced the photodissociation spectra of **1** in which N₃[·] was lost (*cf.* Figure 48a and 48c, blue traces).

Lastly, by combining experimental and theoretical evidence, we concluded that iron(III) azide **1** features two spin states, which are close in energy and account for the thermal spin crossover. At low temperatures (3 K), only the doublet spin state is populated; in contrast, at ambient temperatures (310 K), both doublet and sextet spin

states are populated. In addition, interconversion between doublet and sextet spin states explains the photochemistry of **1**: the former dissociates N_2 concomitant with iron(III) photooxidation to iron(V), whereas the latter dissociates $N_3\cdot$ accompanied by iron(III) photoreduction to iron(II).

5.2.3 CORROBORATION OF THE SPIN CROSSOVER OF **1** BY INFRARED SPECTROSCOPY

With exception of the photodissociation experiments in visible range, we routinely use our ISORI instrument to study ions by helium-tagging infrared photodissociation (IRPD) spectroscopy. In this context, we wondered whether we could use our experimental setup to provide further evidence for the spin crossover observed in **1** by acquiring infrared spectra at 3 and 300 K. However, experiments at 300 K generally require the absorption of many infrared photons to trigger photodissociation; that is, multiphoton infrared photodissociation experiments with powerful free electron lasers, which are only available in a limited number of facilities, thereby preventing us from conducting these experiments (Chapter 3.4).

Despite the theoretically insufficient power of our infrared laser system, which might hamper our experiments at 300 K, we initially measured a helium-tagging IRPD spectrum of **1** at 3 K (Figure 50a) to use it as a reference for laser alignment and spectra at 300 K. The spectrum at 3 K showed two intense absorption bands of the azido ligand, an antisymmetric stretch (ν_{asym}) at 2016 cm^{-1} and a symmetric stretch (ν_{sym}) at 1199 cm^{-1} . We confirmed the assignment of these azide vibrations by ^{15}N isotope labeling of the azido ligand in **1** using an equimolar mixture of $[(\text{MePy}_2\text{TACN})\text{Fe}-(^{15}\text{NNN})]^{2+}$ and $[(\text{MePy}_2\text{TACN})\text{Fe}-(\text{NN}^{15}\text{N})]^{2+}$ instead of unlabeled **1** (Figure 50a, grey trace). Upon labeling, both azide stretching vibration bands divided into two red-shifted bands, ν_{asym} and ν_{sym} emerged at 2013 and 1991 cm^{-1} , and at 1187 and 1170 cm^{-1} , respectively. As expected, the IRPD spectrum of **1** measured at 3 K agreed well with the IR spectrum theoretically predicted for the doublet spin state (Figure 50c).

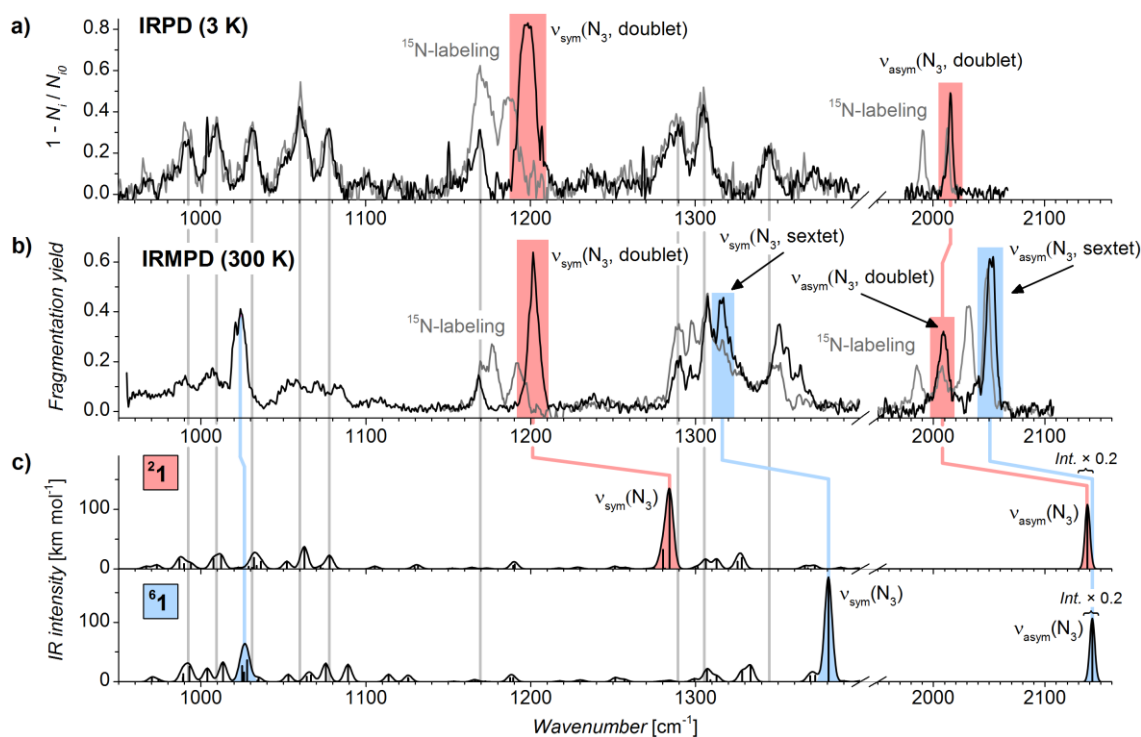


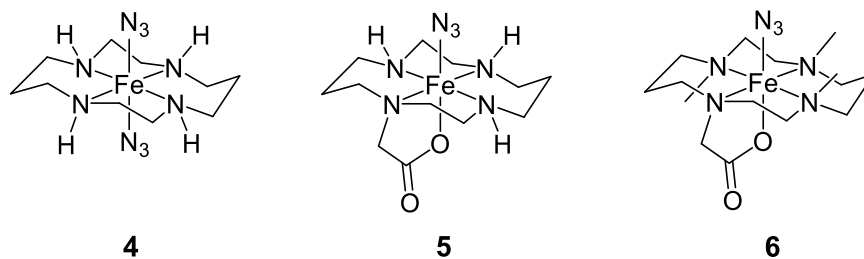
Figure 50. (a) Helium-tagging IRPD spectrum of **1** measured at 3 K. (b) IRMPD spectrum of **1** measured at 300 K acquired by monitoring the dissociation of N₂. Gray traces in both spectra correspond to unsymmetrical ¹⁵N-labeling of one of the azido nitrogen atoms in **1**, [(MePy₂TACN)Fe-(¹⁵N=N=N)]²⁺ and [(MePy₂TACN)Fe-(N=N=¹⁵N)]²⁺. (c) Theoretical IR spectra predictions for the doublet and sextet spin states of **1** calculated at the B3LYP-D3/6-311++G** level.

Despite the limited power output of our infrared laser system and technical difficulties associated with high-temperature laser beam alignment, we successfully recorded IRMPD spectrum of **1** at 300 K (Figure 50b) by monitoring N₂ dissociation, which is the lowest energy dissociation channel for both doublet and sextet spin states. The IRMPD spectrum of **1** displays two antisymmetric azide stretches (ν_{asym}), one located at 2016 cm⁻¹ in the IRPD spectrum shifted to 2009 cm⁻¹ and another band at 2052 cm⁻¹. Similarly, we observed changes in symmetric azide stretches (ν_{sym}); the vibration present at 1199 cm⁻¹ in the IRPD spectrum shifted to 1201 cm⁻¹, and a new band emerged at 1316 cm⁻¹. The presence of two sets of ν_{asym} and ν_{sym} bands suggests that the IRMPD spectrum at 300 K combines spectral features of two iron azide species, such as doublet and sextet **1**. Further evidence, supporting the presence of two spin states at 300 K, emerged from theoretical calculations, which showed that

antisymmetric azide stretches vibrate at comparable frequencies (2009 and 2052 cm^{-1}), regardless of the spin state of complex **1**. Furthermore, the calculations correctly predicted that the ν_{sym} of the sextet spin state is approximately 100 cm^{-1} higher in frequency than the ν_{sym} of the doublet spin state (1201 vs. 1316 cm^{-1}). Lastly, only the prediction for the sextet state accounted for the vibration at 1024 cm^{-1} , which we detected in the IRMPD spectrum at 300 K. Although our DFT calculations successfully predicted the relative frequencies of and trends in ν_{asym} and ν_{sym} azide vibrations upon spin state change, they failed to provide the absolute values of experimental ν_{asym} and ν_{sym} frequencies. Nevertheless, we unequivocally assigned all azide vibrations by ^{15}N -labeling. Hence, our IRPD and IRMPD experiments further corroborate the thermal spin crossover event in iron(III) azide **1**, in line with our previous photodissociation experiments (Chapter 5.2.2).

5.2.4 INVESTIGATION OF THERMAL SPIN CROSSOVER IN OTHER IRON(III) AZIDES

After characterizing the spin crossover event in **1**, we speculated whether other pseudooctahedral iron(III) azide complexes also feature a similar behavior. For the purposes of this study, we selected and synthesized three previously reported pseudooctahedral azide complexes based on the cyclam ligand (Scheme 5), *trans*-[(cyclam)Fe(N₃)₂]⁺ (**4**, cyclam = 1,4,8,11-tetraazacyclotetradecane),¹²⁸ [(cyclam-ac)Fe(N₃)₂]⁺ (**5**, cyclam-ac = 1,4,8,11-tetraazacyclotetradecane-1-acetate)¹²⁹ and [(Me₃cyclam-ac)Fe(N₃)₂]⁺ (**6**, Me₃cyclam-ac = 4,8,11-trimethyl-1,4,8,11-tetraazacyclo-tetradecane-1-acetate),¹³⁰ and investigated them by temperature-dependent photodissociation spectroscopy.



Scheme 7. Cyclam ligand-based iron(III) azide complexes.

First, we examined iron azide **4**, which exhibits a doublet ground state. Complex **4** has already been the object of several photodissociation studies focused on photo-

oxidation and generation of the corresponding iron(V) nitride. Indeed, at 4 or 77 K in a frozen acetonitrile matrix, the irradiation of **4** with a mercury arc lamp or with a 419-nm light provided considerable amounts of the desired photooxidation product.¹²⁸ However, interesting results have been observed in time-resolved Fourier transform IR experiments in acetonitrile solution at room temperature with 532-, 355- and 266-nm lasers used for irradiation.¹⁸⁸ In contrast to the report in frozen acetonitrile, photolysis in the visible range (532 nm) provided no evidence of photooxidation in acetonitrile solution. Instead, photooxidation was only achieved by 266- and 355-nm irradiation, albeit less efficiently in the latter. The only identified photoproduct using 532-nm irradiation was N_3^- , which resulted from a redox-neutral process. Moreover, dissociation to N_3^- became increasingly less efficient with the decrease in irradiation wavelength.

In the gas phase, **4** features more dissociation channels than **1**; aside from expected N_2 and $\text{N}_3\cdot$ dissociations (Figure 51, red and navy traces), we observed HN_3 (cyan trace) and a combined HN_3 and N_2 (wine trace) losses. The former represents a redox-neutral process because the oxidation state of iron remains the same. Analogously, the N_3^- loss is a redox-neutral process in the condensed phase (Chapter 5.2.1). Formally, simultaneous HN_3 and N_2 dissociation is a combination of photooxidation and redox-neutral processes.

The comparison of PD spectra acquired at 3 and 300 K shows that dissociation at ambient temperature mostly consisted of $\text{N}_3\cdot$ and HN_3 dissociation channels (absorption maxima at 485 and 512 nm, respectively), whereas the intensity of the former decreased at low temperature. At 3 K, HN_3 loss remained the dominant process, and the intensity of photooxidation processes (N_2 and combined HN_3 and N_2 losses, with absorption maxima at 512 and 495 nm, respectively) increased, as observed in azide **1**. We also performed TD-DFT calculations of electronic spectra of **4**; however, in this case, TD-DFT predictions were insufficiently accurate, especially regarding the positions of absorption maxima. Nevertheless, such TD-DFT inaccuracies are expected, particularly when predicting electronic transitions, which involve ligand-to-metal charge transfer (LMCT), *i.e.*, N_3^- -to-Fe in the case of **4**.¹⁹⁰ Lastly, we note that the absorption maximum of **4** obtained in our experiments is slightly red-shifted in relation to the absorption maximum of 4.ClO_4 measured in acetonitrile solution, which was reported at 487 nm.¹⁸⁸

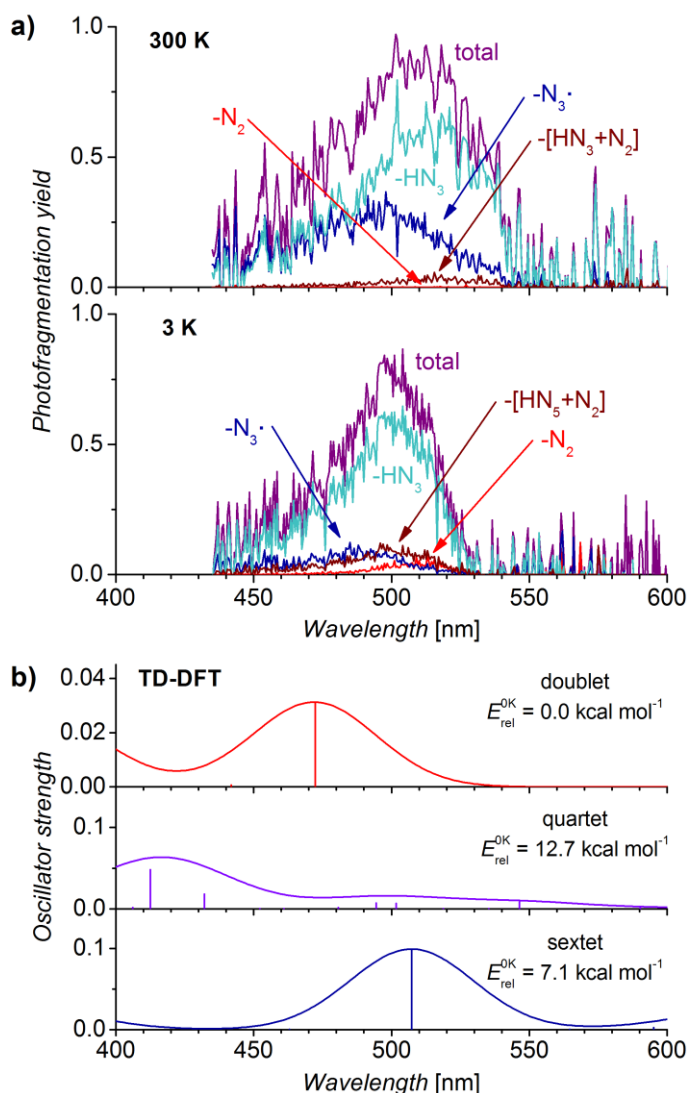


Figure 51. (a) Photodissociation spectra of $[(\text{cyclam})\text{Fe}(\text{N}_3)_2]^+$ (**4**) measured at 300 and 3 K. Each color trace corresponds to a specified photofragmentation channel. (b) TD-DFT electronic spectra of doublet, quartet and sextet spin states of **4**, including relative energies at 0 K with ZPE correction calculated at the B3LYP-D3/6-311+G** level.

Similarly to **1**, we measured temperature-dependent photodissociation yields of **4** at selected absorption maxima (485 and 512 nm) and monitored four dissociation channels: N_2 , $\text{N}_3\cdot$, HN_3 and combined HN_3 and N_2 losses (Figure 52). The decrease in temperature increased the yields of all dissociation channels, except for the loss of $\text{N}_3\cdot$ (navy trace), which decreased with temperature, especially at 512 nm (Figure 52b,d). The analysis of the temperature effect on photooxidation (N_2 , and HN_3 and N_2 dissociations) and photoreduction processes shows that **4** features the same

photochemistry as **1**, with a thermal spin crossover event between their doublet ground and sextet states (Figure 52c,d).

Lastly, we compared our results from the analysis of **4** in the gas phase with those from previous studies on **4** in the condensed phase. Our findings corroborate the study of **4** performed at 77 K,¹²⁸ in which lower temperature also favored photooxidation, and previous time-resolved experiments conducted at room temperature,¹⁸⁸ which identified redox-neutral N_3^- loss (HN_3 in our case). However, our results showed that photooxidation occurs at wavelengths as long as *ca.* 530 nm, in contrast to time-resolved experiments, in which no photooxidation was detected using irradiation in the visible range. We concluded that this discrepancy most likely derives from the different experimental conditions, *i.e.*, condensed vs. gas phase.

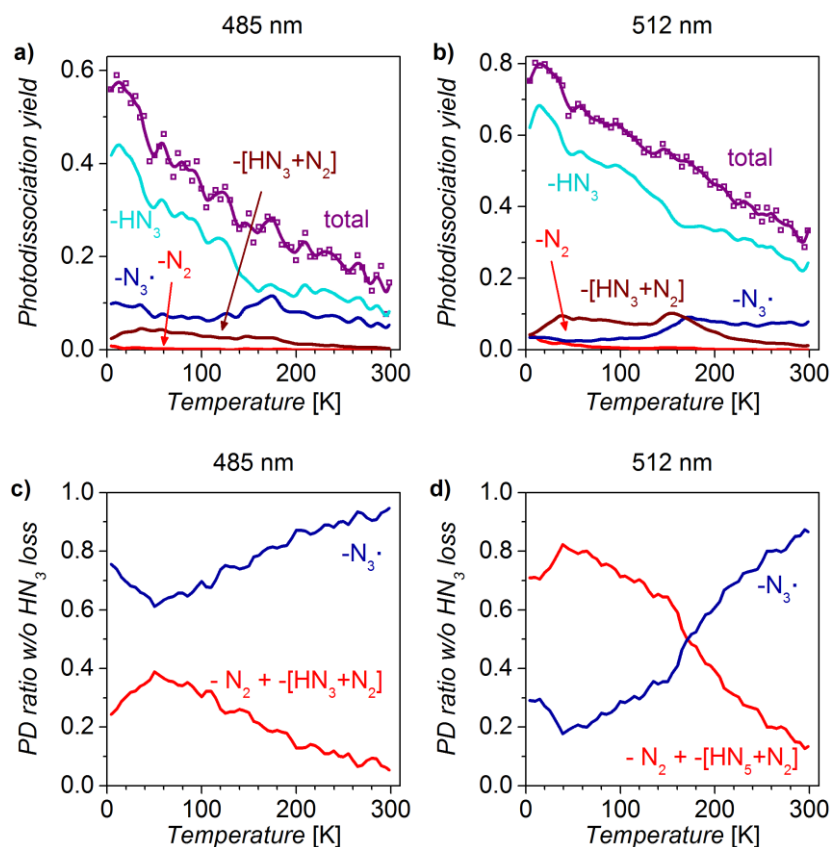


Figure 52. Temperature-dependent photodissociation of **4** measured at absorption maxima recorded for N_2 (a, 485 nm) and N_3^\cdot (b, 512 nm) losses (*cf.* Figure 51).

Subsequently, we investigated the photodissociation of **5**, which exhibits a doublet ground state, similarly to complexes **1** and **4**. Iron azide **5** has been studied in frozen acetonitrile matrix cooled to 77 K. The excitation of its LMCT band

(absorption maximum at 459 nm) with a 419-nm light provided a photooxidation product in 80% yield, whereas photolysis in acetonitrile solution resulted only in photo-reduction.¹²⁹ In contrast, time-resolved experiments performed at ambient temperature in acetonitrile solution demonstrated that LMCT band excitation with a 450-nm laser led to only redox-neutral process producing N_3^- . Irradiation with a 300-nm laser yielded photoreduction (N_3^- loss) and redox-neutral products, whereas the desired photo-oxidation (N_2 loss) was achieved only when under irradiation with a 266-nm laser.

In the gas phase, the photodissociation spectra of complex **5** feature all three possible dissociation outcomes (Figure 53), namely photooxidation (N_2 loss), photoreduction (N_3^- loss) and redox-neutral dissociation (HN_3 loss). At 300 K, these three processes equally contributed to the overall photodissociation yield. However, at 3 K, the N_2 dissociation intensity significantly increased, demonstrating a similar temperature effect to **1** and **4**. We further confirmed this observation by measuring the temperature effect on the photodissociation yield between 3 and 300 K at 460 and 485 nm (Figure 54a,b), which shows a clear increase in total and N_2 dissociation yields with the decrease in temperature. Plotting N_2 and N_3^- yields as a function of temperature (Figure 54c,d) indicates that complex **5** also undergoes thermal spin crossover between doublet and sextet states and that the former leads to photooxidation, producing the corresponding iron(V) nitride.

In comparison with previous studies of **5**, we showed that even visible light is suitable for dissociating N_2 in the gas phase, in contrast to experiments performed in liquid acetonitrile. Similarly to frozen matrix experiments, our experiments also demonstrated that lowering the experimental temperature, at which the photolysis is performed, enhances the photooxidation efficiency.

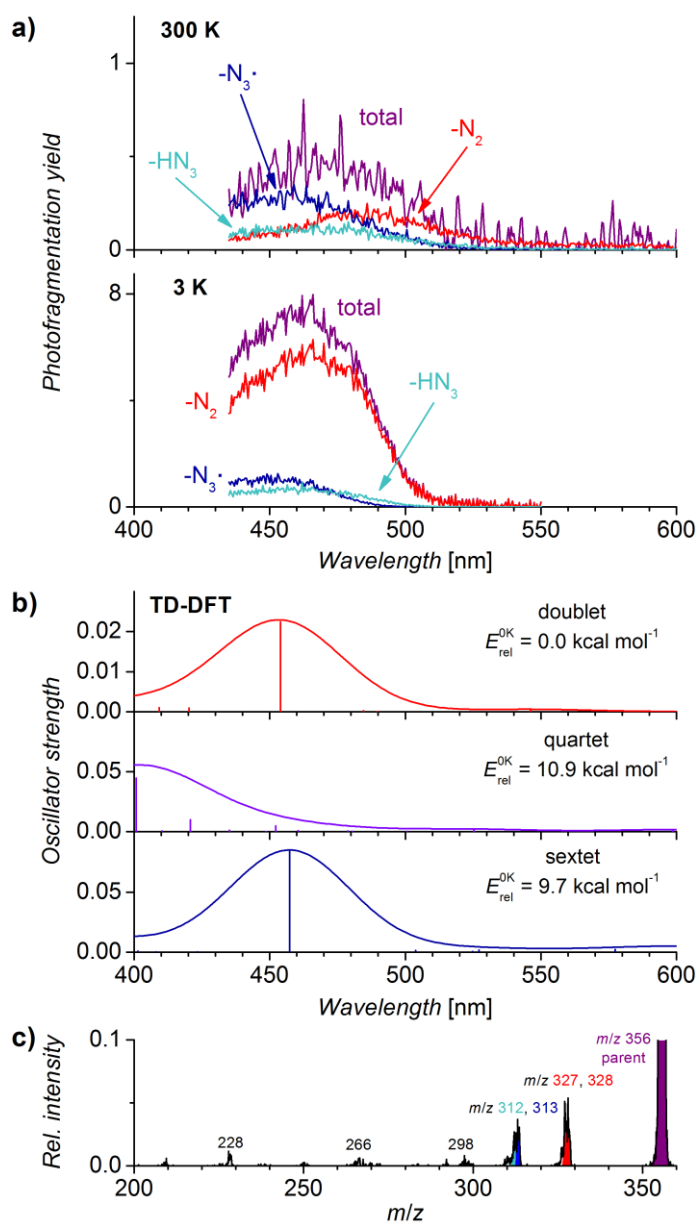


Figure 53. (a) Photodissociation spectra of $[(\text{cyclam-ac})\text{Fe}(1\text{-}^{15}\text{N}_3)]^+$ (**5**, one of the nitrogen atoms in azide ligand was ^{15}N -labeled) measured at 300 and 3 K. Each color trace corresponds to a specified photofragmentation channel. (b) TD-DFT electronic spectra of doublet, quartet and sextet spin states of **5**, including relative energies at 0 K with ZPE corrections calculated at the B3LYP-D3/6-311+G** level. (c) Photodissociation mass spectrum showing losses of N_2 , $\text{N}_3\cdot$, HN_3 and other fragmentation channels.

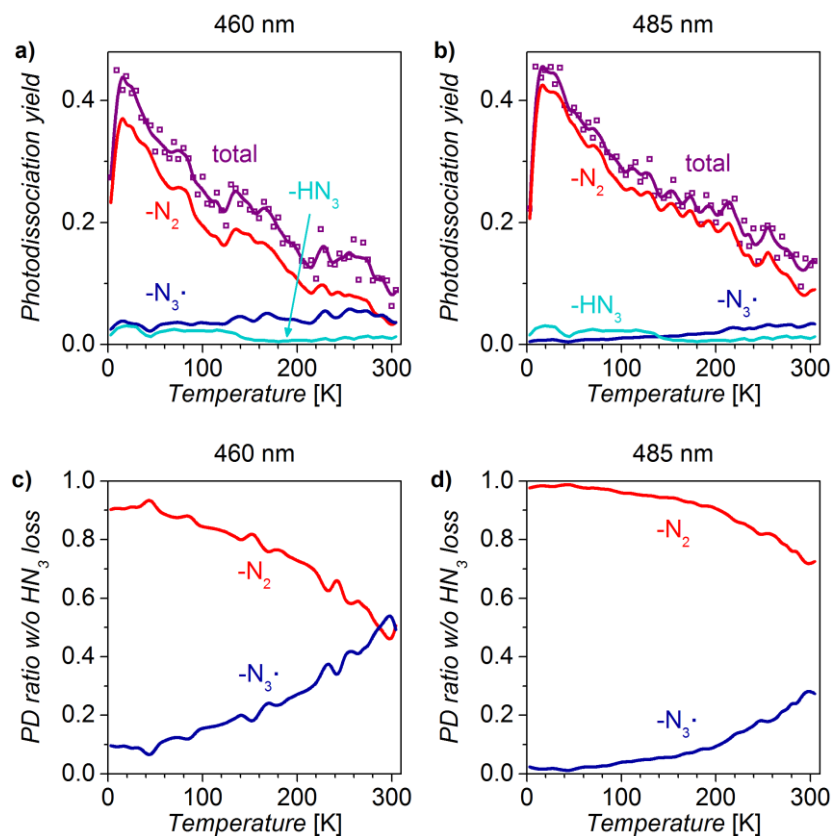


Figure 54. Temperature-dependent photodissociation of **5** measured at absorption maxima of N_2 (a, 485 nm) and $N_3\cdot$ (b, 460 nm) losses (*cf.* Figure 53).

Lastly, we studied azide **6**, a structurally related derivate of complex **5** (N–methyl vs. N–H groups); however, unlike **5**, complex **6** adopts a sextet ground state. The photochemistry of **6** has also been previously investigated in other studies, which showed that photolysis leads to photoreduction regardless of experimental conditions, *i.e.*, excitation wavelength, frozen or liquid solution.^{186,189} Hence, we were interested in assessing whether or not we would be able to detect any appreciable photooxidation of **6**.

Indeed, the photodissociation of **6** is almost exclusively dominated by photoreduction, yielding iron(II) complex and $N_3\cdot$ (Figure 55). Nevertheless, we also detected photooxidation (N_2 loss) and redox-neutral processes (MeN_3 loss), albeit at very low intensities, at 300 K. At 3 K, the photoreduction of **6** was even more dominant, with only trace amounts of photooxidation and redox-neutral products.

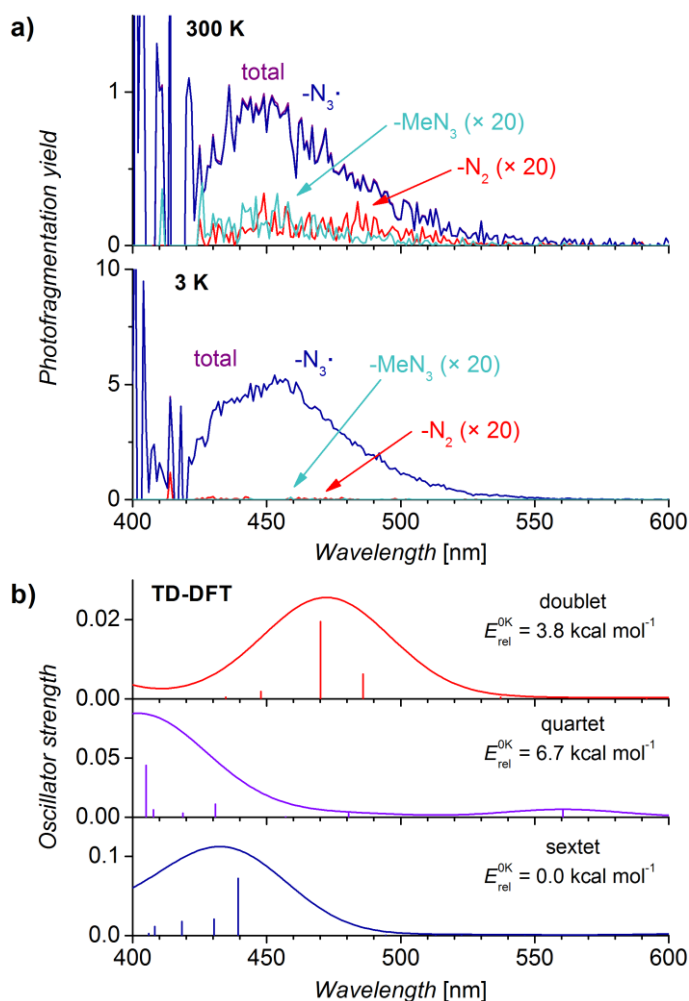


Figure 55. (a) Photodissociation spectra of $[(\text{Me}_3\text{cyclam-ac})\text{Fe}(\text{N}_3)]^+$ (**6**) measured at 300 and 3 K. Each colored trace corresponds to a specified photofragmentation channel. Note that, below 425 nm, the PD signal is biased by low power output of the laser and low PD yield. (b) TD-DFT electronic spectra of doublet, quartet and sextet spin states of **6**, including relative energies at 0 K with ZPE correction calculated at the B3LYP-D3/6-311+G** level.

Figure 56a and 56b display the variation of the photodissociation yield as a function of temperature measured from 3 to 240 K at 445 and 490 nm, which demonstrates the inefficiency of **6** in photodissociating N_2 and in producing the desired iron(V) nitride. The comparison between N_2 and $\text{N}_3\cdot$ PD yields shows that photo-oxidation is more effective at higher temperatures (Figure 56c,d), in contrast to our results from photodissociation experiments of azides **1**, **4** and **5**. However, **1**, **4** and **5** adopt a doublet ground state that is more populated at low temperature and that dissociates N_2 . Hence, photooxidation of **1**, **4** and **5** to the corresponding iron(V)

nitrides is more efficient at low temperatures. Conversely, complex **6**, which features a sextet ground state, exhibits the opposite trend of photooxidation/photoreduction as a function of temperature because the doublet state, which leads to photooxidation, is populated only at higher temperatures. Furthermore, the population of the doublet state of **6** is very small, even at ambient temperatures, which renders the photooxidation process nearly undetectable. Thus, our results agree with previous photodissociation studies and confirm that **6** is an unsuitable precursor for the corresponding photooxidation product, irrespective of method and experimental conditions used.

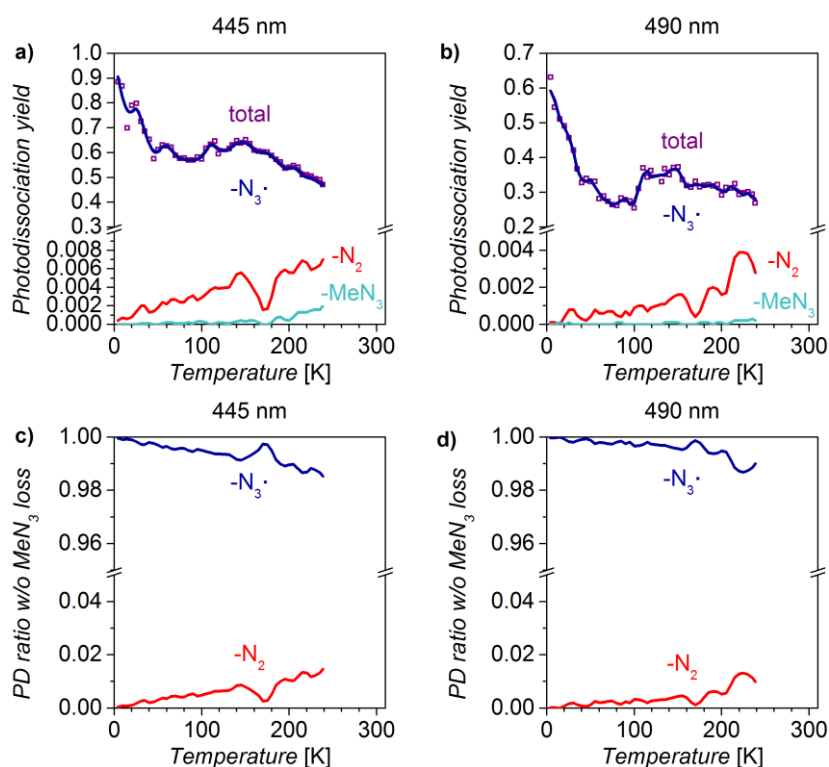


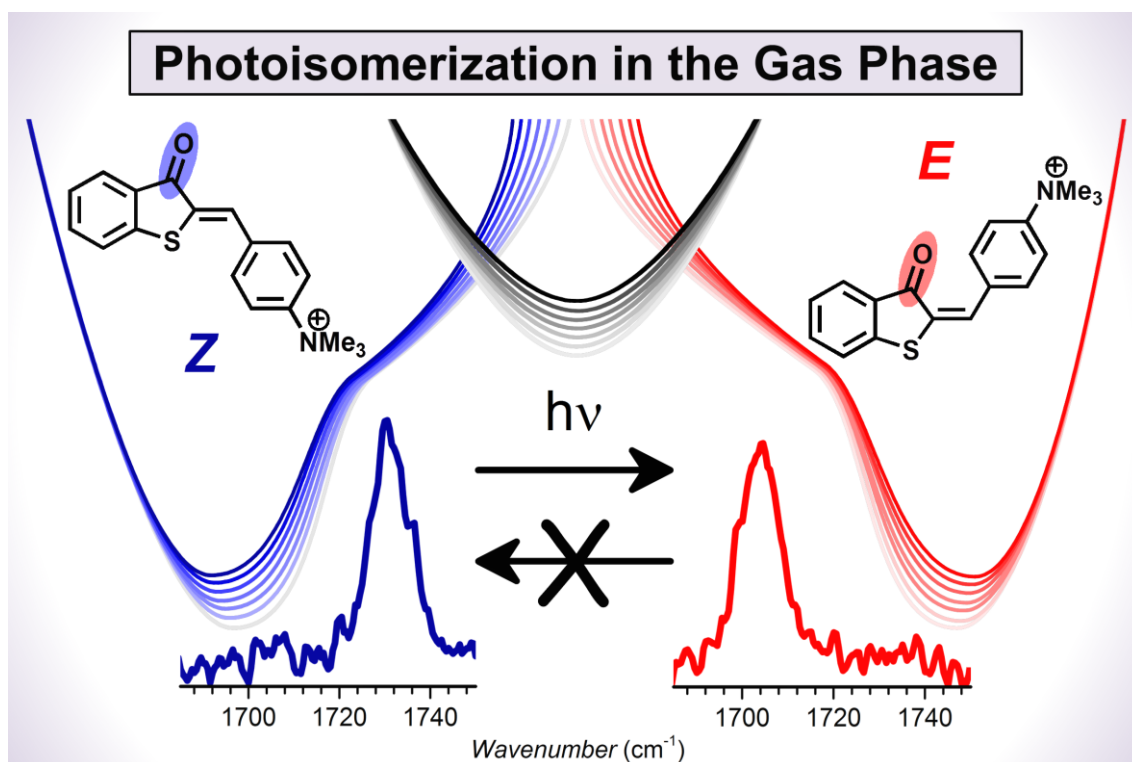
Figure 56. Temperature-dependent photodissociation of **6** measured at 445 and 490 nm (*cf.* Figure 55).

Finally, we attempted to further confirm our conclusions that iron(III) azide **4**, **5** and **6** undergo thermal spin crossover by IRDP and IRMPD experiments. Similarly to **1**, we expected to detect one set of azide vibrations (ν_{asym} and ν_{sym}) at 3 K and two sets of those vibrations at 300 K. However, we failed to obtain conclusive data at 300 K, most likely because of the multiphoton nature of IRMPD experiments, in which some vibrations have been can, in principle, be completely absent from a spectrum.¹⁹¹

5.2.5 CONCLUSION

Gas-phase temperature-dependent photodissociation experiments allowed us to examine and rationalize the photochemistry of pseudooctahedral iron(III) azides. These species adopt two, thermally interconverting, electronic spin states: doublet and sextet. As expected, the two spin states differ in their electronic and vibrational absorption spectra and in the results from their light-driven photodissociation. Photodissociation of doublet spin state iron(III) azides yields photooxidation products, that is, iron(V) nitrides, concomitantly with nitrogen release, whereas photodissociation of sextet spin state iron(III) azides yields photoreduction products, that is, iron(II) complexes, together with the azido radical. The former, more desired process is predominant at low temperature due to an increase in the portion of doublet ground state iron(III) azides under cryogenic conditions caused by the thermal spin-crossover event and *vice versa*. Moreover, photodissociation of some iron(III) azides also produces photo-neutral products, that is, iron(III) complexes and azide anion. Ultimately, these results demonstrate the power of ion spectroscopy in answering challenging chemical questions by eliminating experimental factors that often hamper studies on and the generation of reactive intermediates in solution, particularly those involved in transition metal-catalyzed and photochemical processes.

5.3 PHOTOISOMERIZATION OF HEMITHIOINDIGO MOLECULAR SWITCH IN THE GAS PHASE



This chapter is based on results reported in “Navrátil, R.; Wiedbrauk, S.; Jašík, J.; Dube, H.; Roithová, J. *Transforming hemithioindigo from a two-way to a one way molecular photoswitch by isolation in the gas phase. Phys. Chem. Chem. Phys.* **2018**, *20*, 6868–6876”.

5.3.1 INTRODUCTION

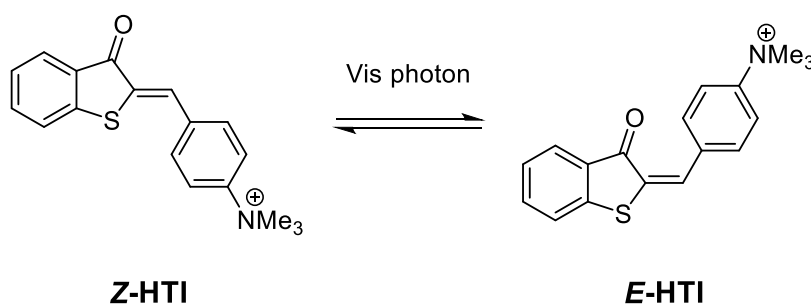
Hemithioindigo (HTI) compounds are emerging molecular photoswitches constructed by combining stilbene and thioindigo moieties connected through a C=C bond.¹⁹² Even though hemithioindigo compounds have already been known for several decades,¹⁹³ they have only recently attracted considerable research interest for their intriguing properties. HTI derivatives are easily prepared,^{194,195} feature thermal bistability and isomerize upon visible light activation of their central C=C bond.¹⁹² These properties have enabled their use in various fields of science, including supramolecular¹⁹⁶⁻¹⁹⁸ and surface chemistry,¹⁹⁹ molecular machinery,^{200,201} peptide^{202,203} and biological chemistry,²⁰⁴ and illustrate their potential for future applications.

HTI photoswitching is based on the isomerization of the central C=C bond and occurs between thermodynamically stable *Z* and metastable *E* isomers upon activation by a suitable visible light source. HTI photochemistry is rather complicated because *Z* and *E* isomers follow different deexcitation pathways along their excited potential energy surface, with many potential barriers, which control the overall photoswitching process.^{205,206} Quantum yields, typically 20%, combined with a favorable photochromism (each isomer has different absorption maxima), lead to efficient, visible light-driven and reversible photoswitching of HTIs with a high content of individual isomers in the photostationary state. The photoswitching efficiency can be improved, for instance, by replacing the stilbene moiety with a hydrogen bond donor, such as pyrrole.²⁰⁷ Quantum yields of HTI photoisomerization, which are typically moderate, are mostly affected by other nonreactive deexcitation pathways, such as fluorescence. However, fluorescence deexcitation is not always the major deexcitation pathway in HTI photoswitches. Another possibility is the formation of a twisted intramolecular charge transfer (TICT) state, which has been recently reported to occur upon excitation of several HTI derivatives.^{208,209} Deexcitation from the TICT state of HTI involves a rotation around the single C–C bond connecting the stilbene and the C=C bond moieties. Nevertheless, the formation of TICT states has only been observed in highly polar solvents, such as dimethylsulfoxide, which are able to stabilize the strongly zwitterionic character of TICT states.

In solution, HTI photoswitches and other molecular photoswitches in general have been well studied. However, our knowledge on photoswitching processes of isolated molecules in the gas phase remains limited. The group of Professor Evan Bieske

has reported several studies on photoisomerization in the gas phase by visible laser spectroscopy within the drift tube of an ion-mobility mass spectrometer.^{210,211} Recently, anion photoelectron spectroscopy has been used to investigate the electronic structure and dynamics of a molecular motor in the gas phase.²¹²

In recent years, the group of Dr. Henry Dube (LMU München, Germany) has actively researched HTI photoswitches and motors. In collaboration with us, they designed and synthesized a HTI derivative with a charged trimethylammonium group (Scheme 8) to enable our HTI photoswitching studies in the gas phase.



Scheme 8. Studied hemithioindigo photoswitch with a charged trimethylammonium group.

We envisioned that the combination of infrared and visible spectroscopies within our ISORI instrument would allow us to study HTI C=C bond isomerization in the gas phase. Furthermore, we hypothesized that we could use some vibrations as spectral markers of the overall photoisomerization process. Hence, this study describes our studies on the photoswitching process of two charged HTI isomers (Scheme 8, denoted as *Z*-HTI and *E*-HTI) in the gas phase.

5.3.2 RESULTS FROM THE CONDENSED PHASE

This chapter is based on the experiments performed by Dr. Sandra Wiedbrauk (LMU München).

In the condensed phase, the studied HTI contains iodide counterions. We structurally characterized both HTI isomers by X-ray crystallography (Figure 57) and by NMR and UV/vis spectroscopy.²¹³ Both *Z* and *E* HTI isomers exhibit molar extinction coefficients typical of HTI derivatives, that is, in the 5000–10000 L mol⁻¹ cm⁻¹ range, which we measured for absorption maxima in the

lower energy part of UV/vis spectra.²¹³ We observed moderate photochromism, typical of HTI derivatives. This photochromism allows efficient, two-way ($Z \rightarrow E$ and $E \rightarrow Z$) photoswitching. In contrast to most HTI photoswitches studied so far, we observed rather efficient fluorescence deexcitation in Z -HTI, whereas the opposite E isomer showed no detectable fluorescence. Therefore, we concluded that, most likely, fluorescence is not a deexcitation pathway competing with E -HTI photoisomerization in solution.

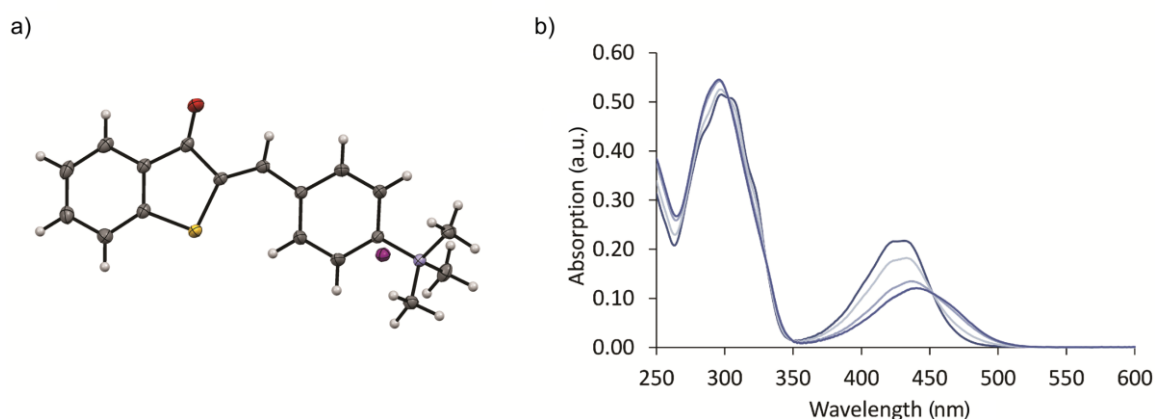


Figure 57. (a) X-ray structure of the Z -HTI iodide salt. (b) UV/vis spectra of methanolic solution of HTI recorded during the $Z \rightarrow E$ photoisomerization process. Isosbestic points are located at 331, 349 and 453 nm.

Figure 57 shows UV/vis absorption spectra recorded during $Z \rightarrow E$ photoisomerization triggered by 420 nm light in methanolic solution. The most prominent isosbestic points are located at 331, 349 and 453 nm. We established the isomer composition in the photostationary state (PSS) at different wavelengths by recording ^1H NMR spectra during photoisomerization. Irradiation at 420 nm results in 78% E -HTI in PSS, whereas irradiation at 505 nm yields 88% of Z -HTI in PSS.²¹³

Additionally, we observed that concentrated HTI samples started to decompose during irradiation in our NMR experiments, which already occurred after a single photoisomerization cycle. We presume that HTI decomposition most likely proceeds through a visible light-induced radical reaction involving trimethylammonium group demethylation, similarly to reports on light-initiated and oxygen-mediated dealkylation reactions of rhodamine²¹⁴ and toluidine blue²¹⁵ dyes.

Lastly, we investigated thermal $E \rightarrow Z$ isomerization in the absence of light in methanol, and we derived the energy barrier for such process (24.3 kcal mol⁻¹) by first-order kinetic analysis.²¹³

5.3.3 RESULTS FROM THE GAS PHASE – INFRARED SPECTROSCOPY

I started the investigation of HTI photoisomerization in the gas phase by transferring the studied HTI isomers to the gas phase by ESI of a methanolic solution of HTI. To transfer each HTI isomer to the gas phase, individually, I irradiated the syringe containing the methanolic solution of HTI with LED diodes (400 and 525 nm for E -HTI and Z -HTI, respectively) prior to ESI. Then, I acquired helium-tagging IRPD spectra of both isomers at 3 K. Note that, without syringe irradiation, I always obtained spectra of a corresponding mixture of HTI isomers.

Figure 58 shows helium-tagging IRPD spectra of Z -HTI (blue trace) and E -HTI (red trace). The main difference in IR spectra between these two isomers is the frequency of the carbonyl stretching vibration, $\nu(\text{C}=\text{O})$. Based on the comparison of DFT calculations at the B3LYP-GD3BJ/6-311++G** level, I assigned the experimental carbonyl stretch at 1704 cm⁻¹ to E -HTI and at 1730 cm⁻¹ to Z -HTI. The experimental frequency difference between these carbonyl vibrations (26 cm⁻¹) is somewhat smaller than the DFT-predicted difference (41 cm⁻¹). Otherwise, the IRPD spectra of both isomers share many similarities, as anticipated from their comparable structures and theoretical spectra. The overall match between experimental and theoretical IR spectra, including band intensities, is good, except for the C–H bending vibration ($\delta(\text{C}-\text{H})_{\text{C}=\text{C}}$) of the (C=C)–H moiety in E -HTI. Experimentally, the $\delta(\text{C}-\text{H})_{\text{C}=\text{C}}$ vibration is red-shifted to 1354 cm⁻¹ by 52 cm⁻¹ with respect to the theoretical frequency.

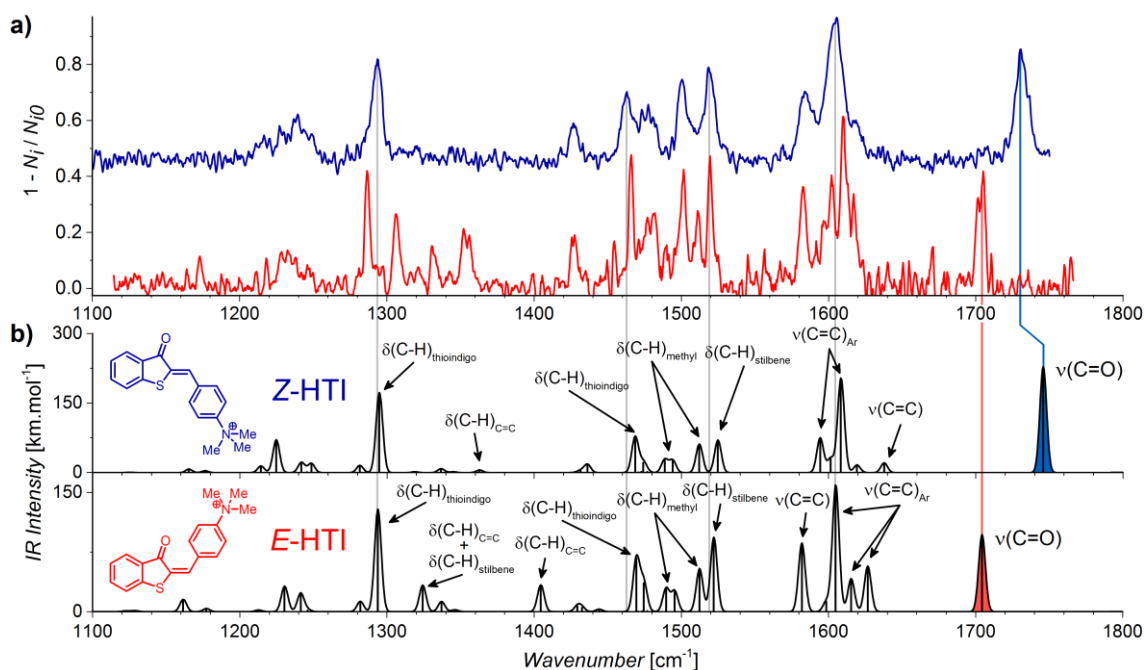


Figure 58. (a) Helium-tagging IRPD spectra of Z-HTI (blue trace, 0.45 y -axis offset) and E-HTI (red trace) measured at 3 K. The syringe containing the methanolic HTI solution was irradiated with 400- or 525-nm LED diodes prior to electrospray ionization to selectively obtain E-HTI or Z-HTI ions, respectively. (b) Theoretical infrared spectra calculated at the B3LYP-GD3BJ/6-311++G** level of theory; frequencies were scaled by 0.99.

5.3.4 RESULTS FROM THE GAS PHASE – ELECTRONIC SPECTROSCOPY

After recording IRPD spectra of individual HTI isomers, I proceeded to investigate their electronic absorption characteristics, which would eventually enable me to explore the HTI photoswitching process. Similarly to IRPD experiments, I also studied each isomer separately; for such purpose, I irradiated the HTI solution with LEDs prior to ESI (Chapter 5.3.3). I used two available experimental techniques to record electronic spectra of HTI isomers, that is, helium-tagging photodissociation and standard photodissociation, both in the visible spectra range. In the latter, I monitored the dissociation of the methyl radical from the trimethylammonium group, whose typical photodissociation yield was 1–2%.

Figure 59 shows helium-tagging (blue traces) and photodissociation (red traces) spectra of HTI isomers, which I measured at 3 K. The spectra of Z-HTI are vibrationally resolved with a strong 0–0 transition peaking at 446 nm (Figure 59a), which corresponds to 2.78 eV (268 kJ mol⁻¹) vertical excitation energy. Absorption below 420 nm

is very small or missing because the power of our laser system significantly decreases in that range.

I performed theoretical predictions of the Franck-Condon envelope. My initial attempts to optimize the geometry of the first singlet excited state at the B3LYP level failed. Therefore, I performed my calculation at the M06L-D3/def2TZVP level instead, which successfully provided excited state geometries, and the subsequent Franck-Condon prediction showed a good match with the experiment (Figure 59a, black trace). The positions and intensities of some bands are not precisely predicted, most likely due to inaccurate theoretical description of the vibrational modes, which are approximated by the harmonic potential.

Contrary to my expectations, the helium-tagging and photodissociation spectra of *E*-HTI feature a very broad absorption, which ranges from 420 to 495 nm (Figure 59b). The helium-tagging spectrum has low intensity, with no resolved features whatsoever. The photodissociation spectrum features two absorption maxima at positions of the two strongest bands of the *Z*-HTI (436 and 446 nm, *cf.* Figure 59a). Because the photodissociation is generally a multiphoton process, the absorption features of the *Z* isomer present in the photodissociation spectrum of *E* isomer most likely stem from sequential absorption of several photons, which eventually cause *E* → *Z* isomerization and subsequent photodissociation of *Z*-HTI. As a result, I detected spectral features of *Z*-HTI in the photodissociation spectrum of *E*-HTI. In addition, I ruled out any potential contamination of *E*-HTI with *Z*-HTI ions because that would be inconsistent with the helium-tagging IRPD spectrum of *E*-HTI (*cf.* Figure 58a, I detected no $\nu(\text{C}=\text{O})$ vibration of *Z*-HTI). These results together with the spectrum of *Z*-HTI, which exhibits higher intensity than *E*-HTI, suggest that the *Z* isomer has a higher extinction absorption coefficient, as observed in the condensed phase, where the extinction absorption coefficient of the *Z* isomer is approximately two times higher than that of the *E* isomer.²¹³ Therefore, even a small fraction of *Z*-HTI ions, formed by multiphoton isomerization from *E*-HTI, created intense absorption features at 436 and 446 nm in the photodissociation spectrum of *E*-HTI.

Conversely, multiphoton absorption cannot occur in helium-tagging experiments. Hence, the absorption of a single photon by *E*-HTI helium complexes already detaches the helium tag and generates a signal in the helium-tagging spectrum.

Accordingly, the helium-tagging spectrum of *E*-HTI contains no bands of the opposite isomer.

Even though the spectra of *E*-HTI are unresolved, I attempted to simulate the Franck-Condon envelope by DFT calculations. However, my DFT calculations predicted Franck-Condon factors with zero intensity due to significant geometry changes induced by the electronic excitation between the ground and excited states (Figure 62). Hence, such prediction is unreliable as stated in the Gaussian software package manual.

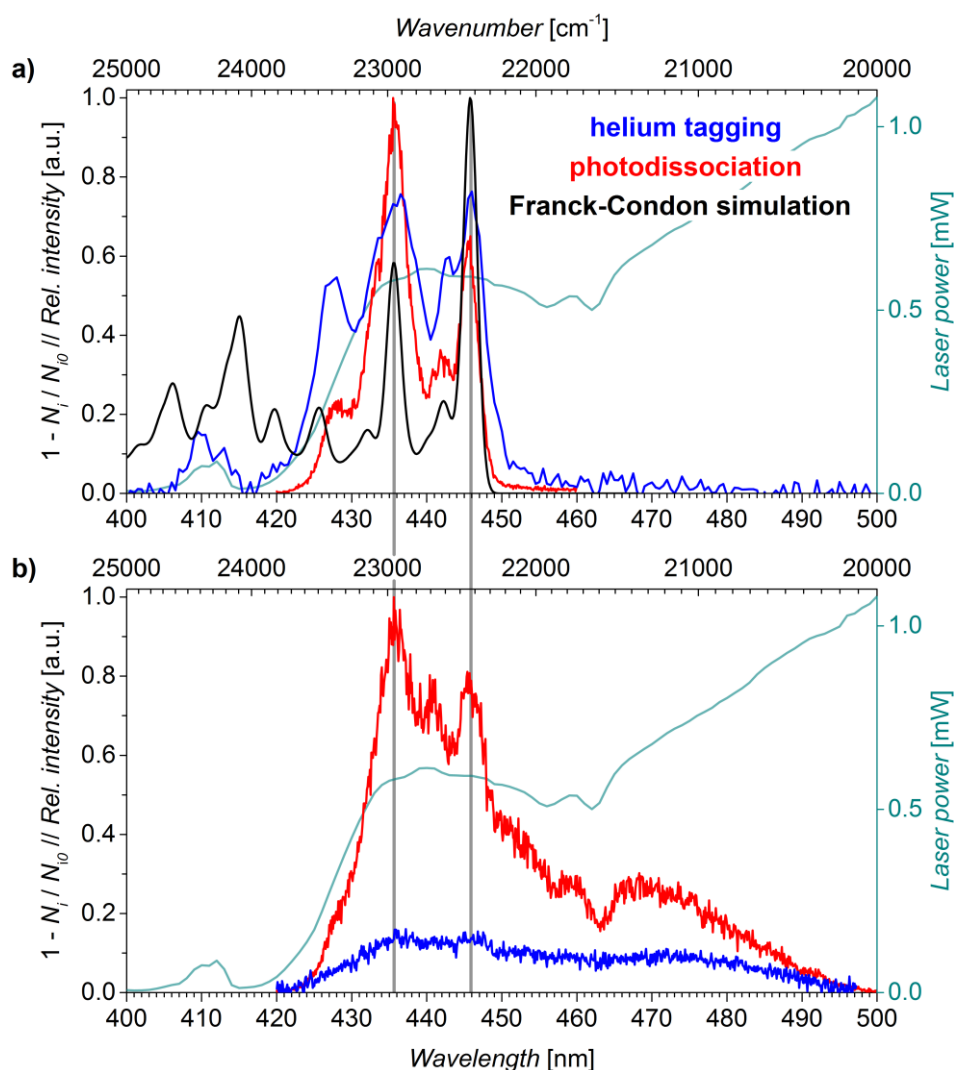


Figure 59. Visible absorption spectra of (a) *Z*-HTI and (b) *E*-HTI. Blue and red traces indicate the helium-tagging (fragmentation of $[\text{HTI}.\text{He}]^+$ monitored) and photodissociation (formation of fragments m/z 281 monitored) spectra, respectively. The *Z*-HTI Franck-Condon simulation was performed at an M06L-D3/def2TZVP level of theory (black trace).

5.3.5 HEMITHIOINDIGO PHOTOISOMERIZATION IN THE GAS PHASE

After determining absorption characteristics of both isomeric HTI ions, I studied their photoisomerization using the following experimental scheme: Initially, I trapped HTI ions in the ion trap at 3 K and then excited them using visible light irradiation for some time. Subsequently, I evaluated the result of electronic excitation by tagging the ions with helium, and I measured their IRPD spectrum. I chose the $\nu(\text{C}=\text{O})$ vibration as a suitable spectral marker, unequivocally indicating the photoisomerization outcome thanks to the distinct frequency of the $\nu(\text{C}=\text{O})$ vibration of each isomer.

First, I examined photoisomerization of *Z*-HTI ions. Upon irradiating *Z*-HTI ions with a 436-nm light in the ion trap at 3 K, the $\nu(\text{C}=\text{O})$ at 1730 cm^{-1} disappeared while a new band at 1704 cm^{-1} emerged, clearly showing virtually quantitative $Z \rightarrow E$ conversion (Figure 60a and 61). In addition to the altered frequency of the $\nu(\text{C}=\text{O})$ vibration, the helium-tagging IRPD spectrum changed completely (most apparently between $1300\text{--}1360\text{ cm}^{-1}$) and fully matched the IRPD spectrum of *E*-HTI (please compare red and gray traces in Figure 60a).

Surprisingly, when I sampled and subjected *E*-HTI ions to the same photoisomerization protocol (transfer to the gas phase and subsequent irradiation with visible light), I detected no changes in the infrared spectrum. Nevertheless, I tested various wavelengths available within the range of our visible laser (400–650 nm), and I also varied other experimental parameters, for instance, trapping conditions (number and duration of helium pulses, voltages applied to entrance and exit electrodes of the ion trap) and irradiation time, among others. However, regardless of the experimental conditions used, I was unable to detect any change in helium-tagging IRPD spectra after attempting photoisomerization.

Because the intensity of electronic absorption of *E*-HTI ions was rather weak (Figure 59b, blue trace), I presumed that the power output of our tunable visible laser might be insufficient to trigger detectable photoisomerization. Therefore, I irradiated *E*-HTI ions with a 462 nm laser diode with a 1.1 W power output focused into the ion trap. I chose this particular diode because the opposite *Z* isomer did not absorb at this wavelength. Nevertheless, even a significantly more powerful light failed to accomplish the desired $E \rightarrow Z$ photoisomerization in amounts, which would be observable in IRPD experiments.

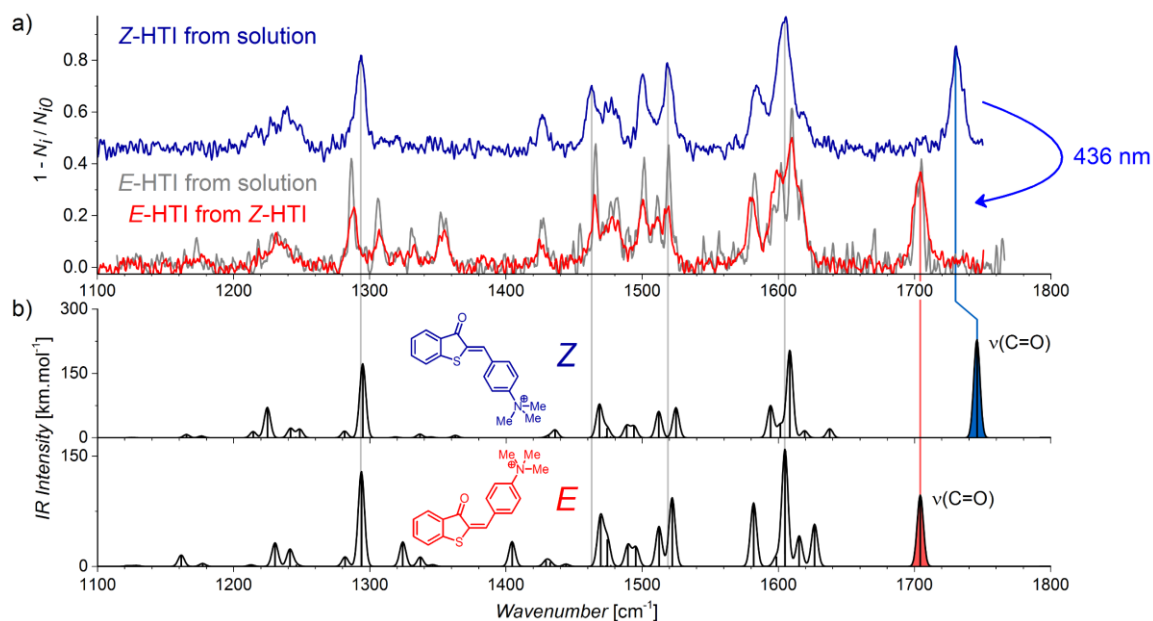


Figure 60. (a) The $Z \rightarrow E$ photoswitching process of Z-HTI. Blue trace corresponds to the spectrum of Z-HTI. Red trace corresponds to the spectrum of E-HTI ions that were formed upon 436-nm light irradiation of trapped Z-HTI ions in the ion trap at 3 K. Gray trace represents the spectrum of E-HTI for comparison, which was obtained in previous experiments (Figure 58). (b) Theoretical DFT spectra calculated at the B3LYP-GD3BJ/6-311++G** level of theory (frequencies were scaled by 0.99).

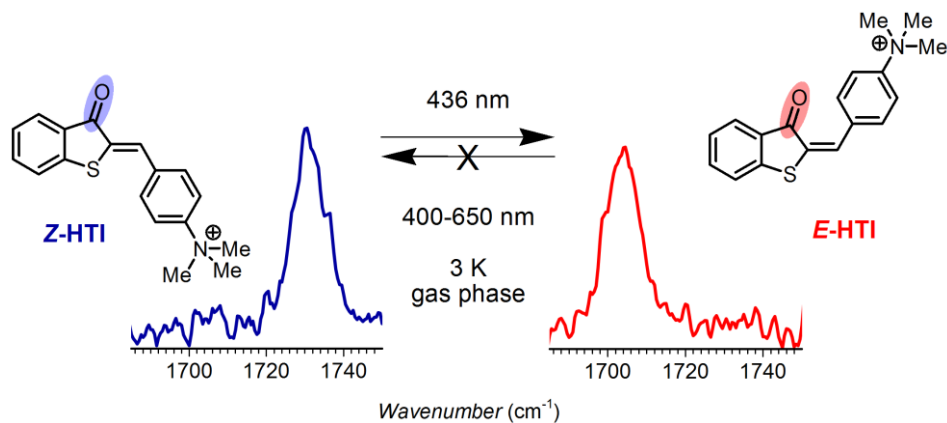


Figure 61. Details of the $\nu(\text{C}=\text{O})$ vibration region showing successful $Z \rightarrow E$ and failed $E \rightarrow Z$ photoisomerization of HTI, which was assessed by helium-tagging IRPD spectroscopy at 3 K. The measured $\nu(\text{C}=\text{O})$ vibration bands correspond to the highlighted C=O group in Z-HTI (blue) and E-HTI (red).

5.3.6 DISCUSSION

Thus far, my results have shown that *Z*-HTI ions readily and quantitatively photoisomerize in the gas phase. Conversely, the photodissociation spectrum of *E*-HTI (Figure 59b) suggests that a small part of ions might have undergone isomerization, but in amounts undetectable in subsequent IRPD experiments. Thus, the *E* → *Z* isomerization efficiency is on the order of tenths of percent at most. In this section, I comment on several factors and scenarios concerning *E*-HTI, its spectra and its inability to photoisomerize in the gas phase:

1. Photoexcited *E*-HTI ions might carry insufficient energy to overcome the energy barrier between S_1 and S_2 states, which is associated with photoisomerization. My assumption corroborates previous observation in solution,²¹⁶ which showed that electron withdrawing substituents on the stilbene fragment (trimethylammonium group in my case) increase the photoisomerization energy barrier by destabilizing the zwitterionic S_2 state. Intuitively, the S_2 state, which is involved in and responsible for photoisomerization of HTI switches, will be even more destabilized in absolutely non-polar gas-phase environment. Additionally, I considered the ability to overcome energy barriers, which is related to temperature in general. Previous studies have shown that the decrease in temperature completely impedes the photoisomerization of *E*-stilbenes.²¹⁷ Interestingly, the isomerization of *Z*-stilbenes remained intact. Because I performed experiments with HTIs at 3 K, I decided to conduct further experiments at a higher temperature to assess whether temperature would have an effect on photoisomerization. However, the *E* → *Z* isomerization remained suppressed even at 290 K. Therefore, I concluded that, most likely, temperature is not the factor that hinders *E*-HTI photoisomerization in the gas phase.

2. The helium-tagging spectrum of *E*-HTI (Figure 59b) features a broad, vibrationally unresolved band. This suggests that electronic excitation leads to considerable geometry changes. Indeed, my DFT calculations at the M06L-D3/def2TZVP level support this because S_0 and S_1 have different geometries (Figure 62). The major difference is the dihedral angle between thioindigo and stilbene planes, which changes from 0° to 27° upon $S_1 \leftarrow S_0$ transition. Furthermore, the dihedral (C=C)–(C–C)_{phenyl} angle changed by 18°, twisting the phenyl ring of the stilbene fragment. As expected, these geometry changes result in negligible Franck-Condon factors and in no resolution of the observed electronic transition. On the contrary, the *Z*-HTI (Figure 59a) undergoes

marginal geometry changes, and its spectra are well resolved. I confirmed this by DFT calculations, which showed that, for instance, the value of the S–C=C–H dihedral angle remains virtually unchanged upon excitation. Moreover, theoretical Franck-Condon predictions account for most features observed in the helium-tagging spectrum (Figure 59a, black trace); thus, I assigned the spectra of *Z*-HTI to the $S_1 \leftarrow S_0$ transition. Lastly, these results agree with earlier theoretical assessments of the HTI photoisomerization.²⁰⁵

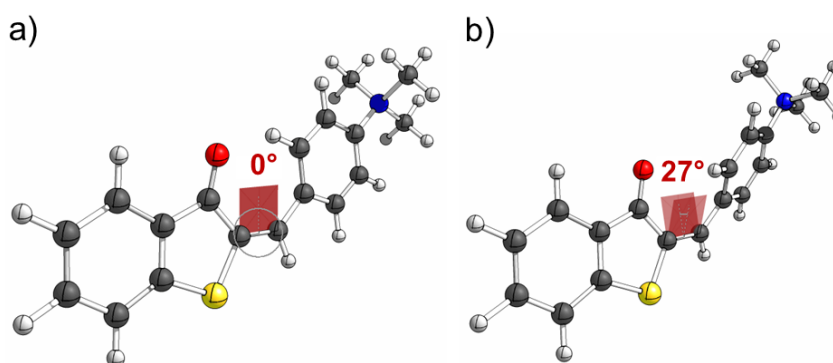


Figure 62. The optimized geometries of (a) S_0 and (b) S_1 states of *E*-HTI at the M06L-D3/def2TZVP level. The values of S–C=C–H dihedral angles are shown in red. Please note that the dihedral (C=C)–(C–C)_{phenyl} angle (between the C=C bond and the phenyl ring planes) of the S_1 state is 18° (not highlighted).

3. The $E \rightarrow Z$ isomerization might compete with a faster deexcitation pathway, such as fluorescence. Even though *Z*-HTI features sizable fluorescence quantum yields in methanolic solution (Chapter 5.3.2 and ref. 213), *E*-HTI fluorescence is negligible, at least in solution. Therefore, fluorescence deexcitation most likely inefficiently competes with photoisomerization. Furthermore, I considered a competing deexcitation involving TICT state.^{208,209} The TICT state in HTI compounds generally involves twisting of the phenyl ring along the (C=C)–(C–C)_{phenyl} dihedral angle, as observed in the S_1 optimized structure of *E*-HTI (Figure 62b). However, TICT states have only been observed in the photochemistry of *Z*-HTI compounds with strong electron donors and in highly polar solvents (Chapter 5.3.1). Hence, I excluded the possibility of the deexcitation of *E*-HTI through the TICT state in the gas phase.

4. The optimized S_1 and T_1 structures of *E*-HTI are rather similar, which may favor an intersystem crossing. The final deexcitation from T_1 to S_0 would be realized by phos-

phorrescence. The relaxation involving triplet states has already been reported in several *Z* hemithioindigo derivatives,²⁰⁵ yet we observed no long-lived phosphorescence in our HTIs studied in solution.²¹³ Nonetheless, HTI deexcitation might actually involve T_1 states, at least if several photons are absorbed as in photodissociation experiments (similarly to the photodissociation mechanism in Figure 5), which involved methyl radical dissociation. I performed DFT calculations to theoretically explain this radical process, and I found that the corresponding dissociation transition states feature, unsurprisingly, triplet multiplicity and that their energies are indeed experimentally accessible (Figure 63).

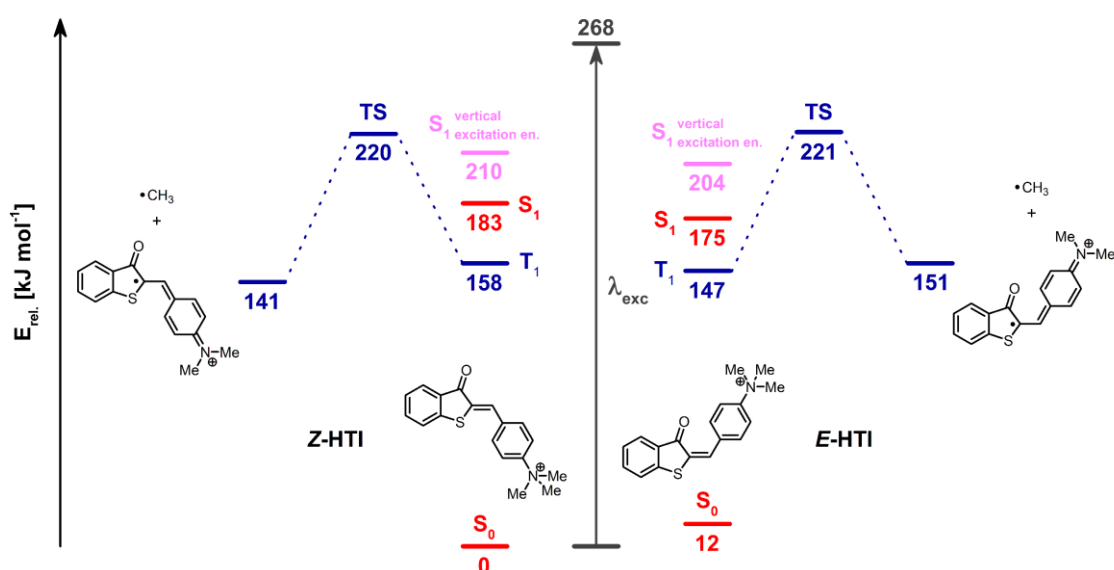


Figure 63. Calculated relative electronic energies of studied charged HTIs in their S_0 , S_1 and T_1 states at the M06L-D3/def2TZVP level of theory. Energies include ZPE corrections and are reported in kJ mol^{-1} . The grey arrow indicates the 0–0 transition energy of Z-HTI ($\lambda_{exc} = 446 \text{ nm}$). Transition states and resulting fragments (m/z 281, doublet multiplicity) from the loss of methyl radical (15 mass units) observed and used in photodissociation experiments are shown in navy blue.

5. In general, HTI photoisomerization quantum yields vary quite a lot between *Z* and *E* isomers, at least if no strong electron donors are present.²¹⁸ The *Z* isomer undergoes the photoisomerization much more efficiently than the *E* isomer, most likely due to the presence of a nonreactive deactivation channel – a seam of conical intersections, which directly and rapidly transfers excited *E* isomer back into its starting

configuration. The fact that nonreactive deexcitation outcompetes photoisomerization agrees with a very short excited state lifetime, which I deduced from the broadness of the electronic spectra of *E*-HTI. I proposed that this internal conversion could specifically result from an interaction between the carbonyl oxygen and the *ortho* hydrogen atom of the phenyl ring of the stilbene part (Figure 64, atoms highlighted in red). The distance between these atoms is 1.94 Å, based on DFT calculations, which is comparable with the length of the hydrogen bond in water, which is typically 1.97 Å. Moreover, this interaction will be strengthened by the lack of surrounding solvent molecules, which would normally interact with the carbonyl group and prevent the formation of C=O...H-C interactions in solution, and by the negative inductive effect of the trimethylammonium group.

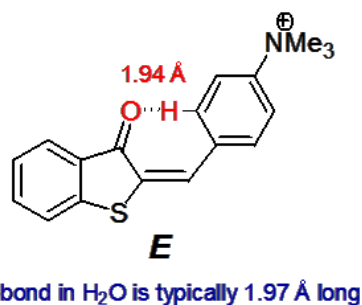


Figure 64. Close contact between highlighted carbonyl oxygen and aryl hydrogen in *E*-HTI. The molecule was optimized at the M06L-D3/def2TZVP level of theory.

Evidently, the inability of the studied HTI to undergo *E* → *Z* isomerization in gas phase stems from the absence of solvent molecules around the isolated ion. I presumed that the surrounding microenvironment of solvent molecules might play a key role in *E* → *Z* isomerization by reducing the dipole-dipole interaction of the *ortho* hydrogen atom of the stilbene part and the carbonyl oxygen. This interaction most likely enables the nonreactive deactivation of excited *E*-HTI back to its ground state.

5.3.7 HEMITHIOINDIGO COMPLEXES WITH BETAINE

In Chapter 3.5, I mentioned that ESI could be advantageously used for the formation of complexes between ions and solvent molecules. Ultimately, performing ion spectroscopy studies on these complexes can be used to bridge the gap between isolated ions in the gas phase and solvated molecules in solution. Because I assumed that

solvation of *E*-HTI ions could eventually enable photoisomerization, I investigated whether the mass spectrum of HTI contained some solvated ions. However, I observed only a weak signal corresponding to $[\text{HTI}\cdot\text{methanol}]^+$ complexes, regardless of ESI conditions. I also tried to generate hydrated HTI by adding water to a methanolic HTI solution; unfortunately, I detected no considerable amounts of hydrated HTI ions.

The Brøndsted Nielsen research group recently described an elegant approach for measuring photodissociation spectra in the gas phase (Chapter 3.5, Figure 16).¹¹³ The authors formed adducts of various ions with betaine zwitterion (*N,N,N*-trimethylglycine), which they added to the solution containing the analyte. The formation of these non-covalently bound adducts was enabled by a strong dipole-dipole interaction. Subsequently, the adducts were transferred to the gas phase by ESI and irradiated by vis laser. Finally, the single photon absorption led to betaine dissociation and generated a PD signal, similarly to the tagging process, but betaine dissociation was performed at ambient temperatures.

Thus, I assumed that the strong dipole moment of betaine zwitterion in the proximity of *E*-HTI could substitute the polar solvent environment and enable $E \rightarrow Z$ photoisomerization as a result. Furthermore, I assumed that *E*-HTI complexation could prolong the lifetime of its excited state, similarly to protonated tryptophan hydration (Figure 13), which would allow me to record vibrationally resolved spectra. Accordingly, I added betaine to the methanolic HTI solution and, gratifyingly, I observed an intense signal of $[\text{HTI}\cdot\text{betaine}]^+$ complexes in the mass spectrum. Similarly to my previous experiments, I irradiated the methanolic HTI and betaine solution with 400- or 525-nm LEDs prior to ESI to isolate an individual HTI isomer.

First, I measured absorption spectra of betaine complexes in the visible range. Figure 65 shows helium-tagging and photodissociation spectra of betaine complexes (navy and red traces, respectively), both at 3 K. In the former, I monitored the dissociation of the helium tag from $[\text{HTI}\cdot\text{betaine}\cdot\text{He}]^+$ complexes, and in the latter, I monitored dissociation of betaine zwitterion from $[\text{HTI}\cdot\text{betaine}]^+$ complexes. Interestingly, the helium-tagging spectrum of *Z*-HTI betaine complex in Figure 65a exhibits a lower intensity than the spectrum of *Z*-HTI (*cf.* Figure 59a). The absorption maxima are blue-shifted by several nanometers, thus indicating that the recorded electronic transition displays a charge-transfer character, as suggested from observations in other betaine complexes.¹¹³ Moreover, the shifts are indicative of a decreased degree of conjugation

and of a reduced donor-acceptor character of the central C=C bond stemming from the enhanced electron deficiency of the stilbene fragment, which is caused by coordination of the carboxylate of betaine to the positively charged trimethylammonium group. Furthermore, the extinction coefficient and hence the spectral intensity are lowered, for the same reasons. Similar substitution effects on photophysical properties of HTI derivatives have been previously described.¹⁹²

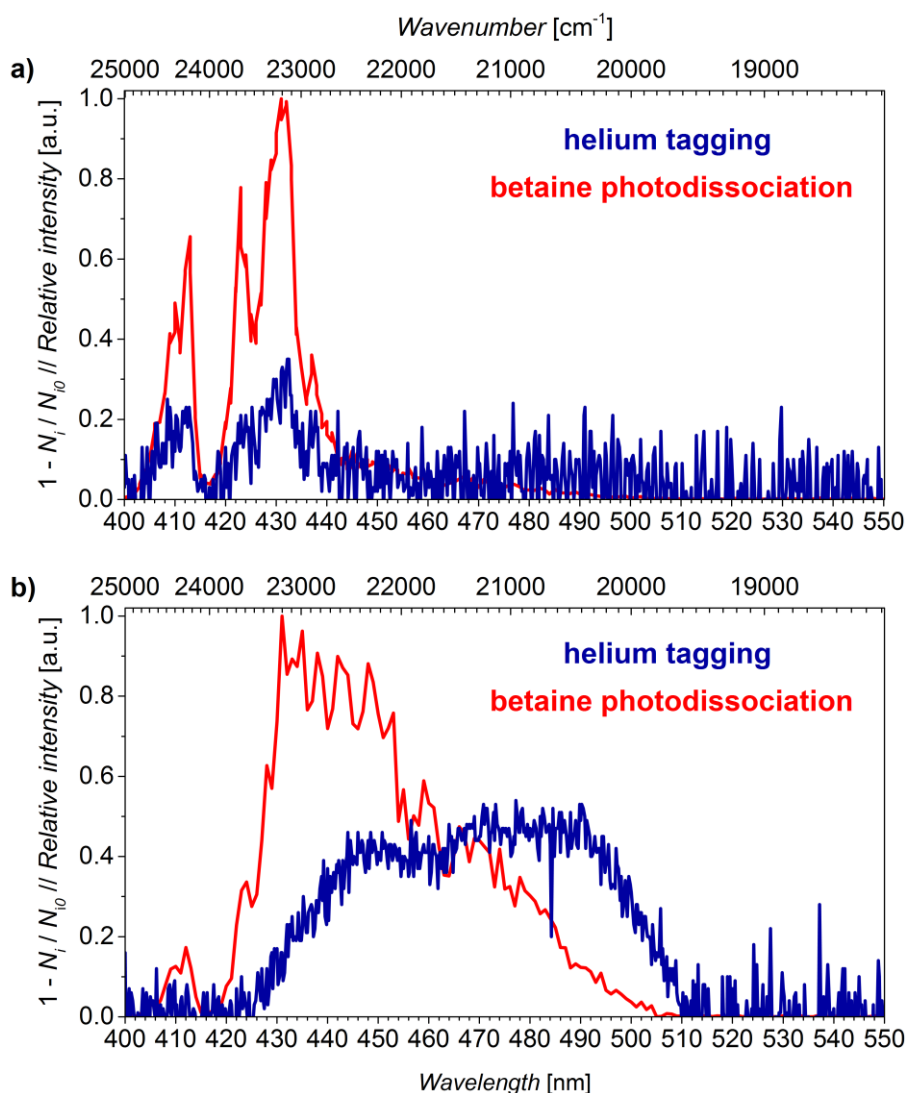


Figure 65. Helium-tagging (navy traces, He tag loss monitored) and betaine photodissociation (red traces, betaine loss monitored) spectra of [Z-HTI·betaine]⁺ (a) and [E-HTI·betaine]⁺ (b) measured at 3 K. The syringe containing the methanolic solution of HTI and betaine was irradiated with 400- or 525-nm LEDs prior to ESI to selectively obtain [E-HTI·betaine]⁺ and [Z-HTI·betaine]⁺ ions, respectively (the identity of ions was confirmed by IRPD).

Betaine photodissociation of *Z*-HTI (Figure 65a, red trace) featured similar changes as the helium-tagging spectrum, including shifts of absorption maxima and preservation of vibrational resolution. Note that the intensities of standard photodissociation (Figure 59a) and betaine photodissociation spectra of *Z*-HTI are incomparable because the number of photons involved in those processes are very different (few vs. one).

Interestingly, the helium-tagging spectrum of *E*-HTI betaine complex shown in Figure 65b (navy trace) shows a nearly five-fold higher intensity than that of bare *E*-HTI (*cf.* Figure 59b). Despite the increase in intensity, the spectrum remains vibrationally unresolved. The betaine photodissociation spectrum (Figure 65b, red trace) features a distinct absorption profile, in contrast to the multiphoton photodissociation spectrum in Figure 59b. The reasons for these effects remain unclear.

After recording absorption spectra of betaine complexes, I proceeded with photoisomerization experiments. Similarly to the isomerization of bare HTI ions, I mainly focused on the region of $\nu(\text{C}=\text{O})$ vibrations, which would also feature absorption of the $\nu(\text{C}=\text{O})$ band belonging to the betaine carboxylate in betaine complexes. Figure 66a shows the IRPD spectrum of $[\text{Z-HTI}\cdot\text{betaine}]^+$ displaying two $\nu(\text{C}=\text{O})$ vibrations at 1667 and 1713 cm^{-1} , which, based on DFT calculations (Figure 66b), correspond to the betaine and HTI carbonyl groups, respectively. The spectrum of the opposite isomer, $[\text{E-HTI}\cdot\text{betaine}]^+$, shown in Figure 66b, contains an intense broad band at 1662 cm^{-1} with a shoulder at 1675 cm^{-1} , which correspond to $\nu(\text{C}=\text{O})$ vibrations of betaine and HTI carbonyl groups. Accordingly, DFT calculations predicted a 13- cm^{-1} frequency difference between these two $\nu(\text{C}=\text{O})$ bands (Figure 66b), thereby explaining the overlap in the experimental spectrum. Please note that the optimized structures of betaine complexes featured the carboxylate group of betaine coordinated to the positively charged trimethylammonium group of HTI. I found no other, energetically more stable, isomer.

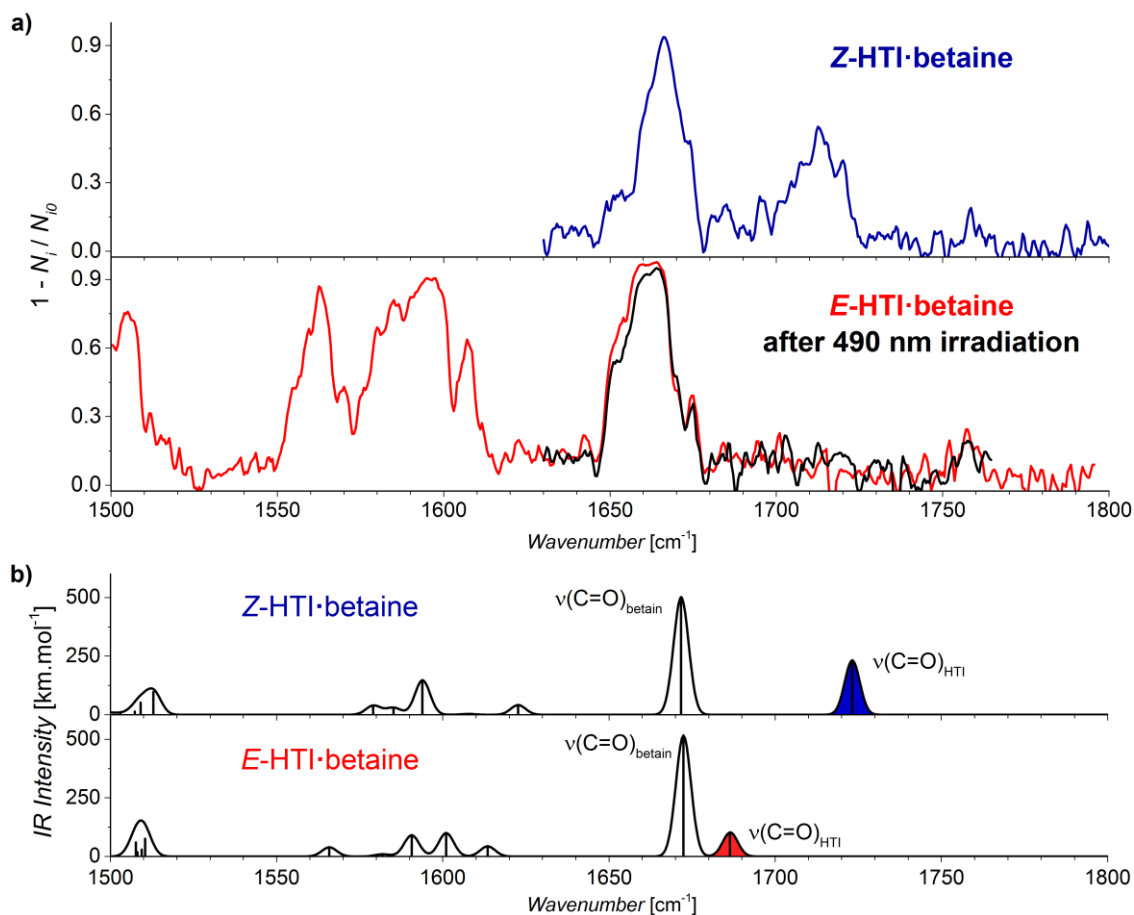


Figure 66. (a) Helium-tagging IRPD spectra of $[Z\text{-HTI}\cdot\text{betaine}]^+$ (navy trace) and $[E\text{-HTI}\cdot\text{betaine}]^+$ (red trace) ions measured at 3 K. In both cases, the loss of the helium tag from $[\text{HTI}\cdot\text{betaine}\cdot\text{He}]^+$ complexes was monitored. The syringe containing the methanolic solution of HTI and betaine was irradiated with 400- or 525-nm LEDs prior to ESI to selectively obtain $[E\text{-HTI}\cdot\text{betaine}]^+$ and $[Z\text{-HTI}\cdot\text{betaine}]^+$ ions. Black trace represents the IRPD spectrum of ions, which were subjected to visible light isomerization. (b) Theoretical IR spectra calculated at the B3LYP-GD3BJ/6-311++G** level of theory, frequency scaling factor 0.99 was used. The optimized structures contained the carboxylate group of betaine coordinated to the positively charged trimethylammonium group of HTI.

Finally, I subjected $[E\text{-HTI}\cdot\text{betaine}]^+$ to photoisomerization experiments at 3 K. I chose 490 nm light, wherein the ions had a strong absorption, whereas the absorption of the opposite isomer was virtually zero (Figure 65). Thus, after 490-nm irradiation of ions in the ion trap for 900 ms, I measured the helium-tagging IRPD spectrum (Figure 66b, black trace). Unfortunately, the spectrum was virtually indistinguishable from the spectrum of pure $[E\text{-HTI}\cdot\text{betaine}]^+$ ions; hence, the result demonstrates that no

$E \rightarrow Z$ photoisomerization occurred. Consequently, despite having a higher absorption cross-section than bare E -HTI, isolated complexes of E -HTI and betaine zwitterion are unable to photoisomerize upon visible-light excitation in the gas phase.

5.3.8 CONCLUSION

I investigated the gas-phase photochemistry of two isomeric hemithioindigo derivatives firstly by recording their helium-tagging photodissociation spectroscopy in visible and infrared ranges at 3 K and, secondly, by combining these ion spectroscopy methods to evaluate the hemithioindigo photoisomerization process while monitoring their unique spectral markers, such as their carbonyl vibrations. I demonstrated that the $Z \rightarrow E$ photoisomerization operates quantitatively, even at the level of isolated molecules in the gas phase, at 3 K. Conversely, despite modifying all possible experimental parameters, I observed complete suppression of the opposite, thermodynamically preferable, $E \rightarrow Z$ photoisomerization. After analyzing the experimental data based on DFT calculations, I concluded that the intrinsically low efficiency of $E \rightarrow Z$ photoisomerization is caused by the rapid decay of the excited state through nonreactive deactivation channels. These channels may stem from the effects of a strong electron-withdrawing trimethylammonium substituent and from the lack of a surrounding solvent environment. Both effects are enhanced in the gas phase. Accordingly, in the condensed phase, the solvent molecules allow efficient photo-switching by preventing the excited E -HTI to internally convert back into its ground state. Despite my attempts to simulate the presence of polar solvent environment by E -HTI complexation with the highly polar betaine zwitterion, I detected no desired $E \rightarrow Z$ photoisomerization in the gas phase, even though the complexes featured increased visible light absorption.

6 GENERAL CONCLUSIONS

I successfully developed gas-phase ion spectroscopy approaches that allow me to track and elucidate photochemical processes using the ISORI instrument, and I applied these methods to study: (1) the effects of tagging and temperature on highly fluorescent xanthene dyes and their electronic spectra, (2) the photodissociation of iron(III) azides involving photooxidation, photoreduction and photo-neutral processes and, accordingly, yielding iron complexes in different oxidation states, (3) the photoisomerization of hemithioindigo molecular switches, which exhibits switching efficiencies different from those previously observed in solution.

In the first study, I discovered that ion complexation with a tagging atom has only negligibly effects on electronic photodissociation spectra; absorption maxima of the 0–0 bands are shifted by *ca.* 8 cm⁻¹ due to differences in tag binding energies in S₀ and S₁ states, rendering these shifts virtually undetectable by low resolution spectroscopy.

In the second study, I identified spin-crossover, between doublet and sextet spin states, as the underlying process governing the photochemistry of pseudo-octahedral iron(III) azides. Thus, if desired, generation of high-valent iron(V) nitrides, photooxidation products of the doublet ground state iron(III) azides, should be preferentially conducted under cryogenic conditions.

Lastly, in my third study, I found that isolation in the gas phase transforms hemithioindigo ions from two-way into one-way molecular switches due to nonradiative deactivations channels, which are enhanced in the absence of solvent. Considering these findings, our understanding of energy barriers and kinetics of excited potential energy surfaces remains limited. Therefore, in future studies, the solvent environment should be carefully evaluated, both experimentally and theoretically, because it is one of the main controlling factors of photoisomerization.

Finally, I hope that my results will stimulate more efforts to pursue novel research avenues and applications of ion spectroscopy towards broadening our knowledge of photochemical processes at the molecular level.

7 REFERENCES AND NOTES

- (1) Santos, L. S., Ed. *Reactive Intermediates: MS Investigations in Solution*; Wiley: Weinheim, Germany, 2010.
- (2) Roithová, J. *Chem. Soc. Rev.* **2012**, *41*, 547–559.
- (3) Schwarz, H.; Asmis, K. R. *Chem. Eur. J.* **2019**, *25*, 2112–2126.
- (4) McLuckey, S. A. *J. Am. Soc. Mass Spectrom.* **1992**, *3*, 599–614.
- (5) Levsen, L.; Schwarz, H. *Mass Spectrom. Rev.* **1983**, *2*, 77–148.
- (6) Baer, T.; Dunbar, R. C. *J. Am. Soc. Mass Spectrom.* **2010**, *21*, 681–693.
- (7) Duncan, M. A. *Int. J. Mass. Spectrom.* **2000**, *200*, 545–569.
- (8) Rizzo, T. R.; Boyarkin, O. V. Cryogenic Methods for the Spectroscopy of Large, Biomolecular Ions. In *Gas-Phase IR Spectroscopy and Structure of Biological Molecules*; Topics in Current Chemistry, vol. 364; Rijs, A.; Oomens, J., Eds.; Springer: Cham, Germany, 2014.
- (9) Gross, J. H. *Mass Spectrometry: A Textbook*, 3rd ed.; Springer: Heidelberg, Germany, 2017.
- (10) Kebarle, P.; Verkerk, U. H. *Mass Spectrom. Rev.* **2009**, *28*, 898–917.
- (11) Cech, N. B.; Enke, C. G. *Mass Spectrom. Rev.* **2001**, *20*, 362–387.
- (12) de Hoffmann, E.; Stroobant, V. *Mass Spectrometry: Principles and Applications*, 3rd ed.; Wiley: Hoboken, NJ, 2007.
- (13) Marshall, A. G.; Hendrickson, C. L.; Jackson, G. S. *Mass Spectrom. Rev.* **1998**, *17*, 1–35.
- (14) Freiser, B. S.; Beauchamp, J. L. *J. Am. Chem. Soc.* **1974**, *96*, 6260–6266.
- (15) Dunbar, R. C. *J. Am. Chem. Soc.* **1971**, *93*, 4354–4358.
- (16) van Velzen, P. N. T.; van der Hart, W. J. *Chem. Phys.* **1981**, *61*, 325–334.
- (17) van der Hart, W. J. *Mass Spectrom. Rev.* **1989**, *8*, 237–268.
- (18) Dumber, R. C.; Fu, E. W. *J. Phys. Chem.* **1977**, *81*, 1531–1536.
- (19) Fu, E. W.; Dunbar, R. C. *J. Am. Chem. Soc.* **1978**, *100*, 2283–2288.
- (20) Orth, R. G.; Dunbar, R. C. *J. Am. Chem. Soc.* **1978**, *100*, 5949–5951.
- (21) Dunbar, R. C. *Int. J. Mass. Spectrom.* **2000**, *200*, 571–589.
- (22) Boyarkin, O. V. *Int. Rev. Phys. Chem.* **2018**, *37*, 559–606.
- (23) Douglas D. J.; Frank, A. J.; Mao, D. *Mass Spectrom. Rev.* **2004**, *24*, 1–29.

- (24) Gerlich, D. Inhomogeneous RF Fields: A Versatile Tool for the Study of Processes with Slow Ions. In *Advances in chemical physics*; vol. LXXXII; Ng, C.-Y.; Baer, M.; Prigogine, I.; Rice, S. A., Eds.; Wiley: Hoboken, NJ, 1992.
- (25) Gerlich, D. *J. Anal. At. Spectrom.* **2004**, *19*, 581–590.
- (26) Gerlich, D.; Norodi, G. *Faraday Discuss.* **2009**, *142*, 57–72.
- (27) Oka, T. *Phys. Rev. Lett.* **1980**, *45*, 531–534.
- (28) Dunbar, R. C. Ion photodissociation. In *Gas Phase Ion Chemistry*, vol. 2; Bowers, M. T., Ed.; Academic press: New York, 1979.
- (29) Lawley, K. P., Ed. *Photodissociation and photoionization*; Wiley: Chichester, NY, 1985.
- (30) Rizzo, T. R.; Stearns, J. A.; Boyarkin, O. V. *Int. Rev. Phys. Chem.* **2009**, *28*, 481–515.
- (31) Ho, Y.-P.; Dunbar, R. C. *Int. J. Mass Spectrom. Ion Processes* **1996**, *154*, 133–144.
- (32) Dunbar, R. C. *Mass. Spectrom. Rev.* **1992**, *11*, 309–339.
- (33) Woodhouse, J. L.; Assmann, M.; Parkes, M. A.; Grounds, H.; Pacman, S. J.; Anderson, J. C.; Wortha, G. A.; Fielding, H. H. *Phys. Chem. Chem. Phys.* **2017**, *19*, 22711–22720.
- (34) McQueen, P. D.; Sagoo, S.; Yao, H.; Jockusch, R. A. *Angew. Chem. Int. Ed.* **2010**, *49*, 9193–9196.
- (35) Forbes, M. W.; Jockusch, R. A. *J. Am. Chem. Soc.* **2009**, *147*, 17038–17039.
- (36) Boesl, U.; Knott, W. *J. Mass Spectrom. Rev.* **1999**, *17*, 275–305.
- (37) Khoury, J. T.; Rodriguez-Cruz, S. E.; Parks, J. H. *J. Am. Soc. Mass Spectrom.* **2002**, *13*, 696–708.
- (38) Sassin, N. A.; Everhart, S. C.; Dangi, B. B.; Ervin, K. M.; Cline, J. I. *J. Am. Soc. Mass Spectrom.* **2009**, *20*, 96–104.
- (39) Bian, Q.; Forbes, M. W.; Talbot, F. O.; Jockusch, R. A. *Phys. Chem. Chem. Phys.* **2010**, *12*, 2590–2598.
- (40) So, H. Y.; Dunbar, R. C. *J. Phys. Chem.* **1989**, *90*, 2192–2000.
- (41) Nagy, A. M.; Talbot, F. O.; Czar, M. F.; Jockusch, R. A. *J. Photochem. Photobiol. A* **2012**, *244*, 47–53.
- (42) Freiser, B. S.; Beauchamp, J. L. *J. Am. Chem. Soc.* **1976**, *98*, 3136–3139.

- (43) Rode, M. F.; Sobolewski, A. L.; Dedonder, C.; Jouvet, C.; Dopfer, O. *J. Phys. Chem. A* **2009**, *113*, 5865–5873.
- (44) Wight, C. A.; Beauchamp, J. L. *Chem. Phys. Lett.* **1981**, *17*, 30–35.
- (45) Freiser, B. S.; Beauchamp, J. L. *Chem. Phys. Lett.* **1975**, *35*, 35–40.
- (46) Orłowski, T. E.; Freiser, B. S.; Beauchamp, J. L. *Chem. Phys.* **1976**, *16*, 439–445.
- (47) Barfknecht, A. T.; Brauman, J. I. *Chem. Phys.* **1986**, *84*, 3870–3881.
- (48) Dunbar, R. C.; Chen, J. H.; So, H. Y.; Asamoto, B. *J. Chem. Phys.* **1987**, *86*, 2081–2086.
- (49) Honovich, J. P.; Segall, J.; Dunbar, R. C. *J. Phys. Chem.* **1985**, *89*, 3617–3622.
- (50) This is the reason why fluorescence spectra, in both gas and condensed phases, are red-shifted with respect to the excitation spectra.
- (51) Sassin, N. A.; Everhart, S. C.; Cline, J. I.; Ervin, K. M. *J. Chem. Phys.* **2008**, *128*, 234305.
- (52) Daly, S.; Kulezsa, A.; Knight, G.; MacAleese, L.; Antoine, R.; Dugourd, P. *J. Phys. Chem. A* **2015**, *119*, 5634–5641.
- (53) Forbes, M. W.; Jockusch, R. A. *J. Am. Soc. Mass Spectrom.* **2011**, *22*, 93–109.
- (54) Zabuga, A. V.; Kamrath, M. Z.; Boyarkin, O. V.; Rizzo, T. R. *J. Chem. Phys.* **2014**, *141*, 154309.
- (55) Little, D. P.; Speir, J. P.; Senko, M. W.; O'Connor, P. B.; McLafferty, F. W. *Anal. Chem.* **1994**, *66*, 2809–2815.
- (56) MacAleese, L.; Maître, P. *Mass Spectrom. Rev.* **2007**, *26*, 583–605.
- (57) Jašíková, L.; Roithová, J. *Chem. Eur. J.* **2018**, *24*, 3374–3390.
- (58) Polfer, N. C. *Chem. Soc. Rev.* **2011**, *40*, 2211–2221.
- (59) Schulz, J.; Jašíková, L.; Škríba, A.; Roithová, J. *J. Am. Chem. Soc.* **2014**, *136*, 11513–11523.
- (60) Elferink, H.; Severijnen, M.; Martens, J.; Mensink, R.; Berden, G.; Oomens, J.; Rutjes, F.; Rijs, A. M.; Boltje, T. *J. Am. Chem. Soc.* **2018**, *140*, 6034–6038.
- (61) Fielicke, A.; von Helden, G.; Meijer, G.; Simard, B.; Dénommée, S.; Rayner, D. M. *J. Am. Chem. Soc.* **2003**, *125*, 11184–11185.
- (62) Lyon, J. T.; Gruene, P.; Fielicke, A.; Meijer, G.; Rayner, D. M. *J. Chem. Phys.* **2009**, *131*, 184706.

- (63) Lang, S. M.; Bernhardt, T. M.; Kiawi, D. M.; Bakker, J. M.; Barnett, R. N.; Landman, U. *Angew. Chem. Int. Ed.* **2015**, *54*, 15113–15117.
- (64) Seo, J.; Hoffmann, W.; Warnke, S.; Huang, X.; Gewinner, S.; Schöllkopf, W.; Bowers, M. T.; von Helden, G.; Pagel, K. *Nat. Chem.* **2017**, *9*, 39–44.
- (65) Seo, J.; Warnke, S.; Pagel, K.; Bowers, M. T.; von Helden, G. *Nat. Chem.* **2017**, *9*, 1263–1268.
- (66) Yang, Y.; Liao, G.; Kong, X. *Sci. Rep.* **2017**, *7*, 16592.
- (67) Gerlich, D. *J. Chin. Chem. Soc.* **2018**, *65*, 637–653.
- (68) Roithová, J.; Gray, A.; Andris, E.; Jašík, J.; Gerlich, D. *Acc. Chem. Res.* **2016**, *49*, 223–230.
- (69) Wolk, A. B.; Leavitt, C. M.; Garand, E.; Johnson, M. A. *Acc. Chem. Res.* **2014**, *47*, 202–210.
- (70) Johnson, C. J.; Wolk, A. B.; Fournier, J. A.; Sullivan, E. N.; Weddle, G. H.; Johnson, M. A. *J. Chem. Phys.* **2014**, *140*, 221101.
- (71) Brümmer, M.; Kaposta, C.; Santambrogio, G.; Asmis, K. R. *J. Chem. Phys.* **2003**, *119*, 12700–12703.
- (72) Jašík, J.; Gerlich, D.; Roithová, J. *J. Am. Chem. Soc.* **2014**, *136*, 2960–2962.
- (73) Holz, M.; Campbell, E. K.; Rice, C. A.; Maier, J. P. *J. Mol. Spectrosc.* **2017**, *332*, 22–25.
- (74) Jašík, J.; Roithová, J. *Int. J. Mass Spectrom.* **2015**, *377*, 109–115.
- (75) Srnec, M.; Navrátil, R.; Andris, E.; Jašík, J.; Roithová, J. *Angew. Chem. Int. Ed.* **2018**, *57*, 17053–17057.
- (76) Solcà, N.; Dopfer, O. *J. Am. Chem. Soc.* **2004**, *126*, 1716–1725.
- (77) Robertson, W. H.; Diken, E. G.; Price, E. A.; Shin, J.-W.; Johnson, M. A. *Science* **2003**, *299*, 1367–1372.
- (78) Douberly, G. E.; Walters, R. S.; Cui, J.; Jordan, K. D.; Duncan, M. A. *J. Phys. Chem. A* **2010**, *114*, 4570–4579.
- (79) Rodriguez, J. D.; Lisy, J. M. *Int. J. Mass Spectrom.* **2009**, *283*, 135–139.
- (80) Wang, G.; Zhou, M.; Goettel, J. T.; Schrobilgen, G. J.; Su, J.; Li, J.; Schlöder, T.; Riedel, S. *Nature* **2014**, *514*, 75–77.
- (81) Garand, E.; Fournier, J. A.; Kamrath, M. Z.; Schley, N. D.; Crabtree, R. H.; Johnson, M. A. *Phys. Chem. Chem. Phys.* **2012**, *14*, 10109–10113.

- (82) Solcà, N.; Dopfer, O. *Angew. Chem. Int. Ed.* **2003**, *42*, 1537–1540.
- (83) Bieske, E. J.; Dopfer, O. *Chem. Rev.* **2000**, *100*, 3963–3998.
- (84) Ward, T. B.; Carnegie, P. D.; Duncan, M. A. *Chem. Phys. Lett.* **2016**, *654*, 1–5.
- (85) Gerlich, D.; Jašík, J.; Andris, E.; Navrátil, R.; Roithová, J. *ChemPhysChem* **2016**, *17*, 3723–3739.
- (86) Uhl, F.; Marx, D. *Angew. Chem. Int. Ed.* **2018**, *57*, 14792–14795.
- (87) Campbell, E. K.; Holz, M.; Gerlich, D.; Maier, J. P. *Nature* **2015**, *523*, 322–323.
- (88) <https://www.ru.nl/felix>
- (89) <http://clio.lcp.u-psud.fr>
- (90) <http://fel.fhi-berlin.mpg.de>
- (91) Duarte, F. J., Ed. *Tunable Laser Applications*, 3rd ed.; CRC Press: Boca Raton, FL, 2015.
- (92) Lushchikova, O. V.; Huitema, D. M. M.; López-Tarifa, P.; Visscher, L.; Jamshidi, Z.; Bakker, J. M. *J. Phys. Chem. Lett.* **2019**, *10*, 2151–2155.
- (93) Houmøller, J.; Wanko, M.; Stöckel, K.; Rubio, A.; Brøndsted Nielsen, S. *J. Am. Chem. Soc.* **2013**, *135*, 6818–6821.
- (94) Yao, H.; Jockusch, R. A. *J. Phys. Chem. A* **2013**, *117*, 1351–1359.
- (95) Sagoo, S. K.; Jockusch, R. A. *J. Photochem. Photobiol. A* **2011**, *220*, 173–178.
- (96) Honma, K. *Phys. Chem. Chem. Phys.* **2018**, *20*, 26859–26869.
- (97) Stocketta, M. H.; Houmøller, J.; Brøndsted Nielsen, S. *J. Chem. Phys.* **2015**, *145*, 104303.
- (98) Andersen, L. H.; Nielsen, I. B.; Kristensen, M. B.; El Ghazaly, M. O. A.; Haacke, S.; Brøndsted Nielsen, M.; Petersen, M. Å. *J. Am. Chem. Soc.* **2005**, *127*, 12347–12350.
- (99) Boyarkin, O. V.; Mercier, S. R.; Kamariotis, A.; Rizzo, T. R. *J. Am. Chem. Soc.* **2006**, *128*, 2816–2817.
- (100) Redwine, J. G.; Davis, Z. A.; Burke, N. L.; Oglesbee, R. A.; McLuckey, S. A.; Zwier, T. S. *Int. J. Mass Spectrom.* **2013**, *348*, 9–14.
- (101) Ehlerding, A.; Wyer, J. A.; Zettergren, H.; Kirketerp, M.-B. S.; Brøndsted Nielsen, S. *J. Phys. Chem. A* **2010**, *114*, 299–303.
- (102) Ishikawa, H.; Nakano, T.; Eguchi, T.; Shibukawa, T.; Fuke, K. *Chem. Phys. Lett.* **2011**, *514*, 234–238.

- (103) Günther, A.; Nieto, P.; Müller, D.; Sheldrick, A.; Gerlich, D.; Dopfer, O. *J. Mol. Spectrosc.* **2017**, *332*, 8–15.
- (104) Boyarkin, O. V.; Kopysov, V. *Rev. Sci. Instrum.* **2014**, *85*, 033105.
- (105) Mercier, S. R.; Boyarkin, O. V.; Kamariotis, A.; Guglielmi, M.; Tavernelli, I.; Cascella, M.; Rothlisberger, U.; Rizzo, T. R. *J. Am. Chem. Soc.* **2006**, *128*, 16938–16943.
- (106) Fujihara, A.; Noguchi, N.; Yamada, Y.; Ishikawa, H.; Fuke, K. *J. Phys. Chem. A* **2009**, *113*, 8169–8175.
- (107) Houmøller, J.; Wanko, M.; Rubio, A.; Brøndsted Nielsen, S. *J. Phys. Chem. A* **2015**, *119*, 11498–11503.
- (108) Dopfer, O.; Patzer, A.; Chakraborty, S.; Alata, I.; Omidyan, R.; Broquier, M.; Dedonder, C.; Jouve, C. *J. Chem. Phys.* **2014**, *140*, 124314.
- (109) Nagornova, N. S.; Rizzo, T. R.; Boyarkin, O. V. *Science* **2012**, *336*, 320–323.
- (110) Ishikawa, H.; Kurusu, I.; Yagi, R.; Kato, R.; Kasahara, Y. *J. Phys. Chem. Lett.* **2017**, *8*, 2541–2546.
- (111) Milne, B. F.; Toker, Y.; Rubio, A.; Brøndsted Nielsen, S. *Angew. Chem. Int. Ed.* **2015**, *54*, 2170–2173.
- (112) Kjær, C.; Stockett, M. H.; Pedersen, B. M.; Brøndsted Nielsen, S. *J. Phys. Chem. B* **2016**, *120*, 12105–12110.
- (113) Stockett, M. H.; Boesen, M.; Houmøller, J.; Brøndsted Nielsen, S. *Angew. Chem. Int. Ed.* **2017**, *56*, 3490–3495.
- (114) Kjær, K.; Lisy, J. M.; Brøndsted Nielsen, S. *J. Phys. Chem. A* **2018**, *122*, 3211–3217.
- (115) Herzberg, G. *Molecular spectra and molecular structure. Vol. 1: Spectra of diatomic molecules*, 2nd ed.; David van Nostrand: New York, 1950.
- (116) This is true only when ions are not vibrationally excited, which is unlikely at elevated temperatures.
- (117) Sheldrick, A.; Müller, D.; Günther, A.; Nieto, P.; Dopfer, O. *Phys. Chem. Chem. Phys.* **2018**, *20*, 7407–7414.
- (118) Andris, E.; Navrátil, R.; Jašík, J.; Puri, M.; Costas, M.; Que, L., Jr.; Roithová, J. *J. Am. Chem. Soc.* **2018**, *140*, 14391–14400.

- (119) Kulesza, A.; Titov, E.; Daly, S.; Włodarczyk, R.; Megow, J.; Saalfrank, P.; Choi, C. M.; MacAleese, L.; Antione, R.; Dugourd, P. *ChemPhysChem* **2016**, *17*, 3129–3138.
- (120) Savarese, M.; Aliberti, A.; De Santo, I.; Battista, E.; Causa, F.; Netti, P. A.; Rega, N. *J. Phys. Chem. A* **2012**, *116*, 7491–7497.
- (121) Polfer, N. C.; Oomens, J. *Mass Spectrom. Rev.* **2009**, *28*, 468–494.
- (122) Warnke, S.; von Helden, G.; Pagel, K. *J. Am. Chem. Soc.* **2013**, *135*, 1177–1180.
- (123) Seo, J.; Hoffmann, W.; Warnke, S.; Bowers, M. T.; Pagel, K.; von Helden, G. *Angew. Chem. Int. Ed.* **2016**, *55*, 14173–14176.
- (124) Bakhtiari, M.; Konermann, L. *J. Phys. Chem. B* **2019**, *123*, 1784–1796.
- (125) Chen, S.-H.; Russell, D. H. *J. Am. Soc. Mass Spectrom.* **2015**, *26*, 1433–1443.
- (126) Andris, E.; Navrátil, R.; Jašík, J.; Terencio, T.; Srnec, M.; Costas, M.; Roithová, J. *J. Am. Chem. Soc.* **2017**, *139*, 2757–2765.
- (127) Sabenya, G.; Lázaro, L.; Gamba, I.; Martin-Diaconescu, V.; Andris, E.; Weyhermüller, T.; Neese, F.; Roithová, J.; Bill, E.; Lloret-Fillol, J.; Costas, M. *J. Am. Chem. Soc.* **2017**, *139*, 9168–9177.
- (128) Meyer, K.; Bill, E.; Mienert, B.; Weyhermüller, T.; Wieghardt, K. *J. Am. Chem. Soc.* **1999**, *121*, 4859–4876.
- (129) Grapperhaus, C. A.; Mienert, B.; Bill, E.; Weyhermüller, T.; Wieghardt, K. *Inorg. Chem.* **2000**, *39*, 5306–5317.
- (130) Berry, J. F.; Bill, E.; Bothe, E.; Weyhermüller, T.; Wieghardt, K. *J. Am. Chem. Soc.* **2005**, *127*, 11550–11551.
- (131) Jašík, J.; Žabka, J.; Roithová, J.; Gerlich, D. *Int. J. Mass Spectrom.* **2013**, *354-355*, 204–210.
- (132) Jašík, J.; Gerlich, D.; Roithová, J. *J. Am. Chem. Soc.* **2014**, *136*, 2960–2962.
- (133) Škríba, A.; Jašík, J.; Andris, E.; Roithová, J. *Organometallics* **2016**, *35*, 990–994.
- (134) Ducháčková, L.; Roithová, J. *Chem. Eur. J.* **2019**, *15*, 13399–13405.
- (135) Gerlich, D. The Production and Study of Ultra-Cold Molecular Ions. In *Low Temperatures and Cold Molecules*; Smith, I. W. M., Ed.; Imperial College Press: Singapore, 2008.
- (136) Jašík, J.; Gerlich, D.; Roithová, R. *J. Phys. Chem. A* **2015**, *119*, 2532–2542.

- (137) Savitzky, A.; Golay, M. J. E. *Anal. Chem.* **1964**, *36*, 1627–1639.
- (138) Gaussian 09, Revision D.01, Frisch, M. J.; Trucks, G. W.; Schlegel, H. B.; Scuseria, G. E.; Robb, M. A.; Cheeseman, J. R.; Scalmani, G.; Barone, V.; Mennucci, B.; Petersson, G. A.; Nakatsuji, H.; Caricato, M.; Li, X.; Hratchian, H. P.; Izmaylov, A. F.; Bloino, J.; Zheng, G.; Sonnenberg, J. L.; Hada, M.; Ehara, M.; Toyota, K.; Fukuda, R.; Hasegawa, J.; Ishida, M.; Nakajima, T.; Honda, Y.; Kitao, O.; Nakai, H.; Vreven, T.; Montgomery, J. A., Jr.; Peralta, J. E.; Ogliaro, F.; Bearpark, M.; Heyd, J. J.; Brothers, E.; Kudin, K. N.; Staroverov, V. N.; Keith, T.; Kobayashi, R.; Normand, J.; Raghavachari, K.; Rendell, A.; Burant, J. C.; Iyengar, S. S.; Tomasi, J.; Cossi, M.; Rega, N.; Millam, J. M.; Klene, M.; Knox, J. E.; Cross, J. B.; Bakken, V.; Adamo, C.; Jaramillo, J.; Gomperts, R.; Stratmann, R. E.; Yazyev, O.; Austin, A. J.; Cammi, R.; Pomelli, C.; Ochterski, J. W.; Martin, R. L.; Morokuma, K.; Zakrzewski, V. G.; Voth, G. A.; Salvador, P.; Dannenberg, J. J.; Dapprich, S.; Daniels, A. D.; Farkas, O.; Foresman, J. B.; Ortiz, J. V.; Cioslowski, J.; Fox, D. J. Gaussian, Inc., Wallingford CT, 2013.
- (139) <https://www.chemcraftprog.com>
- (140) Becke, A. D. *J. Chem. Phys.* **1993**, *98*, 5648–5652.
- (141) Lee, C.; Yang, W.; Parr, R. G. *Phys. Rev. B* **1988**, *37*, 785–789.
- (142) Miehlich, B.; Savin, A.; Stoll, H.; Preuss, H. *Chem. Phys. Lett.* **1989**, *157*, 200–206.
- (143) Stephens, P. J.; Devlin, F. J.; Chabalowski, C. F.; Frisch, M. J. *J. Phys. Chem.* **1994**, *98*, 11623–11627.
- (144) Grimme, S.; Antony, J.; Ehrlich, S.; Krieg, H. *J. Chem. Phys.* **2010**, *132*, 154104.
- (145) Grimme, S.; Ehrlich, S.; Goerigk, L. *J. Comp. Chem.* **2011**, *32*, 1456–1465.
- (146) Zhao, Y.; Truhlar, D. G. *J. Chem. Phys.* **2006**, *125*, 194101.
- (147) Weigend, F.; Ahlrichs, R. *Phys. Chem. Chem. Phys.* **2005**, *7*, 3297–3305.
- (148) Aquilante, F.; Pedersen, T. B.; Lindh, R.; Roos, B. O.; Sánchez de Merás, A.; Koch, H. *J. Chem. Phys.* **2008**, *129*, 024113.
- (149) Hess, B. A. *Phys. Rev. A* **1986**, *33*, 3742–3748.
- (150) Jansen, G.; Hess, B. A. *Phys. Rev. A* **1989**, *39*, 6016–6017.

- (151) Andris, E.; Navrátil, R.; Jašík, J.; Sabenya, G.; Costas, M.; Srnec, M.; Roithová, J. *Angew. Chem. Int. Ed.* **2017**, *56*, 14057–14060.
- (152) Santoro, F.; Lami, A.; Improta, R.; Bloino, J.; Barone, V. *J. Chem. Phys.* **2008**, *128*, 224311.
- (153) Barone, V.; Bloino, J.; Biczysko, J. M. *Vibrationally-resolved electronic spectra in GAUSSIAN 09*.
- (154) PGOPIER, A Program for Simulating Rotational, Vibrational and Electronic Spectra, Western, C. M., University of Bristol, <http://pgopher.chm.bris.ac.uk>
- (155) Mozhayskiy, V. A.; Krylov, A. I. ezSpectrum, <http://iopshell.usc.edu/downloads>
- (156) Wright, P. Xanthene Dyes. In *Kirk-Othmer Encyclopedia of Chemical Technology*; Wiley: Hoboken, NJ, 2014.
- (157) Baeyer, A. *Chem. Ber.* **1871**, *4*, 555–558.
- (158) Kubin, R. F.; Fletcher, A. N. *J. Lumin.* **1982**, *27*, 455–462.
- (159) Sabnis, R. W. *Handbook of Fluorescent Dyes and Probes*; Wiley: Hoboken, NJ, 2015.
- (160) Arbeloa, F. L.; Arbeloa, T. L.; Estevez, M. J. T.; Arbeloa, I. L. *J. Phys. Chem.* **1991**, *95*, 2203–2208.
- (161) Drexhage, K. H. *Dye Lasers*; Schafer, F. P., Ed.; Springer: Berlin, Germany, 1973.
- (162) Flury, M.; Wai, N. N. *Rev. Geophys.* **2003**, *41*, 1–37.
- (163) Grimm, J. B.; Heckman, L. M.; Lavis, L. D. *Prog. Mol. Biol. Transl.* **2013**, *113*, 1–34.
- (164) Farinha, J. P. S.; Charreyre, M. T.; Martinho, J. M. G.; Winnik, M. A.; Pichot, C. *Langmuir* **2001**, *17*, 2617–2623.
- (165) Bogen, S. T.; Karolin, J.; Molotkovsky, J. G.; Johansson, L. B. A. *J. Chem. Soc. Faraday Trans.* **1998**, *94*, 2435–2440.
- (166) Gonçalves, M. S. T. *Chem. Rev.* **2009**, *109*, 190–212.
- (167) Shiraishi, Y.; Miyamoto, R.; Zhang, X.; Hirai, T. *Org. Lett.* **2007**, *9*, 3921–3924.
- (168) Kommareddi, S.; Abramowsky, C.; Swinehart, G.; Hrabak, L. *Human Pathology* **1984**, *15*, 1085–1089.
- (169) Emery, A. J.; Hazen, F. K.; Stotz, E. *Biotech. Histochem.* **1950**, *25*, 201–208.

- (170) Beija, M.; Afonsoa, C. A. M.; Martinho, J. M. G. *Chem. Soc. Rev.* **2009**, *38*, 2410–2433.
- (171) Wellman, S. M. J.; Jockush, R. A. *J. Phys. Chem. A* **2015**, *119*, 6333–6338.
- (172) In analogy to the ground electronic state, loosely bound tags will unlikely be bound in a vibrationally excited S₁ electronic state.
- (173) Kelleher, P. J.; Johnson, C. J.; Fournier, J. A.; Johnson, M. A.; McCoy, A. B. *J. Phys. Chem. A* **2015**, *119*, 4170–4176.
- (174) Yao, H.; Jockush, R. A. *J. Phys. Chem. A* **2013**, *117*, 1351–1359.
- (175) Abu-Omar, M. M.; Loaiza, A.; Hontzeas, N. *Chem. Rev.* **2005**, *105*, 2227–2252.
- (176) Solomon, E. I.; Light, K. M.; Liu, L. V.; Srnec, M.; Wong, S. D. *Acc. Chem. Res.* **2013**, *46*, 2725–2739.
- (177) Klein, J. E. M. N.; Que, L., Jr. Biomimetic High-Valent Mononuclear Nonheme Iron-Oxo Chemistry. In *Encyclopedia of Inorganic and Bioinorganic Chemistry*; Scott, R. A., Ed.; Wiley: Hoboken, NJ, 2016.
- (178) Svastits, E. W.; Dawson, J. H.; Breslow, R.; Gellman, S. H. *J. Am. Chem. Soc.* **1985**, *107*, 6427–6428.
- (179) Hoffman, B. M.; Dean, D. R.; Seefeldt, L. C. *Acc. Chem. Res.* **2009**, *42*, 609–619.
- (180) Ertl, G. *Angew. Chem. Int. Ed. Engl.* **1990**, *29*, 1219–1227.
- (181) Smith, J. M.; Subedi, D. *Dalton Trans.* **2012**, *41*, 1423–1429.
- (182) Hohenberger, J.; Ray, K.; Meyer, K. *Nat. Commun.* **2012**, *3*, 720.
- (183) Wagner, W.-D.; Nakamoto, K. *J. Am. Chem. Soc.* **1988**, *110*, 4044–4045.
- (184) Vennekate, H.; Schwarzer, D.; Torres-Alacan, J.; Vöhringer, P. *J. Am. Chem. Soc.* **2014**, *136*, 10095–10103.
- (185) Torres-Alacan, J.; Vöhringer, P. *Int. Rev. Phys. Chem.* **2014**, *33*, 521–553.
- (186) Berry, J. F.; Bill, E.; Bothe, E.; DeBeer George, S.; Mienert, F.; Neese, F.; Wieghardt, K. *Science* **2006**, *312*, 1937–1941.
- (187) Vennekate, H.; Schwarzer, D.; Torres-Alacan, J.; Krahe, O.; Filippou, A. C.; Neese, F.; Vöhringer, P. *Phys. Chem. Chem. Phys.* **2012**, *14*, 6165–6172.
- (188) Torres-Alacan, J.; Das, U.; Filippou, A. C.; Vöhringer, P. *Angew. Chem. Int. Ed.* **2013**, *125*, 13067–13071.
- (189) Torres-Alacan, J.; Vöhringer, P. *Chem. Eur. J.* **2017**, *23*, 6746–6751.

- (190) Neese, F. *Coord. Chem. Rev.* **2009**, *253*, 526–563.
- (191) Semrouni, D.; Balaj, O. P.; Calvo, F.; Correia, C. F.; Clavaguéra, C.; Ohanessian, G. *J. Am. Mass Spectrom. Soc.* **2010**, *21*, 728–738.
- (192) Wiedbrauk, S.; Dube, H. *Tetrahedron Lett.* **2015**, *56*, 4266–4274.
- (193) Friedländer, P. *Chem. Ber.* **1906**, *39*, 1060–1066.
- (194) Konieczny, M. T.; Konieczny, W. *Heterocycles* **2005**, *65*, 451–464.
- (195) Gerwien, A.; Reinhardt, T.; Mayer, P.; Dube, H. *Org. Lett.* **2018**, *20*, 232–235.
- (196) Dube, H.; Rebek, J., Jr. *Angew. Chem. Int. Ed.* **2012**, *51*, 3207–3210.
- (197) Guentner, M.; Uhl, M.; Mayer, P.; Dube, H. *Chem. Eur. J.* **2016**, *22*, 16433–16436.
- (198) Wiedbrauk, S.; Bartelmann, T.; Thumser, S.; Mayer, P.; Dube, H. *Nat. Commun.* **2015**, *9*, 1456.
- (199) Hoffmann, K.; Mayer, P.; Dube, H. *Org. Biomol. Chem.* **2019**, *17*, 1979–1983.
- (200) Guentner, M.; Schildhauer, M.; Thumser, S.; Mayer, P.; Stephenson, D.; Mayer, P. J.; Dube, H. *Nat. Comm.* **2015**, *6*, 8406.
- (201) Huber, L. A.; Hoffmann, K.; Thumser, S.; Böcher, N.; Mayer, P.; Dube, H. *Angew. Chem. Int. Ed.* **2017**, *56*, 14536–14539.
- (202) Regner, N.; Herzog, T. T.; Haiser, K.; Hoppmann, C.; Beyermann, M.; Sauermann, J.; Engelhard, M.; Cordes, T.; Rück-Braun, K.; Zinth, W. *J. Phys. Chem. A* **2012**, *116*, 4181–4191.
- (203) Kitzig, S.; Thilemann, M.; Cordes, T.; Rück-Braun, K. *ChemPhysChem* **2016**, *17*, 1252–1263.
- (204) Fullbeck, M.; Michalsky, E.; Jaeger, I. S.; Henklein, P.; Kuhn, H.; Rück-Braun, K.; Preissner, R. *Genome Inform.* **2006**, *17*, 141–151.
- (205) Nenov, A.; Cordes, T.; Herzog, T. T.; Zinth W.; de Vivie-Riedle, R. *J. Phys. Chem. A* **2010**, *114*, 13016–13030.
- (206) Wilcken, R.; Schildhauer, M.; Rott, F.; Huber, L. A.; Guentner, M.; Thumser, S.; Hoffmann, K.; Oesterling, S.; de Vivie-Riedle, R.; Riedle, E.; Dube, H. *J. Am. Chem. Soc.* **2017**, *139*, 10956–10959.
- (207) Zweig J. E.; Newhouse, T. R. *J. Am. Chem. Soc.* **2017**, *139*, 10956–10959.
- (208) Wiedbrauk, S.; Maerz, B.; Samoylova, E.; Reiner, A.; Trommer, F.; Mayer, P.; Zinth, W.; Dube, H. *J. Am. Chem. Soc.* **2016**, *138*, 12219–12227.

- (209) Wiedbrauk, S.; Maerz, B.; Samoylova, E.; Mayer, P.; Zinth, W.; Dube, H. *J. Phys. Chem. Lett.* **2017**, *8*, 1585–1592.
- (210) Markworth, P. B.; Adamson, B. D.; Coughlan, N. J. A.; Goerigk, L.; Bieske, E. J. *J. Phys. Chem. Chem. Phys.* **2015**, *17*, 25676–25688.
- (211) Scholz, M. S.; Bull, J. N.; Coughlan, N. J. A.; Carrascosa, E.; Adamson, B. D.; Bieske, E. J. *J. Phys. Chem. A* **2017**, *121*, 6413–6419.
- (212) Beekmeyer, R.; Parkes, M. A.; Ridgwell, L.; Riley, J. W.; Chen, J.; Feringa, B. L.; Kerridge, A.; Fielding, H. H. *Chem. Sci.* **2017**, *8*, 6141–6148.
- (213) Navrátil, R.; Wiedbrauk, S.; Jašík, J.; Dube, H.; Roithová, J. *Phys. Chem. Chem. Phys.* **2018**, *20*, 6868–6876.
- (214) Butkevich, A. N.; Bossi, M. L.; Lukinavičius, G.; Hell, S. W. *J. Am. Chem. Soc.* **2019**, *141*, 981–989.
- (215) Robinson-Duggon, J.; Mariño-Ocampo, N.; Barrias, P.; Zúñiga-Núñez, D.; Günther, G.; Edwards, A. M.; Greer, A.; Fuentealba, D. *J. Phys. Chem. A* **2019**, *123*, 4863–4872.
- (216) Cordes, T.; Schadendorf, T.; Priewisch, B.; Rück-Braun, K.; Zinth, W. *J. Phys. Chem. A* **2008**, *112*, 581–588.
- (217) Malkin, S.; Fischer, E. *J. Phys. Chem.* **1964**, *68*, 1153–1163.
- (218) Maerz, B.; Wiedbrauk, S.; Oesterling, S.; Samoylova, E.; Nenov, A.; Mayer, P.; de Vivie-Riedle, R.; Zinth, W.; Dube, H. *Chem. Eur. J.* **2014**, *20*, 13984–13992.